Accelerating cardiovascular MRI

Document status and date:
Published: 01/01/2015

Document Version:
Publisher's PDF, also known as Version of Record (includes final page, issue and volume numbers)

Please check the document version of this publication:

• A submitted manuscript is the version of the article upon submission and before peer-review. There can be important differences between the submitted version and the official published version of record. People interested in the research are advised to contact the author for the final version of the publication, or visit the DOI to the publisher's website.
• The final author version and the galley proof are versions of the publication after peer review.
• The final published version features the final layout of the paper including the volume, issue and page numbers.

Link to publication

Accelerating Cardiovascular MRI

Abdallah Motaal
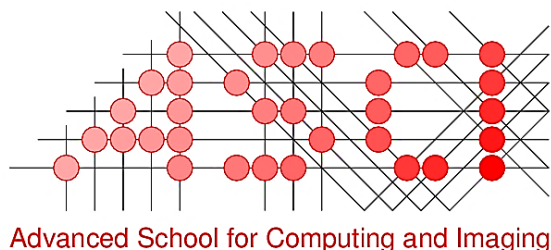
A catalogue record is available from the Eindhoven University of Technology Library.

The work described in this thesis was performed in the Biomedical NMR group of the Department of Biomedical Engineering at the Eindhoven University of Technology, Eindhoven, the Netherlands.

Accelerating Cardiovascular MRI

PROEFSCHRIFT

ter verkrijging van de graad van doctor aan de Technische

Universiteit Eindhoven, op gezag van de rector magnificus,

prof.dr.ir. C.J. van Duijn, voor een commissie aangewezen door het

College voor Promoties in het openbaar te verdedigen

op maandag 30 maart 2015 om 16:00 uur

door

Abdallah Gaafar AbdelMotaal Mohamed

geboren te Aswan, Egypte

Dit proefschrift is goedgekeurd door de promotoren en de samenstelling van de promotiecommissie is als volgt:

voorzitter:	prof.dr. P.A.L. Hilbers
1e promotor:	prof.dr. K. Nicolay
2e promotor:	prof.dr. L.M. J. Florack
copromotor(en):	dr.ir. G.J. Strijkers
leden:	prof.dr. A. Webb (Leiden University Medical Center)
	prof.dr. C. Faber (Westfalische Wilhelms-Universitat Munster)
	dr.ir. M. Mischi
adviseur(s):	dr.ir. A. Nederveen (Academic Medical Center, Amsterdam)

To my beloved parents
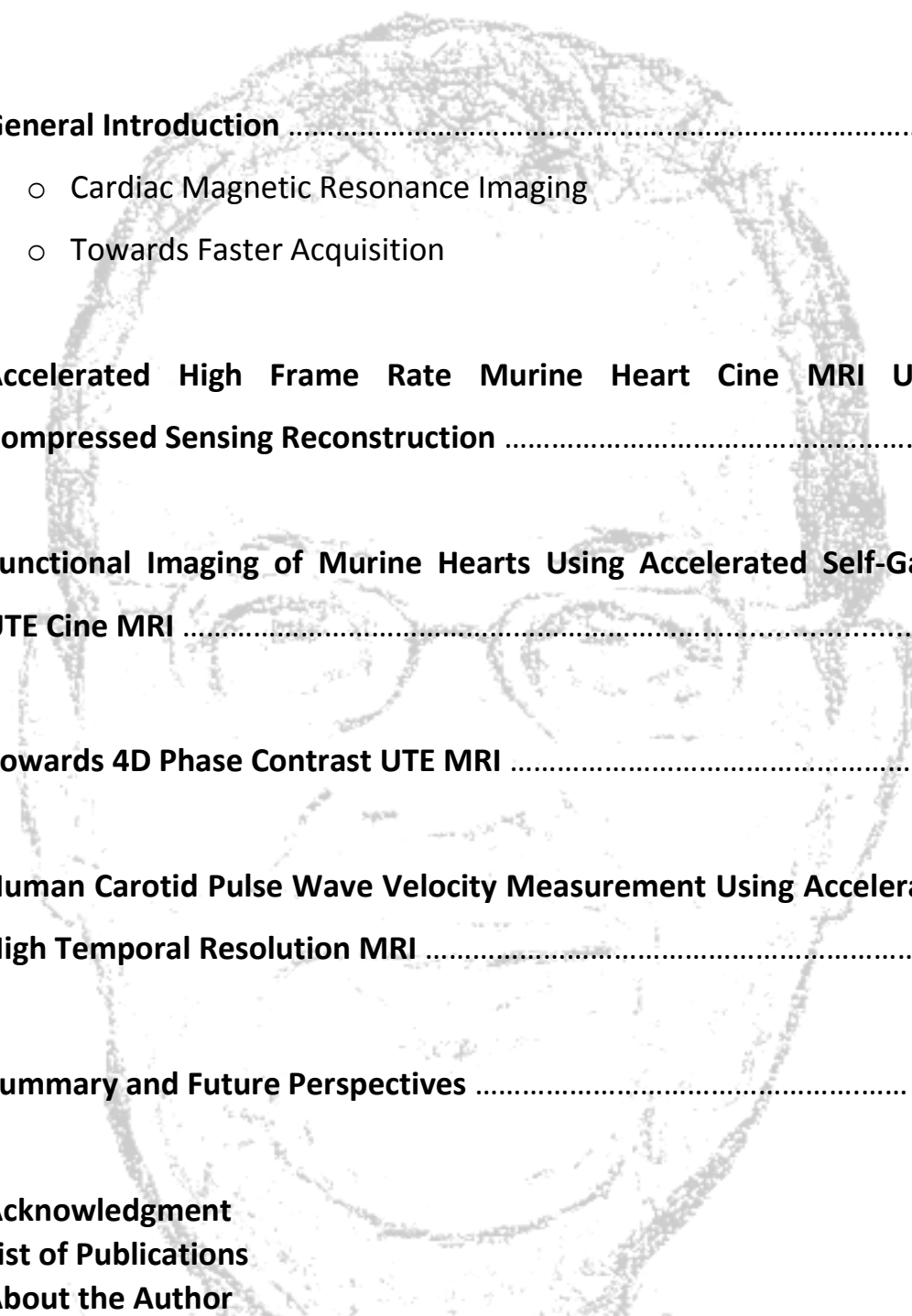
Father
(1955-2013)

&

Mother

Table of contents

General Introduction

I. Cardiac Magnetic Resonance Imaging
II. Towards Faster Acquisition

As you go …

Related Articles:

➢ Bakermans A.J., Abdurrachim D., Moonen R.P.M., Motaal A.G., J.J. Prompers, G.J Strijkers, K. Vandoorne, K. Nicolay. Small animal MR imaging and spectroscopy of cardiovascular disorder. Progress Nucl Magn Reson Spectros. Invited Review.

This thesis focuses on mouse heart Magnetic Resonance Imaging (MRI), and more specifically on developing strategies to accelerate the MRI measurements. In this introductory chapter, first a general introduction about the cardiovascular system and cardiac MRI is presented. Next a short outline of common murine cardiac MRI imaging strategies is reported. Finally a brief overview for accelerating MRI scans with some of the commonly used strategies will be discussed.

1.1   The cardiovascular system

The heart is a vital organ that is responsible for pumping out the blood to the whole body. The heart, blood and vessels build up the cardiovascular system. This is a closed system where oxygen delivery to the different cells inside the body takes place. In the cardiovascular system, three blood circulations are present; 1-The systemic circulation: transporting the blood from/to heart and whole body, 2-pulmonary circulation: transporting the blood from/to heart and lungs, 3-coronary circulation: providing the heart with oxygenated blood through the coronary arteries.

In the systemic circulation, the oxygen saturated blood is transported from the heart, specifically from the left ventricle, through the arteries to the capillaries where oxygen/carbon-dioxide exchange takes place, since the blood supplies the surroundings cells with oxygen and withdraws the carbon dioxide that is produced due to the cell metabolism. Blood carrying carbon dioxide is then collected through veins and delivered back to the heart, specifically to the right atrium. From this point, the pulmonary circulation is responsible for taking out the blood carrying carbon dioxide from the right ventricle and pumps it to the lungs via the pulmonary artery. In the lungs, oxygenation takes place and the oxygen-saturated blood is returned back to the heart, specifically to the left atrium, through the pulmonary veins. The atrium collects the blood and stores it for a short period during the ventricle contraction, and during ventricular relaxations, the atria contract pushing the blood to the ventricles for quick filling of the ventricles. Heart

valves prevent the backflow of the blood from ventricles to atrium. The tricuspid and mitral valves are the valves between right- atrium and ventricle, and left- atrium and ventricle, respectively. The valves are very important for the pump efficiency.

As explained above, contractions of atria and ventricles take place, and strict coordination of these contractions are mandatory for stable and efficient blood pumping. This coordination of contraction is caused by an electric pulse which is traveling through the heart muscle from the atria to both ventricles. This electrical pulse is generated by the sinoatrial node (SA node), which is located on the surface of the right atrium of the heart. The electrical signal is strong enough to be measured and recorded using electrocardiography (ECG) [1]. Fig. 1 shows the anatomical map of the heart.

With ECG the different heart phases can be distinguished. The cardiac cycle is defined by the state of the ventricles. The systolic heart phase is defined as the period where ventricles pump the blood into the aorta or the pulmonary artery. On the other hand, the period during ventricular relaxation in which the ventricles are filled with blood from the atria is defined as the diastolic heart phase. By detecting the depolarization of the ventricles within the ECG signal the start of the systolic heart phase can be identified. z
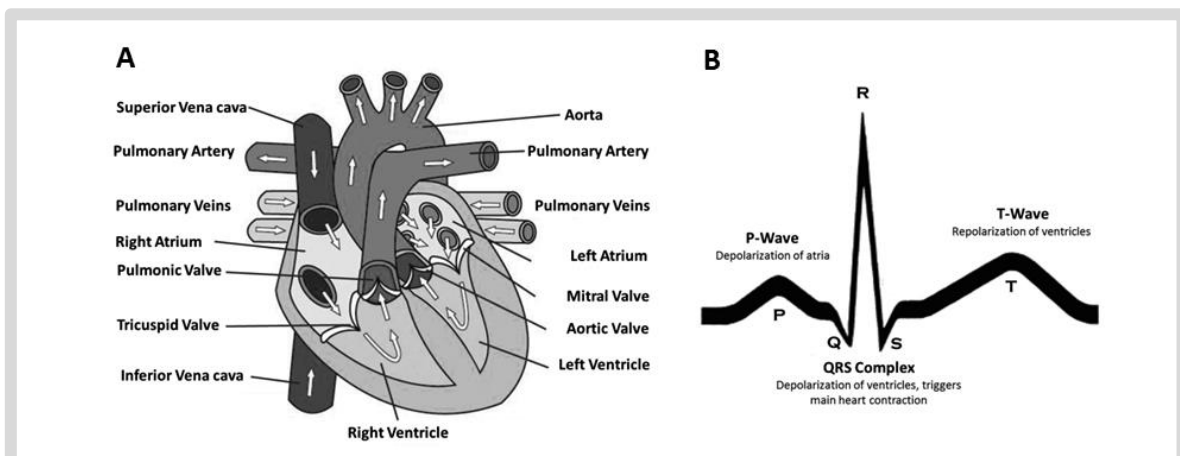
Figure 1. A) Schematic diagram showing the anatomical map of the heart with the most important blood vessels, valves and the different heart chambers. B) The ECG signal that coordinates the beating pattern of the heart, showing the different phases of the heart muscle relaxation and contraction.

1.2   Cardiac Magnetic Resonance Imaging

Magnetic resonance imaging (MRI) is a versatile imaging technique, which has evolved tremendously in the past decades. It plays an important role in the field of cardiovascular research as it offers exceptional precision in the depiction of the anatomy and function. Its broad spectrum of soft-tissue contrast options provides a multiplicity of tools for cardiovascular status assessment.

At present, and because of the remarkable advances in MRI hardware and innovation in imaging strategies, many MRI-based assays of in-vivo tissue status have much matured. MRI offers superb image quality with high spatial and temporal resolutions. Besides, avoiding using ionizing radiations, which is a negative aspect of other imaging modalities such as computed tomography (CT) or positron emission tomography (PET), is a merit [2]. The variety of applications makes MRI the most valuable imaging technique for medical diagnostics and monitoring therapeutic interventions.

Technological developments in cardiovascular MRI presently proceed very much along similar paths for human and small animal applications. Rodents such as mice and rats become popular models to study the cardiovascular status. The studies in this thesis mainly deal with mouse and rats models. However, there is a profound difference in heart rate and size between man and rodents. The typical heart rates of 60 beats-per-min (bpm) allow measurements of human cardiac function within a single breath hold with state-of-the-art hardware. However, even the very short minimal repetition times (TR) that can be achieved on nowadays, animal scanners are still too slow to allow for measurements of cardiac function in mice, having heart rates between 400 and 600 bpm at rest, within similar acquisition times as those achieved in human.

Obviously the large differences in heart size as well as respiration frequency between man and mouse also contribute to the fact that the acquisition of cardiac images with sufficiently high spatial resolution and acceptable signal to noise ratio (SNR) is a lot more

challenging in mice than man. Despite of the fact that MRI of the small animal cardiovascular system is technologically more difficult than MR studies in man, there is still a strong impetus for developing advanced MR tools in rodents. The main driver is the fact that mouse models of cardiovascular diseases and to a lesser extent rat models, are indispensable for unraveling disease mechanisms and for early stage drug development. Most developments for mouse cardiac MRI have focused on measuring cardiac function, which has been used for studying several cardiac diseases, such as myocardial infarction [3-5], cardiac hypertrophy [6, 7] and aortic valve dysfunction [8].

Translation of cardiac imaging protocols from/to mice and human requires careful reconsideration of sequence design parameters. Recently, considerable progress in protocols for mouse as well as human cardiac MRI has been made, improving the contrast-to-noise ratio (CNR), speed and sensitivity. Fig. 2 shows an example of mouse and human cardiac MR images.

Figure 2. Short axis views of a mouse heart at A) end-diastole and B) end-systole and of a human heart at C) end-diastole and D) end-systole.
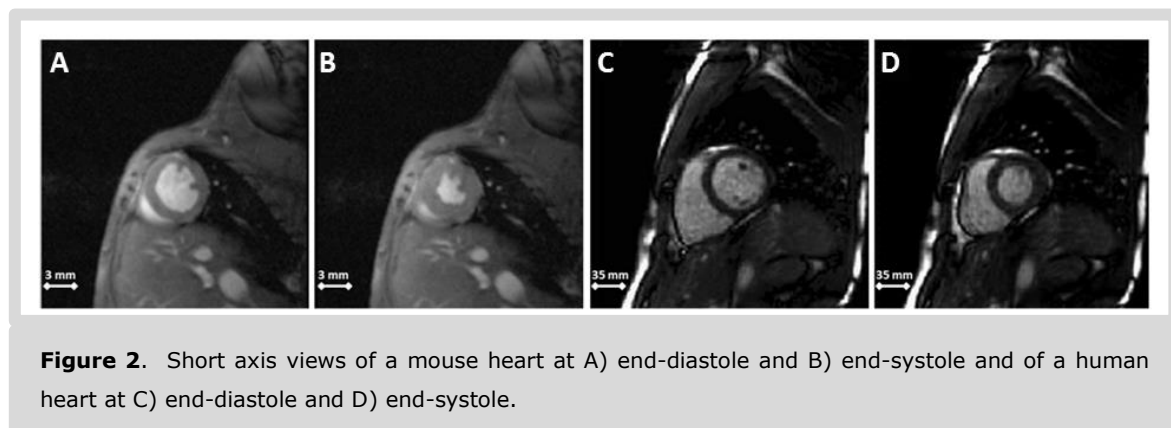
1.3   Cardiac MRI Strategies

a. Murine Cardiac MRI Acquisition Setup

Extracting the functional parameters of the heart is carried by measuring series of images at different time points during the cardiac cycle. Thus, measurements to find the accurate location and orientation of the heart are mandatory for accurate measurements. The

procedure for finding the different chamber views in human MRI cannot be directly applied to the mouse heart because the mouse heart differs in geometry from the human heart. The main difference is that the right ventricle of the mouse heart is positioned at the upper part of the left ventricle. However, in the human heart the right and left ventricles are positioned at almost the same height between base and apex. Most of the parameters defining myocardial function can be deduced from measurements of the end-systolic and end-diastolic volumes. Thus short-axis and long-axis views of the heart are required. The short-axis view shows cross-sections of the left and right ventricle that are useful for volumetric measurements. The short axis view is chosen such that a series of slices perpendicular to the long axis of the LV are obtained.

The procedure for finding the different chambers is usually started by accurate planning of the long-axis through the mouse heart. From this long-axis, the short-axis as well as other long-axis, and two- or four-chamber view orientations can be found easily. The planning of the different planes is always done on the basis of the image collected at the end-diastolic heart phase. Fig. 3 shows a schematic diagram of the mouse heart with the short- and long-axis views.

b. Data Acquisition and Animal Handling

Horizontal bore magnets with field strengths up to 15 Tesla are commercially available for small animal MR research, with bore diameters typically ranging between 10 and 30 cm. The advantage of high field magnets is that the sensitivity of MR measurements increases approximately linearly with field strength. However, the costs of ultra-high field instruments are very high and therefore most small animal cardiovascular MR is done at systems with 7 and 9.4 Tesla magnets. Another important aspect of the hardware specifications of small animal MR instruments are the maximal gradient strengths, switching rates and duty cycles that are provided by the linear magnetic field gradients. These specifications among others strongly affect the minimal echo time (TE) and

repetition time (TR) that can be achieved and thus the scan duration. Depending on the inner diameter maximal gradient amplitudes typically range from 100 to 1,000 mT/m. Similarly vital to data quality and flexibility in pulse sequence design is the choice of radio-frequency (RF) coils. A major topical advance in RF coils for small animal cardiovascular MR is the construction of phased-array coils for accelerated imaging. The development of parallel imaging techniques has revolutionized the field of human MR and has recently also found its way to preclinical MR research.

Figure 3. A) A mouse heart showing the different chambers, and the MRI views for the B) short, C) 4-chamber-, and D) 2-chamber long-axis views.
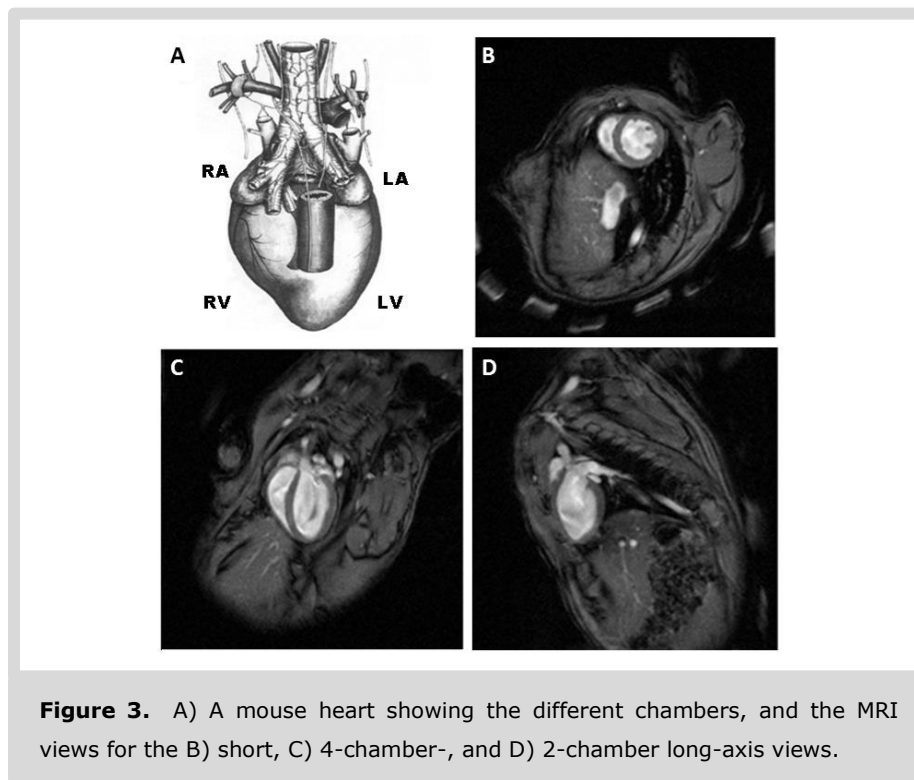
During the MRI session, the temperature and the anesthesia should be constantly monitored and controlled in order to keep the subject physiologically stable during the scan [9]. Temperature should be kept stable around 36-37°C using a heating blanket or heated air, typically monitored using a rectal probe. The level of anesthesia strongly influences the respiration rate [10]. Commonly animals are anesthetized using inhalation anesthesia (Isoflurane in oxygen or medical air).

c. Cardiac triggering and respiratory gating

To obtain a series of artifact-free images for a moving object such as the beating heart, triggering the sequence to the cardiac and respiratory motion is crucial. Conventional prospective triggering is conducted where the ECG is measured using electrodes, while respiratory movements are monitored with a pressure balloon placed on the mouse abdomen. The ECG signal, most commonly the R-peak, synchronizes the MR scanner pulses and acquisition window during imaging to cardiac activity. In prospective ECG triggered Cine-MRI, the time of repetition (TR) of pulse sequence mainly determines the highest frame rate that can be achieved [11].

Alternatively, with the retrospective triggering strategy, data is acquired continuously, asynchronous with the cardiac cycle, thus maintaining a steady-state of the MRI signal as shown in Fig. 4. After acquisition is completed, the cine movie is reconstructed by binning the data into a specified number of cardiac frames and data affected by respiratory activity is discarded.

Different strategies have been proposed to retrospectively assign each k-line to the correct cardiac time point, and to determine respiration intervals. The assignment can be done by: (a) parallel recording of the physiological signals, (b) by acquiring a navigator signal from a specific slice to extract the cardiac and respiratory cycle information at the cost of increased TE [11, 12], or (c) when using specific acquisition strategies like radial imaging [12-14], the center point in the k-space that is recorded each TR can be used for self-gating purposes as shown in Fig. 5. In this scenario, cardiac triggering and respiratory gating is therefore derived directly from the radial readout with the shortest possible TE and TR.

Retrospective triggering sometimes might be problematic due to poor navigator signals that might be present in mice with severely compromised cardiac function. Nonetheless, retrospective triggering becomes more popular because of its practical ease of use.
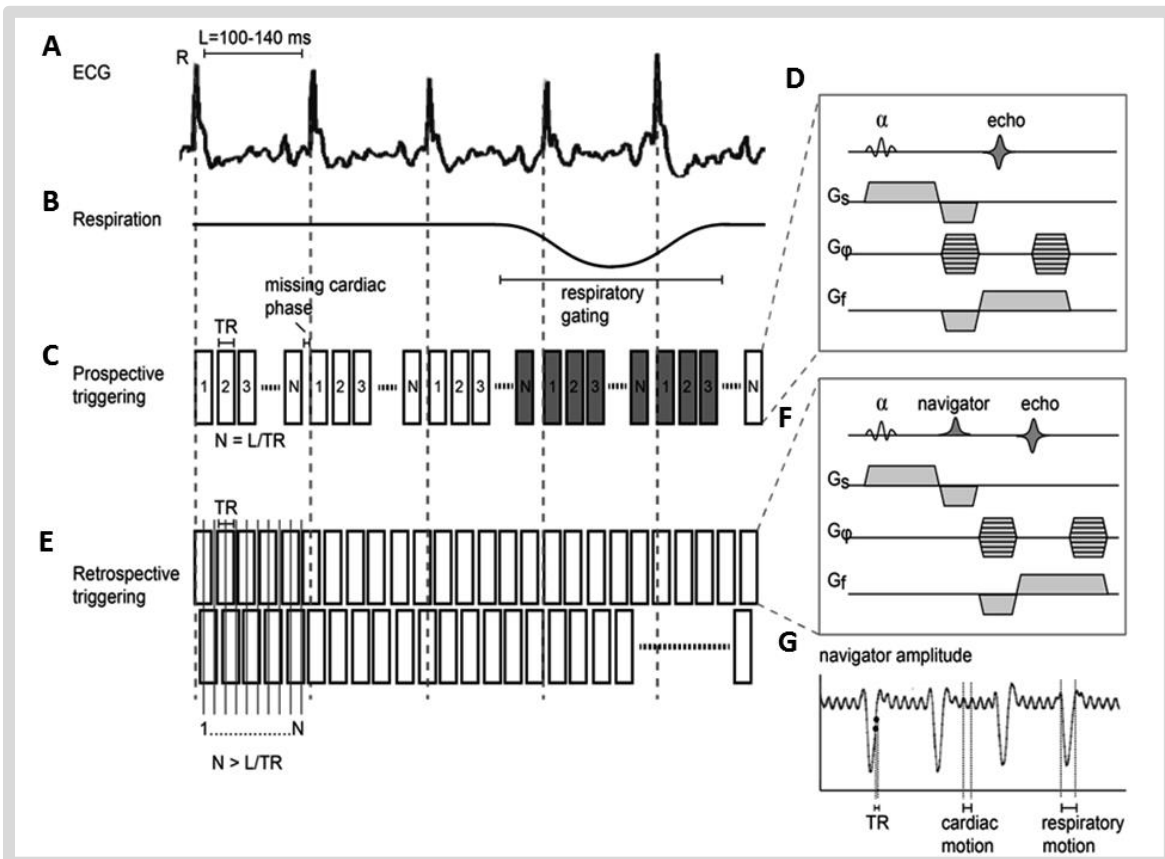
Figure 4. Strategy to synchronize cine MRI acquisition with cardiac cycle. (A) ECG and (B) respiratory signal, recorded externally using ECG electrodes and pressure balloon, respectively. (C) In the prospective triggering scheme, the acquisition is synchronized with the external ECG signal. (D) FLASH sequence typically used with prospective triggering. (E) In the retrospective triggering scheme, data is acquired continuously, asynchronously with the cardiac activity. (F) The FLASH sequence is modified to include the acquisition of a navigator signal (representative navigator signal amplitude is shown in G). The navigator signal is used to retrospectively bin the data into a number of frames N for cine reconstruction. Continuous data acquisition, with small variations in the cardiac cycle, creates high probability that data is acquired at different positions within each cardiac cycle (as illustrated by the two rows in E).

1.4 Cardiac MRI Sequences

When applied to murine animal models of myocardial diseases, MRI provides a unique technique to get detailed longitudinal information on disease progression [15, 16]. This has made a substantial contribution to the understanding of cardiac disease. Nevertheless, there are considerable experimental limitations to small animal

cardiovascular MRI. The small size of the murine heart requires high imaging gradients that may lead to ECG distortions and unreliable cardiac and respiratory triggering. The high heart rate and high blood flow velocities result in residual movement artifacts in the images. Moreover, full heart coverage requires lengthy acquisitions when using traditional MRI methods [17-19].

Figure 5. In the self-gated sequence, the navigator is either A) derived from the first data point of each acquisition in radial readout, or B) from a navigator slice, which increases the minimum TR.
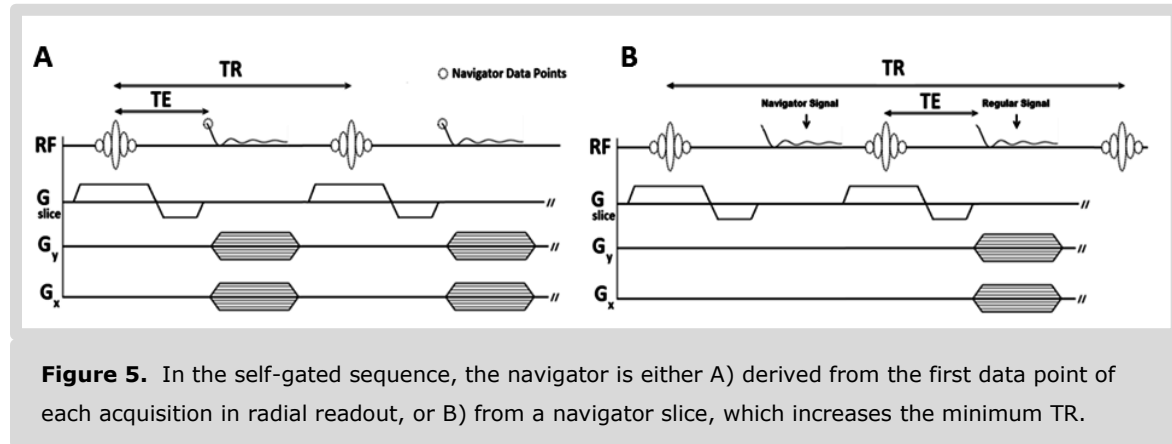
Therefore, effort has been put in optimizing MRI protocols specifically for the mouse heart. MRI allows for high spatial resolution imaging making it possible to accurately assess cardiac functional parameters, e.g. end-diastolic volume (EDV), end-systolic volume (ESV), ejection fraction (EF) and wall thickening [20], as well as regional heart wall motion and myocardial strain using tagged MR images [21]. Most of the cardiac function parameters can be determined based on low temporal resolution imaging, where a small set of time frames are obtained by ECG-triggering. However, recently it was proven that diastolic function assessment requires high frame-rate cardiac imaging [22-23].

Currently, Cinematic (Cine) MRI is the gold standard for measurement of cardiac function in mice and humans, because of its excellent endogenous soft tissue contrast and its high spatial and temporal resolution [24]. The most common parameters derived from cine MRI are the parameters for systolic function. From the segmentation of the left ventricular (LV) myocardium and cavity (Fig. 6A), LV myocardial mass, end-diastolic volume (EDV), and end-systolic volume (ESV) can be derived. From this data, systolic

function parameters can be calculated, such as stroke volume (SV) = EDV-ESV, ejection fraction (EF) = (EDV-ESV)/EDV, and cardiac output = SV x heart rate.

Next to systolic function, diastolic function is also an important parameter in cardiac function. Diabetic or obesity-related cardiomyopathy is often preceded by diastolic dysfunction [25]. Furthermore, heart failure can also occur with preserved systolic function, while diastolic function is reduced [26]. The diastolic phase of the cardiac cycle is characterized by two separate filling phases: the early filling (E) phase, which is due to active LV relaxation, and the late filling (A) phase, which is due to atrial contraction. The E rate, A rate, as well as the E/A ratio are commonly determined by echocardiography. Unfortunately, the time resolution of cine MRI in most cases is too low to separate the two diastolic filling phases. The two diastolic filling phases can only be differentiated when using ~50-60 frames/cardiac cycle [27] (Fig. 6B and C).

The time resolution in the prospective triggering method is constrained by the TR. For the gradient echo sequence, TR is limited by the lengths of the excitation pulse, the amplitude of the spatial encoding gradients, spoiler gradients, and echo readout. TR therefore becomes constrained by the desired spatial resolution, gradient performance, and SNR. At a given spatial resolution, TR can only be made shorter at the expense of a shorter excitation pulse with a higher slice selection gradient, shorter and higher spatial encoding and spoiler gradients, and a shorter echo readout with higher readout gradient and higher receiver bandwidth. However, gradient rise-time and strength are hardware limited, and increasing the gradient strength may cause gradient duty cycle problems. Also, a higher receiver bandwidth will lead to lower SNR. Therefore, to achieve the high time resolution required for diastolic function assessment, a high-performance gradient system is necessary, such as used in the study of Stuckey et al. of diabetic murine models [27]. As an alternative strategy to obtain high time-resolution cine MRI data, retrospective triggering with a long acquisition time is implemented. As reported in this thesis, we showed that the retrospective triggering method allows the reconstruction of up to 90 frames/cardiac

cycle, which enabled the identification of subtle impairments in diastolic function in diabetic mice [22, 23].

Figure 6. Analysis of cine MRI for the quantification of cardiac systolic and diastolic function. A) Series of short-axis images at different cardiac phases. Blue and red represent the segmentation of the myocardium and LV cavity, respectively, from which end diastolic volume (EDV) and end systolic volume (ESV) can be quantified. B) LV cavity volume-time curve, in which the early (E) and late peak diastolic filling (A) phases are visible. Red lines indicate the slopes/the rates of the diastolic filling. C) The first derivative of the LV cavity volume-time curve in (B), depicting the LV ejection rate (PER), early peak filling E rate (E), and late peak filling A rate (A).

Signal voids and ghosting due to rapid blood flow are the most pronounced artifacts in the standard Cine MRI acquisition of the murine heart. Additionally, susceptibility artifacts near the lungs and liver may result in local signal loss. Both types of artifacts can be mitigated by decreasing the echo time (TE). However, in the established Cine sequence TE cannot be chosen adequately short due to image resolution requirements and bandwidth limitations [28]. A solution to flow and susceptibility related artifacts can be found in the use of an ultra-short echo time (UTE) sequence [29-30]. The use of a radial readout shortens TE considerably and enables artifacts free Cine of the murine heart as shown in Fig. 7 [14, 29].

Measuring blood flow rates and profiles could be achieved through Phase Contrast (PC) MRI that employs a pair of symmetric bipolar gradients between signal excitation and readout to label the phase of the MRI signal [31, 32]. The net phase effect of the gradient pair on flowing spins is linearly proportional to the flow velocity, while zero for static spins. Both the flow direction and the range of flow velocities to which the sequence is sensitized can be selected by the choice of the direction, amplitude and duration of the linear magnetic field gradient. The absolute phase of the MRI signal is affected by many different factors.

Figure 7 [12]. Comparison between cardiac (A, C) UTE and (B, D) FLASH MRI images at mid and end diastole, respectively. Using UTE sequence, blood flow and susceptibility artefacts, normally present in FLASH images (B, D), are avoided.
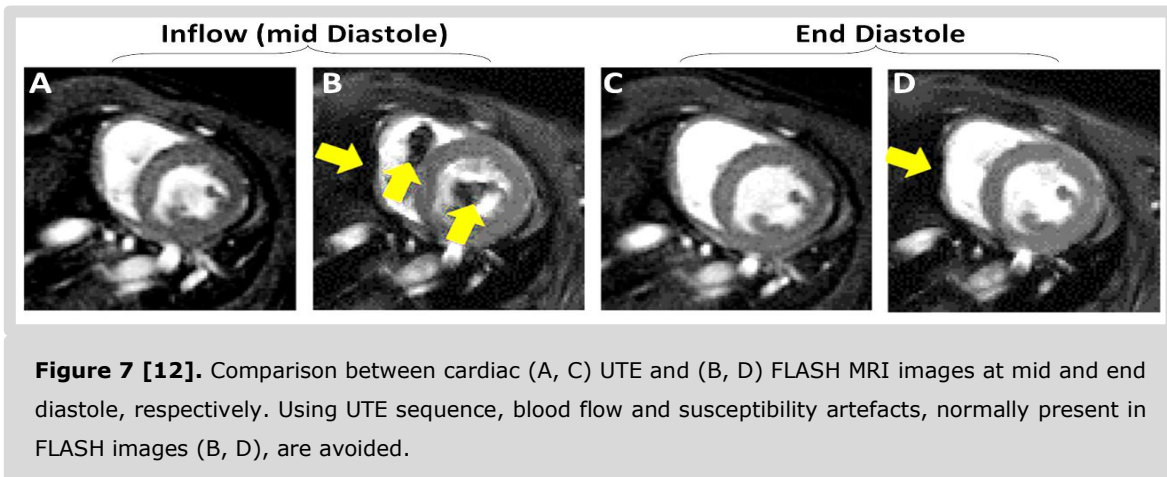
To cancel the background phase noise, the effects of static magnetic field inhomogeneity, etc., and single out the wanted phase effects of the bipolar gradient pair, a minimum of two acquisitions is needed in which the polarity of the gradient pairs is reversed. In order to resolve the blood flow velocity field in 3D, multiple acquisitions with gradient pairs played out in different spatial directions are needed, which substantially prolongs the scan times. Moreover, a prolonged measurement normally results in less accuracy due to, for instance, subjects' movement during scanning. Pelc et al. proposed a novel flow encoding scheme in which there are only four experiments required to measure the flow information in the three orthogonal directions [33]. Despite the improved efficiency of flow measurement, PC MRI is still a lengthy modality, especially in the context of clinical practices.

Therefore, most often scans are planned perpendicular to the flow direction and flow encoding is only done parallel to the main direction of flow. TR's are typically between 5 and 15 ms, with TE's as short as possible. It should be noted that the gradient-based velocity encoding inherent to PC MRI inevitably prolongs TE's.

PC MRA has been applied to small animals particularly in the setting of vascular diseases. It was used in apo-E deficient mice to quantify 2D blood flow velocities in the carotid arteries and used these to estimate wall shear stresses, in view of their importance in atherosclerotic plaque formation [34]. Herold et al. used similar PC MRA approaches to quantify pulse wave velocities in the ascending and descending aortae of wild type and apo-E knock out mice [35].

Maximizing the contrast between healthy and infarcted tissue is important for accurate quantification of the infarcted area. However, delineation of the infarct area is complicated due to a low CNR between the cardiac tissue and the LV blood. The same occurs in ultra-short echo times imaging due to the used short echo time that reduces the contrast between the blood and myocardium. Black-blood imaging has been used to enhance the contrast between blood and myocardium. A well stablished method for blood suppression is the application of one or more saturation slices at the base of the heart, saturating the magnetization of inflowing blood [36, 37], as shown in Fig. 8. Saturation is most efficient in 3D imaging, because of the repeated 3D volume excitations.

1.5   Towards Faster Acquisition

Imaging speed is an important consideration in magnetic resonance imaging (MRI). However, MRI scanners often operate at the limits of potential imaging speed as the acquisition speed is constrained by hardware performance (such as gradient amplitudes and slew rates), physiological factors and the available signal-to-noise per unit time. Therefore, faster imaging can only be achieved by a reduction in the amount of acquired data by skipping some of the data that are normally acquired. However, when data is

acquired at sub-Nyquist resolution or rates, images corrupted with undersampling artifacts are generated. The field of accelerated MRI deals with how to mitigate aliasing and produce artifact free images and movies.

If the underlying images show a predictable pattern, estimating the missing information becomes feasible. Many techniques have been developed to uncover the underlying predictability or redundancy and to utilize it to recover the missing data.

Figure 8. [37] A 3D volume was scanned to cover the entire left ventricle and consisted of 20 slices. (A) The upper, thicker slice used as navigator slice in retrospectively triggered imaging, or as saturation slice to obtain black-blood images by choosing flip angle = 90˚, as shown in (B).
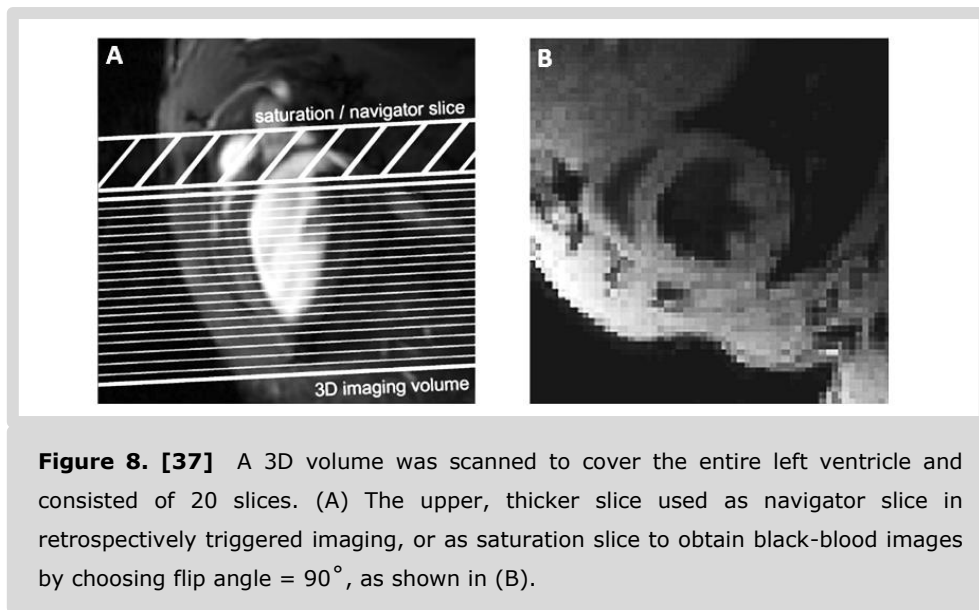
In MRI, the data is collected in what is called a k-space matrix. This k-space could be a 2-D or a 3-D matrix depending on the dimensionality reconstructed image from the object undergoes the MR scan. Each acquired MR signal represents a line in a k-space, where images are reconstructed at the end after acquiring all the k-space data. K-space represents the spatial frequencies of an image. k-t space is an extension of k-space with an additional time axis, t.

Several reconstruction techniques for accelerated imaging have been developed which differ in their strategy how to recover or estimate the missing data. Basically, these techniques fall in one of three main categories. First, methods aim to make the artifacts

less visually apparent by an incoherent or weighted acquisition. Also, data may be shared between acquisitions and zero-filling may be applied. Examples in this family of methods are radial undersampling, key-hole imaging, and partial Fourier imaging. A drawback to this strategy is loss of spatiotemporal resolution, reduced SNR, and residual artifacts. Second, methods that use parallel imaging (pMRI) scan, i.e. using multiple coils as signal receivers, to partially replace phase encoding steps and then eliminate the effect of undersampling whether by "un-aliase" the image or directly recover the missing lines in k-space. The pMRI reconstruction methods can be classified into two groups. Those in which the reconstruction takes place in image space such as in sensitivity encoding (SENSE), and those in which the reconstruction procedure takes place in k-space such as generalized autocalibrating partially parallel acquisition (GRAPPA). In this family of techniques, coil sensitivity information is required, which can be derived either by means of a pre-scan or by means of a few additionally acquired k-space lines (auto-calibration). A third class of methods exploits spatio-temporal redundancy in the image or movie and a non-linear optimization algorithm to reconstruct artifact free images from undersampled data, without the need for multiple receiver coils. Examples of this class of methods are k-t-principle component analysis (k-t-PCA) and compressed sensing (CS).

In all these cases the goal of acceleration is to permit higher spatial resolution, increased temporal resolution, shorter scan duration, or a combination of these benefits. In this section, the major image acceleration techniques that are successfully applied in the preclinical setting are briefly discussed.

a. Sensitivity Encoding (SENSE)

The SENSE reconstruction is perhaps the most frequently used parallel imaging technique [38]. Its basic principle relies on unfolding the aliasing in the image domain given that the coil sensitivity maps are known. Consider an image that is undersampled in k-space by skipping some k-space lines. The undersampling in k-space results in aliasing in the image domain as shown in Fig. 9A. The image can be unfolded by combining the aliased images

from multiple coils and the coil sensitivity maps, since every pixel in the aliased images is a superposition of different pixels at specific locations in the full FOV image weighted by the coil sensitivity maps at those locations as shown in Fig. 9B.

SENSE provides reduction in the scan time with arbitrary coil configurations, however, at the expense of SNR loss, which depends on the level of acquisition reduction and a spatially dependent geometry factor (g), which describes the underlying geometry of the coil array. SENSE reconstruction is feasible as long as the reconstruction problem is a determined system, i.e. the number of pixels that contribute to a specific pixel in the aliased image and need to be separated is less than or equal to the number of coils in the receiver array.

The use of SENSE for accelerating self-gated CMR in mice was demonstrated in [39] using a 4-element (2x2) phased array receiver coil with 3-fold acceleration. High spatial resolution at sufficiently high contrast to noise ratio (CNR) was obtained in short scan times without compromising the accuracy of estimated structural and functional parameters of the mouse heart.

b. GeneRalized Autocalibrating Partially Parallel Acquisitions (GRAPPA)

GRAPPA is a k-space based reconstruction technique [40]. One of the k-space properties is that the signal intensity in a given location is generated by applying phase or frequency encoding, which is normally produced by magnetic field gradients, to the MR signal. GRAPPA is a generalized implementation of the Simultaneous Acquisition of Spatial Harmonics (SMASH) technique [41]. The basic concept in using SMASH is that a linear combination of coil sensitivities can directly generate missing phase-encoding steps by imposing a phase shift to the MR signal, which would normally be performed by using phase-encoding magnetic field gradients.

However, in GRAPPA, a set of linear weights is used to reconstruct missing k-space points from the acquired neighborhood k-space points. The weights are estimated using a kernel for fitting k-space points from multiple receivers to a single coil Auto-Calibration signal (ACS), as schematically shown in Fig. 9C. This procedure is repeated for every receiver coil separately. After estimating all the missing k-space points in the different coils, the final image is reconstructed using a sum of squares combination of the individual coil images. GRAPPA is beneficial in cases when extraction of accurate coil sensitivity maps is difficult. Also, there is some flexibility, e.g. in the size of the kernel for better weights estimation, to tweak the reconstruction and provide good quality images. Accelerated imaging of inflow of contrast agent to quantify myocardial perfusion using GRAPPA was demonstrated in [42]. GRAPPA acceleration enabled sufficient temporal and spatial resolution to capture the first pass of a Gd-DTPA bolus through the mouse myocardium. With a measurement time of <2 minutes, a time series of 250 images was acquired, where each image was acquired in a segmented fashion over three consecutive heart beats. Missing k-lines were recovered using GRAPPA reconstruction with an effective acceleration factor of 1.64.

The GRAPPA concept was extended to also incorporate the time domain using a kernel for estimating missing data simultaneously in the k-t domain. Using kt-GRAPPA a complete cardiac functional study could be conducted in less than 3 minutes with up to 4-fold acceleration [43]. In another study, using an eight channel receiver coil, 3-fold acceleration was achieved using two- and three-dimensional sequences combined with GRAPPA to quantify global cardiac function, T1-relaxation times and infarct sizes [44].

c. SpatioTemporal Redundancy Techniques

Various dynamic imaging methods have been developed through the last years, which exploit spatiotemporal correlations to achieve higher frame rate, or shorter scan duration, since these dynamic images exhibit significant correlations in k-space and time. For some of these reconstruction techniques it is assumed that nearby data are similar and can be recovered using interpolation techniques. Others use low spatial resolution training data,

with full temporal resolution, to deduce the temporal correlation that can be used to recover the missing data. Examples of the latter are the Broad-use Linear Acquisition Speed-up Technique (k-t BLAST) [45] and temporally constrained reconstruction using principal component analysis (k-t PCA) [46].
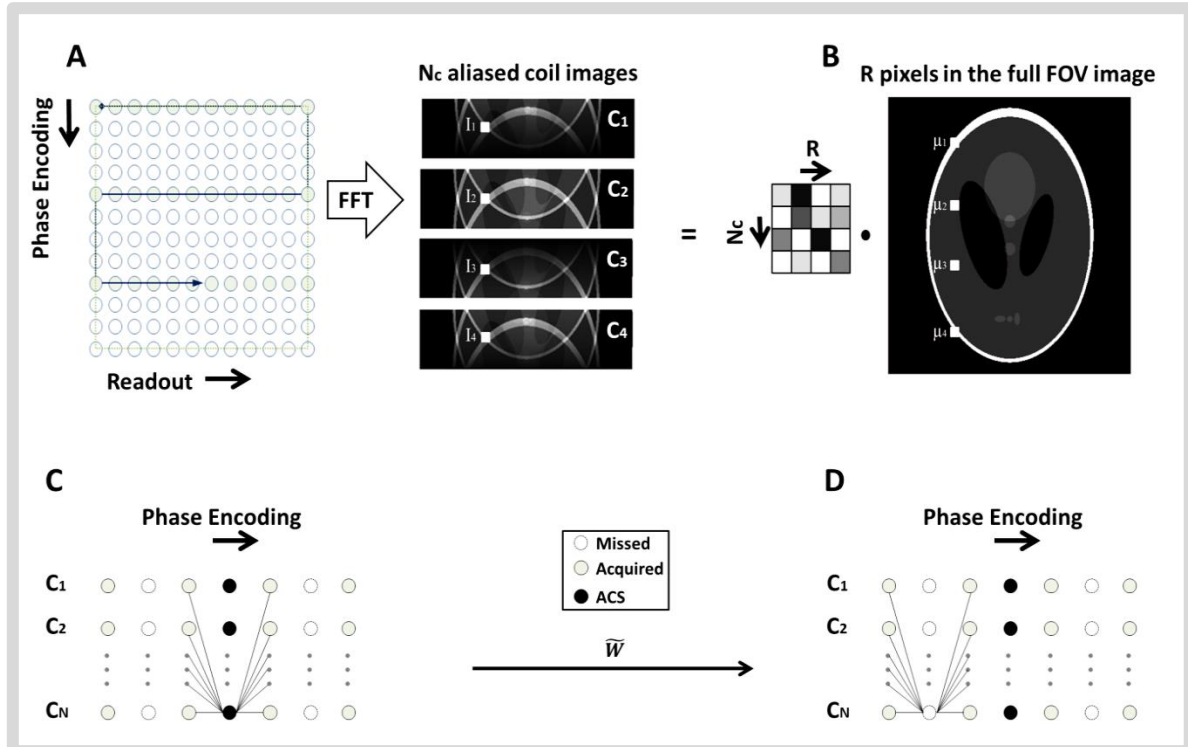
Figure 9. A) SENSE acquisition with acceleration factor R, here R=4. By skipping k-space lines and apply inverse Fourier transformation, aliased with reduced field of view images in all the receiver coils will be produced. B) Each aliased pixel in the different coils images is a superposition of a number of different pixels, depending on the reduction factor, in the full FOV multiplied by the sensitivity values of the coils at those pixels locations in the Full FOV image. By solving this inverse problem, the pixels in the Full FOV could be accurately recovered. C) Schematic diagram of the GRAPPA kernel for estimating missing k-space points. Weighting factors are determined by fitting one ACS point at one coil, here at coil=C_N, from multiple acquired points at this coil as well as the other different receiver coils. After this fitting process, the weighting parameters, $\widetilde{W}$, can be calculated and D) subsequently used to calculate the missing k-points from the neighbourhood k-space sampled points.

In these two techniques a central part of k-t-space with full sampled time points is acquired as a source of training data, while on the other hand, accelerated, undersampled, scans are acquired with full temporal and spatial resolutions. In k-t-BLAST

both reconstructed data, the training and the undersampled data, could be converted to x-f space (x = spatial axis, f = temporal frequency), where the training data provides a low-spatial-resolution x-f space which is used to extract information reflecting the temporal correlations. However, the undersampled data produces an aliased x-f space because of undersampling. Using the training data, and by knowing the undersampling pattern, recovering the aliased signal in the undersampled data becomes possible. k-t SENSE is an extension of k-t BLAST and incorporates parallel imaging in the signal recovery process. k-t PCA is very similar to k-t BLAST. However, the basic difference is that instead of reconstructing the data in x-f space, the reconstruction process takes place in the x-PC space, where PC stands for principle components, by applying principle component analysis in the time direction. The k-t-PCA shows higher performance compared to k-t-BLAST in application that exhibiting broad range of temporal frequencies. This enables achieving higher acceleration factors with better reconstruction quality. Fig. 10A shows a schematic diagram for k-t-BLAST and k-t-PCA techniques.

kt-BLAST was applied for cardiac MRI in healthy and infarcted mice with 3-fold acceleration [47]. Dynamic imaging of hyperpolarized 13C labeled pyruvate and its downstream products lactate and bicarbonate in rat heart in vivo was achieved with kt-PCA and 5-fold undersampling [48]. Hyperemic first-pass perfusion MRI during vasodilator stress in mice was achieved at 3T with 10-fold undersampling and kt-PCA reconstruction [49].

d. Compressed Sensing (CS)

A complementary mathematical framework to reconstruct images from highly undersampled data is compressed sensing [49]. This technique enables scan acceleration by taking advantage of intrinsic redundancy (sparsity) in the MR images themselves, which makes it possible to acquire only a small portion of data and recover artifact-free images afterwards. For CS MRI to work, briefly, three requirements need to be fulfilled. First, the data to be reconstructed should be sparse, i.e. compressible, which means that it could be

compactly described in the spatial domain or in other transform domain e.g: discrete cosine, Fourier, wavelet, or finite difference domain. Moreover, the undersampling acquisition trajectory should lead to incoherent, noise-like, aliasing artifacts. This could be achieved through random sampling of the raw data. As a consequence, the compressed signal stands well above these resulted incoherent diffused undersampling artifacts. Then by cleaning up the signal in an iterative manner, the compressed signal could be separated from the undersampled artifacts by using a non-linear reconstruction algorithm utilizing both the image sparsity and the acquired raw data (Fig. 10B).

In model based compressed sensing technique [50], the signal is allowed to be sparse with respect to an overcomplete dictionary learned from a data model, where the acquired data could be described by a model with few parameters. Representing the signal with respect to overcomplete dictionaries instead of the commonly used orthonormal bases as sparsifying transforms, improve the sparsity significantly.

CS reconstruction was used to accelerate the assessment of left ventricular systolic function in mice at 4.7 T [51]. Time accelerations of 6- and 12-fold were achieved using rectilinear and radial acquisitions, respectively. In several other studies compressed sensing was used to accelerate Cine functional assessment of the mouse heart [23, 52-53], where it has been shown that time accelerations up to 15-fold in global cardiac functional imaging at 7T and 9.4T was achievable.

Model-based CS method for fast cardiac T1 mapping at high spatial resolution in the mouse heart using single channel surface coil at 7T was reported by exploiting the sparsity of the signals in the T1 recovery direction, where an acceleration factor of two was achieved [54].

Higher acceleration factors could be obtained by combining CS and parallel imaging techniques. Based on CS theory and by incorporating parallel imaging techniques and sensitivity profiles, techniques like k-t SPARSE-/SENSE [56] and l1-SPIRIT [57] were

proposed. In k-t SPARSE, the random variable density undersampling generates high incoherent artifacts that could be eliminated from the true signal through an iterative process. The signal recovery is carried in the x-f space. SPIRIT stands for Iterative self-consistent parallel imaging reconstruction. It is heavily based on GRAPPA, however the reconstruction process is formulated as an optimization problem that estimates a solution consistent with the calibration and acquired data. l1-SPIRIT adds some data penalties that incorporate prior data knowledge, for example TV penalty, has been proposed.
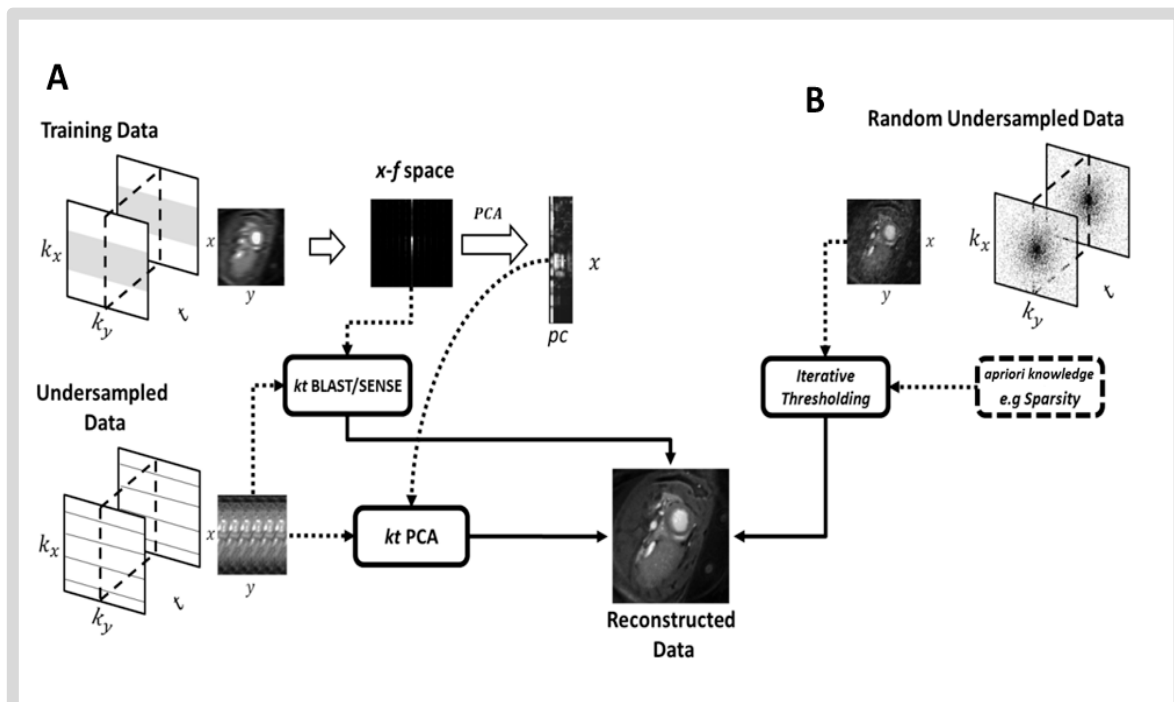
Figure 10. A) Schematic diagram of k-t-BLAST and k-t-PCA techniques. Low resolution training data as well as undersampled data with full spatial and temporal resolutions are acquired. From the training data, temporal correlations could be deducted. This will guide the reconstruction afterwards to produce artefacts free images. In k-t-PCA, transforming the temporal frequency to the principle components domain using principle component analysis, results in achieving higher acceleration factors. B) Schematic diagram of the compressed sensing reconstruction pipeline. Through random sampling, images with incoherent artefacts are produced. Extracting clean signal can be done through iterative process, given that some apriori knowledge about the data is known, e.g. related to sparstiy.

1.6   Conclusions

In conclusion, seeking improved noninvasive monitoring of patients with heart disease is stimulating the development of novel MR imaging strategies for visualizing and quantitatively assessing the cardiovascular status. Recent advances in murine cardiac MRI have made a substantial contribution to the understanding of the pathophysiology of myocardial infarction, the cardiac remodeling processes and heart failure [57-60]. Future improvements in imaging hardware and sequences are necessary to cope with the difficult tradeoff between temporal and spatial resolution when imaging the small and fast beating mouse heart. Scan time reduction in small animal MRI is also desired, particularly if one wants to combine different protocols in the same session, e.g. Cine MRI, T1 mapping, T2 mapping and perfusion imaging. Novel strategies are explored that increase overall MR efficacy, including retrospective imaging, parallel imaging and reconstruction algorithms for undersampled data.

Several MRI and MRS acceleration techniques have been developed in the past years for in vivo cardiac applications in rodents. Basically, the acceleration is achieved by skipping some data that are normally acquired. However, this leads to image artifacts, and the role of these acceleration techniques is to estimate the missing/skipped data. For mild artifacts, most of the techniques seek a variable-density sampling with dense sampling at the center of the k-space that contains most of the signal information. Also, using non-Cartesian readout results in benign artifacts compared to those generated when using the Cartesian sampling. However, they are more demanding computationally. Using acceleration techniques helps in reducing the scan time tremendously while still achieving high spatial or high temporal resolution data. As a consequence, accurate assessment of the cardiovascular status in short acquisition times becomes possible. The research presented in this thesis is centered on innovations in the field of mouse cardiac MRI, building on and inspired by the topics discussed in this chapter.

1.7 Outline of this thesis

The research described in this thesis focuses on MRI of the mouse heart, and more specifically on developing strategies to accelerate the MRI measurements. Self-gated sequences were used in all the projects presented in this thesis, since the self-gated strategy allows more flexibility for scan acceleration than the prospective triggering strategy. Chapter 2 shows the application of compressed sensing reconstruction to accelerate the acquisition of the recently developed retrospectively triggered high temporal resolution MR sequence to measure diastolic function in mice. Chapter 3 focuses on flow-artifact-free imaging of mouse heart using ultra short echo time MRI, and also exploits the benefits of radial trajectory used in the data acquisition to achieve high acceleration factors using compressed sensing reconstruction. In Chapter 4, we aimed for volume acquisition and phase contrast imaging to estimate blood flow velocity. The acquired phantom data has a very high spatial resolution in the slice direction leading to accurate quantification of blood flow profiles. In chapter 5, a clinical feasibility study is presented that shows the successful application of compressed sensing reconstruction in high temporal resolution pulse wave velocity measurements in human carotids. This thesis ends with a general discussion and some future perspectives in Chapter 6.

References

1.   Einthoven, W. and J. Wieringa, *Ungleichartige Vaguswirkungen auf das Herz, elektrokardiographisch untersucht.* Pflügers Archiv European Journal of Physiology, 1912. **149**(1): p. 48-64.
2.   Gibbons, R.J., P.A. Araoz, and E.E. Williamson, *The year in cardiac imaging.* J Am Coll Cardiol, 2009. **53**(1): p. 54-70.
3.   Ross, A.J., et al., *Serial MRI evaluation of cardiac structure and function in mice after reperfused myocardial infarction.* Magn Reson Med, 2002. **47**(6): p. 1158-68.
4.   Schneider, J.E., et al., *Fast, high-resolution in vivo cine magnetic resonance imaging in normal and failing mouse hearts on a vertical 11.7 T system.* J Magn Reson Imaging, 2003. **18**(6): p. 691-701.
5.   Wiesmann, F., et al., *Analysis of right ventricular function in healthy mice and a murine model of heart failure by in vivo MRI.* Am J Physiol Heart Circ Physiol, 2002. **283**(3): p. H1065-71.
6.   Bakermans, A.J., et al., *Fasting-Induced Myocardial Lipid Accumulation in Long-Chain Acyl-CoA Dehydrogenase Knockout Mice Is Accompanied by Impaired Left Ventricular Function.* Circulation-Cardiovascular Imaging, 2011. **4**(5): p. 558-565.
7.   Slawson, S.E., et al., *Cardiac MRI of the normal and hypertrophied mouse heart.* Magnetic Resonance in Medicine, 1998. **39**(6): p. 980-987.
8.   Aikawa, E., et al., *Multimodality molecular imaging identifies proteolytic and osteogenic activities in early aortic valve disease.* Circulation, 2007. **115**(3): p. 377-386.
9.   Appleton, G.O., et al., *Determinants of cardiac electrophysiological properties in mice.* Journal of Interventional Cardiac Electrophysiology, 2004. **11**(1): p. 5-14.
10.   Kober, F., et al., *Myocardial blood flow mapping in mice using high-resolution spin labeling magnetic resonance imaging: influence of ketamine/xylazine and isoaflurane anesthesia.* Magnetic Resonance in Medicine, 2005. **53**(3): p. 601-606.
11.   Heijman, E., et al., *Comparison between prospective and retrospective triggering for mouse cardiac MRI.* Nmr in Biomedicine, 2007. **20**(4): p. 439-447.
12.   Hoerr, V., et al., *Cardiac-respiratory self-gated cine ultra-short echo time (UTE) cardiovascular magnetic resonance for assessment of functional cardiac parameters at high magnetic fields.* Journal of Cardiovascular Magnetic Resonance, 2013. **15**.
13.   Hiba, B., et al., *Cardiac and respiratory double self-gated cine MRI in the mouse at 7 T.* Magnetic Resonance in Medicine, 2006. **55**(3): p. 506-513.
14.   Motaal, A.G., et al., *Functional imaging of murine hearts using accelerated self-gated UTE cine MRI.* Int J Cardiovasc Imaging, 2014.
15.   Geelen, T., et al., *Contrast-enhanced MRI of murine myocardial infarction - part I.* NMR Biomed, 2012. **25**(8): p. 953-68.
16.   Kober, F., et al., *Cardiovascular magnetic resonance of myocardial structure, function, and perfusion in mouse and rat models.* Current Cardiovascular Imaging Reports, 2012. **5**(2): p. 109-115.
17.   Shin, T., et al., *Three dimensional first-pass myocardial perfusion imaging at 3T: feasibility study.* J Cardiovasc Magn Reson, 2008. **10**: p. 57.
18.   Peters, D.C., et al., *Undersampled projection reconstruction applied to MR angiography.* Magn Reson Med, 2000. **43**(1): p. 91-101.
19.   Thedens, D.R., et al., *Fast magnetic resonance coronary angiography with a three-dimensional stack of spirals trajectory.* Magn Reson Med, 1999. **41**(6): p. 1170-9.
20.   Schneider, J.E., et al., *How to perform an accurate assessment of cardiac function in mice using high-resolution magnetic resonance imaging.* Journal of Cardiovascular Magnetic Resonance, 2006. **8**(5): p. 693-701.
21.   Heijman, E., et al., *Magnetic resonance imaging of regional cardiac function in the mouse.* Magnetic Resonance Materials in Physics Biology and Medicine, 2004. **17**(3-6): p. 170-178.
22.   Coolen, B.F., et al., *High frame rate retrospectively triggered Cine MRI for assessment of murine diastolic function.* Magnetic Resonance in Medicine, 2013. **69**(3): p. 648-656.
23.   Motaal, A.G., et al., *Accelerated high-frame-rate mouse heart cine-MRI using compressed sensing reconstruction.* Nmr in Biomedicine, 2013. **26**(4): p. 451-457.
24.   Epstein, F.H., *MR in mouse models of cardiac disease.* Nmr in Biomedicine, 2007. **20**(3): p. 238-255.
25.   Fang, Z.Y., J.B. Prins, and T.H. Marwick, *Diabetic cardiomyopathy: Evidence, mechanisms, and therapeutic implications.* Endocrine Reviews, 2004. **25**(4): p. 543-567.
26.   Gladden, J.D., W.A. Linke, and M.M. Redfield, *Heart failure with preserved ejection fraction.* Pflugers Arch, 2014. **466**(6): p. 1037-53.
27.   Stuckey, D.J., et al., *Novel MRI method to detect altered left ventricular ejection and filling patterns in rodent models of disease.* Magn Reson Med, 2008. **60**(3): p. 582-7.
28.   Frahm, J., A. Haase, and D. Matthaei, *Rapid Nmr Imaging of Dynamic Processes Using the Flash Technique.* Magnetic Resonance in Medicine, 1986. **3**(2): p. 321-327.
29.   Robson, M.D., et al., *Magnetic resonance: An introduction to ultrashort TE (UTE) imaging.* Journal of Computer Assisted Tomography, 2003. **27**(6): p. 825-846.
30.   O'Brien, K.R., et al., *Aortic valve stenotic area calculation from phase contrast cardiovascular magnetic resonance: the importance of short echo time.* Journal of Cardiovascular Magnetic Resonance, 2009. **11**.
31.   Bernstein, M.A., K.F. King, and Z.J. Zhou, *Handbook of MRI pulse sequences*. 2004, Amsterdam ; Boston: Academic Press. xxii,1017 p.

32.   Bernstein, M.A., A. Shimakawa, and N.J. Pelc, *Minimizing Te in Moment-Nulled or Flow-Encoded 2-Dimensional and 3-Dimensional Gradient-Echo Imaging.* Jmri-Journal of Magnetic Resonance Imaging, 1992. **2**(5): p. 583-588.

33.   Pelc, N.J., et al., *Encoding strategies for three-direction phase-contrast MR imaging of flow.* J Magn Reson Imaging, 1991. **1**(4): p. 405-13.

34.   van Bochove, G.S., et al., *MRI-determined carotid artery flow velocities and wall shear stress in a mouse model of vulnerable and stable atherosclerotic plaque.* MAGMA, 2010. **23**(2): p. 77-84.

35.   Herold, V., et al., *In Vivo Measurement of Local Aortic Pulse-Wave Velocity in Mice With MR Microscopy at 17.6 Tesla.* Magnetic Resonance in Medicine, 2009. **61**(6): p. 1293-1299.

36.   Nieman, B.J., K.U. Szulc, and D.H. Turnbull, *Three-Dimensional, In Vivo MRI With Self-Gating and Image Coregistration in the Mouse.* Magnetic Resonance in Medicine, 2009. **61**(5): p. 1148-1157.

37.   Coolen, B.F., et al., *Three-dimensional T1 mapping of the mouse heart using variable flip angle steady-state MR imaging.* NMR Biomed, 2011. **24**(2): p. 154-62.

38.   Pruessmann, K.P., et al., *SENSE: sensitivity encoding for fast MRI.* Magn Reson Med, 1999. **42**(5): p. 952-62.

39.   Ratering, D., et al., *Accelerated cardiovascular magnetic resonance of the mouse heart using self-gated parallel imaging strategies does not compromise accuracy of structural and functional measures.* Journal of Cardiovascular Magnetic Resonance, 2010. **12**.

40.   Griswold, M.A., et al., *Generalized Autocalibrating Partially Parallel Acquisitions (GRAPPA).* Magnetic Resonance in Medicine, 2002. **47**(6): p. 1202-1210.

41.   Coolen, B.F., et al., *Mouse Myocardial First-Pass Perfusion MR Imaging.* Magnetic Resonance in Medicine, 2010. **64**(6): p. 1658-1663.

42.   Schneider, J.E., et al., *Ultra-fast and accurate assessment of cardiac function in rats using accelerated MRI at 9.4 Tesla.* Magnetic Resonance in Medicine, 2008. **59**(3): p. 636-641.

43.   Schneider, J.E., et al., *Accelerated Cardiac Magnetic Resonance Imaging in the Mouse Using an Eight-Channel Array at 9.4 Tesla.* Magnetic Resonance in Medicine, 2011. **65**(1): p. 60-70.

44.   Tsao, J., P. Boesiger, and K.P. Pruessmann, *k-t BLAST and k-t SENSE: Dynamic MRI with high frame rate exploiting spatiotemporal correlations.* Magnetic Resonance in Medicine, 2003. **50**(5): p. 1031-1042.

45.   Pedersen, H., et al., *k-t PCA: Temporally Constrained k-t BLAST Reconstruction Using Principal Component Analysis.* Magnetic Resonance in Medicine, 2009. **62**(3): p. 706-716.

46.   Marshall, I., et al., *Application of kt-BLAST acceleration to reduce cardiac MR imaging time in healthy and infarcted mice.* Magnetic Resonance Materials in Physics Biology and Medicine, 2014. **27**(3): p. 201-210.

47.   Weiss, K., et al., *Accelerating hyperpolarized metabolic imaging of the heart by exploiting spatiotemporal correlations.* Nmr in Biomedicine, 2013. **26**(11): p. 1380-1386.

48.   Jogiya, R., et al., *Hyperemic stress myocardial perfusion cardiovascular magnetic resonance in mice at 3 Tesla: initial experience and validation against microspheres.* Journal of Cardiovascular Magnetic Resonance, 2013. **15**.

49.   Lustig, M., D. Donoho, and J.M. Pauly, *Sparse MRI: The application of compressed sensing for rapid MR imaging.* Magnetic Resonance in Medicine, 2007. **58**(6): p. 1182-1195.

50.   Doneva, M., et al., *Compressed Sensing Reconstruction for Magnetic Resonance Parameter Mapping.* Magnetic Resonance in Medicine, 2010. **64**(4): p. 1114-1120.

51.   Buonincontri, G., et al., *Functional assessment of the mouse heart by MRI with a 1-min acquisition.* Nmr in Biomedicine, 2014. **27**(6): p. 733-737.

52.   Wech, T., et al., *Accelerating Cine-MR Imaging in Mouse Hearts Using Compressed Sensing.* Journal of Magnetic Resonance Imaging, 2011. **34**(5): p. 1072-1079.

53.   Montesinos, P., et al., *Application of the Compressed Sensing Technique to Self-Gated Cardiac Cine Sequences in Small Animals.* Magnetic Resonance in Medicine, 2014. **72**(2): p. 369-380.

54.   Li, W., M. Griswold, and X. Yu, *Fast cardiac T1 mapping in mice using a model-based compressed sensing method.* Magnetic Resonance in Medicine, 2012. **68**(4): p. 1127-1134.

55.   Otazo, R., et al., *Combination of Compressed Sensing and Parallel Imaging for Highly Accelerated First-Pass Cardiac Perfusion MRI.* Magnetic Resonance in Medicine, 2010. **64**(3): p. 767-776.

56.   Lustig, M. and J.M. Pauly, *SPIRiT: Iterative Self-consistent Parallel Imaging Reconstruction From Arbitrary k-Space.* Magnetic Resonance in Medicine, 2010. **64**(2): p. 457-471.

57.   Yang, Z.Q., et al., *Simultaneous evaluation of infarct size and cardiac function in intact mice by contrast-enhanced cardiac magnetic resonance imaging reveals contractile dysfunction in noninfarcted regions early after myocardial infarction.* Circulation, 2004. **109**(9): p. 1161-1167.

58.   Bohl, S., et al., *Advanced methods for quantification of infarct size in mice using three-dimensional high-field late gadolinium enhancement MRI.* American Journal of Physiology-Heart and Circulatory Physiology, 2009. **296**(4): p. H1200-H1208.

59.   Waghorn, B., et al., *Monitoring dynamic alterations in calcium homeostasis by T-1-weighted and T-1-mapping cardiac manganese-enhanced MRI in a murine myocardial infarction model.* Nmr in Biomedicine, 2008. **21**(10): p. 1102-1111.

60.   Sosnovik, D.E., et al., *Magnetic resonance imaging of cardiomyocyte apoptosis with a novel magneto-optical nanoparticle.* Magnetic Resonance in Medicine, 2005. **54**(3): p. 718-724.

Accelerated High Frame Rate Murine Heart Cine MRI Using Compressed Sensing Reconstruction

As you go, you will make mistakes of your own ...

Related Articles:

➤ Motaal, A. G., Coolen, B. F., Abdurrachim, D., Castro, R. M., Prompers, J. J., Florack, L. M. J., Nicolay, K. and Strijkers, G. J. (2013), Accelerated high-frame-rate mouse heart cine-MRI using compressed sensing reconstruction. NMR Biomed., 26: 451–457.

➤ Coolen, B. F., Abdurrachim, D., Motaal, A. G., Nicolay, K., Prompers, J. J. and Strijkers, G. J. (2013), High frame rate retrospectively triggered Cine MRI for assessment of murine diastolic function. Magn Reson Med, 69: 648–656.

Abstract

For accurate assessment of the left ventricular diastolic function using Cine MRI, a high frame rate is required. We introduce a new protocol to obtain very high frame-rate Cine MRI movies of the beating mouse heart within reasonable measurement time. The method is based on a self-gated accelerated FLASH acquisition and compressed sensing reconstruction. Key to our approach is that we exploit the stochastic nature of the retrospective triggering acquisition scheme to produce an undersampled and random k-t-space filling that allows for compressed sensing reconstruction and acceleration. As a standard, a self-gated FLASH sequence with a total acquisition time of 10 min was used to produce single-slice Cine movies of 7 mouse hearts with 90 frames per cardiac cycle. 2X and 3X k-t-space undersampled Cine movies were produced from 2.5 and 1.5 min data acquisitions. The accelerated 90-frames Cine movies of the mouse hearts were successfully reconstructed with a compressed sensing algorithm. The movies had high image quality and the undersampling artifacts were effectively removed. Left ventricular functional parameters, i.e. end-systolic and end-diastolic lumen surface areas and early-to-late filling rate ratio (E/A) ratio as a parameter to evaluate diastolic function, derived from the standard and the accelerated Cine movies were nearly identical.

2.1   Introduction

Magnetic Resonance Imaging (MRI) of heart anatomy and function is an important diagnostic tool to study the heart in mouse models of myocardial disease [1-4]. Functional parameters, such as end-systolic volume (ESV), end-diastolic volume (EDV), ejection fraction (EF) and cardiac output (CO), are derived from a dynamic series of images through the cardiac cycle (Cine). Commonly, Cine MR images of the fast beating mouse heart (400 - 600 bpm) are recorded with a relatively low frame rate (typically less than 25 frames per cardiac cycle), and this is because the speed of acquisition is constrained by hardware performance (gradient amplitudes and slew rates) and available signal-to-noise per unit time [5].

However, a significant drawback of low frame-rate Cine evaluation of heart function is that details on myocardial motion during the phases of systolic contraction and diastolic relaxation go undetected [6-8]. For example, during diastole, filling of the left ventricle (LV) occurs in two phases – the early filling (E) phase as a result of LV relaxation followed by late filling induced by atrial contraction (A) – and these two phases cannot be distinguished unless high temporal resolution (high frame rate) Cine imaging is conducted [9, 10]. E and A denote the peak filling rates of the two phases. Alteration of the E/A ratio is widely accepted as a clinical marker of diastolic heart dysfunction [6, 9]. In rats and mice, the E and A diastolic filling phases were previously quantified using ECG-triggered Cine MRI with a frame rate of 62 frames/cardiac cycle using short repetition time (TR = 2.4 ms) [11].

In a recent publication, we described quantification of the E and A diastolic filling phases of mouse hearts using a self-gated Cine MRI with a frame rate of >80 frames/cardiac cycle [10]. High frame rates were achieved by acquiring k-lines with constant TR asynchronously with the cardiac and respiratory cycle. Synchronization was performed retrospectively from a navigator echo that was incorporated in the imaging sequence and is sensitive to

the heart and respiratory motion [10, 12-14]. However, a significant drawback of the method was the long acquisition time. The reason for the long acquisition time is that a classical Fourier transform reconstruction requires a completely filled k-space for each Cine frame, which may take very long for high spatial-resolution and high frame-rate Cine movies due to the stochastic nature of k-space filling with the retrospective approach. For example, acquisition of a single-slice 93 frames Cine movie of a mouse heart with high number of averages (NA ≈ 13) took approximately 25 min. Therefore, acceleration of this self-gated high frame rate Cine technique is highly desired.

In this chapter we introduce a new self-gated Cine MRI protocol for measuring high frame rate movies of the mouse heart within a much shorter acquisition time. Acceleration of the method is achieved with a compressed sensing (CS) reconstruction algorithm [15-17]. Unique to our approach is that we exploit the stochastic nature of the retrospective triggering acquisition scheme to produce an undersampled and random k-t-space filling that allows for CS reconstruction and acceleration. With this strategy mouse cardiac Cine MRI is demonstrated with very high frame rates (90 frames/cardiac cycle) within much shorter acquisition times of typically 2.5 and 1.5 min, which roughly corresponds to 2X and 3X undersampled k-t-spaces. The acquired k-lines, on average, stochastically, are measured with 1-2 averages. The technique was validated by comparing the compressed sensing reconstructions with standard long acquisition time Cine movies.

2.2   Materials and Methods

2.2.1   In vivo measurements

The local institutional animal care committee (Maastricht University, Maastricht, The Netherlands) reviewed and approved all experimental procedures. During imaging, mice were sedated by inhalation of 1 - 2% isoflurane in medical air (0.4 l/min). Temperature was maintained at 36 - 37 $^\circ$C with a heating pad and monitored using a rectal probe. After

the MRI experiment, the mice were killed by cervical dislocation. A total of N = 7 healthy mice (C57BL/Ks mice) were included in the experiment.

2.2.2   MRI protocol

Scanning was performed with a 9.4 T Bruker animal scanner (Bruker BioSpin MRI GmbH, Ettlingen, Germany). The gradient system allows a maximal gradient strength of 740 mT/m with a slew rate of 6600 T/m/s. A 4-element mouse cardiac phased-array surface receive coil was used in combination with a 72-mm-diameter volume transmit coil (Bruker BioSpin). To determine the orientation of the short axis, several scout images were acquired in the transverse plane and the long-axis plane of the left ventricle at the start of each examination. The location of the central short-axis slice was planned halfway between the apex and base.

A single-slice FLASH sequence with a navigator echo was used [10, 18]. Sequence parameters were: Gaussian-shaped RF pulse of 300 μs; flip angle = 15°; TR = 4.7 ms; TE = 2.35 ms; bandwidth = 150 kHz; field of view = 3 x 3 cm^2; acquisition matrix (NF x NP) = 192 x 128; reconstruction matrix = 192 x 192; slice thickness = 1 mm; number of repetitions (NR) = 1000. The resulting total acquisition time was NR x NP x TR ≈ 10 min. The resulting k-space trajectory was under-sampled with a factor 1.5 corresponding to 64 auto-calibration signal (ACS) lines in the center of k-space. The navigator echo analyses were done retrospectively with homebuilt software in Matlab 8.1 (The Mathworks, Natick, MA, USA) using a local maximum detection algorithm to determine the start of the cardiac cycle. K-lines acquired during respiration (~30% of the data) were discarded. No sharing of k-lines between frames or interpolation was applied. Images from the 4 coil elements were reconstructed individually and subsequently combined using a sum-of-squares method weighted by fixed coil sensitivities. The coil sensitivities were pre-calibrated using a homogeneous agar phantom.

All Cine movies were reconstructed with 90 frames, well above the number for which accurate determination of diastolic function in mice was demonstrated by others [10, 11]. The effective number of averages for the standard Cine movies acquired in 10 min was NA ≈ 4.3. The under-sampled data was taken from the first 2.5 and 1.5 min of the fully sampled data. Reconstructions of 2.5 and 1.5 min acquisition time movies, roughly corresponding to 2X and 3X under-sampling, were done by CS reconstruction as explained below.

2.2.3 CS reconstruction

Originating from the field of information theory and approximation, the CS theory has recently found application in MRI [16]. Briefly, CS aims to accurately reconstruct a signal from a small subset of random linear combinations of signal samples. For MRI this means that we could achieve accurate image reconstructions by only measuring a small subset of k-space. However, there are some requirements that have to be satisfied for successful CS image reconstruction [15, 16]. First, the desired data needs to be compressible, which means that the data has a sparse representation in a transform domain. Image data can be sparse represented in e.g. the finite-difference, the wavelet or discrete cosine transform domain. Second, aliasing artifacts due to k-space under-sampling have to be incoherent (noise-like) in the transform domain. Random undersampling has been proposed as an acceleration method because it produces incoherent or low-coherent artifacts [20, 21]. The coherence can be defined as the maximum off-diagonal element in a normalized point spread function (PSF) for the k-space trajectory used, which measures the tendency of linear reconstruction to leak energy from the underlying source pixel to other pixels, or equivalently as the side lobe to principal peak ratio [16]. Finally, a nonlinear reconstruction has to be applied to enforce sparsity of the image and consistency with the acquired data.

In Cine MRI, static tissue and background regions are sparsely represented in the temporal frequency domain. Besides, the quasi-periodicity of myocardial activity has a sparse temporal Fourier transform. Additionally, a single voxel is sparsely represented by spatio-temporal total variation. The spatio-temporal total variation is given by:

$$\text{TV(m)} = \sqrt{|\Delta_x(m)|^2 + |\Delta_y(m)|^2 + |\Delta_t(m)|^2} \qquad (2.1)$$

where m is a voxel, Δ_x, Δ_y and Δ_t are the finite difference in the frequency, phase and time directions. The difference operator used for the TV is one sided difference. For example, Δ_x (m) is calculated by:

$$\Delta_x(m) = m(x+1, y,\ t) - m(x, y,\ t) \qquad (2.2)$$

In this work we exploit both temporal and spatial sparsity using these sparse transformations.

Due to the stochastic nature of the retrospective triggering acquisition, a random under-sampled k-t-space is achieved, which – as will be demonstrated – satisfies the CS reconstruction requirement of incoherent undersampling artifacts. Fig. 1A schematically illustrates the acquisition of k-lines asynchronously with the periodic cardiac motion. The k-lines are binned in cardiac frames of duration γ, which results in a random filling of k-space for a small number of repetitions (NR = 150). The random filling is different for each of the 90 frames, which introduces a random sampling in the time direction as well (Fig. 1B).

The resulting k-t-space, sampled at significantly sub-Nyquist rates (up to 4X), is reconstructed with a non-linear compressed sensing algorithm. Mathematically, the following constrained optimization problem is solved:

$$min\ ||\partial(m)||_1\ subject\ to\ ||F_s m - y||_2 < \epsilon \qquad (2.3)$$

where m is the reconstructed Cine movie, ∂ is the sparse transformation (temporal and spatial sparse transformations), F_s is the sampled Fourier transform corresponding to a given undersampling scheme, y is the measured k-space data, and ϵ controls the fidelity of the reconstructed to the measured data, where it is set to be the expected noise level.

Figure 1. The self-gated acquisition scheme. A) K-lines are acquired asynchronously with the periodic cardiac motion. Retrospectively, k-lines are collected in bins of length γ using the cardiac triggering and respiratory gating information from a navigator echo. Small variations in cardiac cycle length ensure that TR is not a multiple of the R-R interval as indicated with Δ, leading to time-shifted acquisition of k-lines and a random filling of k-space. B) kt-space after a small number of shots (NR = 150), illustrating the random filling.

The objective function is the ℓ1 norm that promotes sparsity. The constrained optimization problem in Eq.2.3, could be reformulated as unconstrained optimization form by solving the Lagrangian l_1-minimization problem:

$$min_m\{\ ||F_sm - y||_2{}^2 + l\ ||\partial(m)||_1 + TV\ (m)$$
(2.4)

where TV is the total variation penalty, and ℓ is a regularization parameter that determines the trade-off between data consistency and sparsity. Several methods for solving Eq. 4 have been proposed in literature [22-24]. In this work, we use a modified

version for the ℓ_1 penalized nonlinear conjugate gradients and backtracking line-search method as described by Lustig et al. [16].

2.2.4   Data analysis

To validate CS reconstructions of the high frame rate Cine movies, the root-mean-square errors (RMSe) between full and undersampled datasets were calculated. The RMSe was calculated by

$$RMSe = \frac{\sum_{i=1}^{n} (S_i - S_i')^2}{n} \tag{2.5}$$

where S_i and S_i' are the gold standard and estimated reconstructions at voxel i respectively, and n is the number of voxels of the Cine image. Additionally, heart functional parameters (end-systolic LV lumen surface area, end-diastolic LV cavity lumen surface area, LV lumen surface area-time curves correlation and E/A ratio) of the under-sampled CS reconstructions were compared to the standard datasets. Global heart parameters were calculated using a semi-automatic segmentation with the software Segment (version 1.8 R1145, http://segment.heiberg.se). To avoid large errors in surface area determination, contours were manually corrected for the papillary muscle area. The E/A ratio was calculated by taking the time derivative for the LV lumen surface area as a function of time. Agreement in LV lumen surface area and E/A between fully sampled, 2X and 3X under-sampled data sets were graphically assessed using Bland-Altman analysis.

2.3   Results

Fig.2 shows the k_y-t sampled trajectory for representative cases after 1.5 and 2.5 min scans with the corresponding point spread functions. As shown, the kt-space is randomly sampled. The elevated side lobes at the edges of the point spread functions occur because of the GRAPPA-Like acquisition. Further improvements are feasible as will be addressed in the discussion section. It is clear that the point spread function after the 2.5 min scan has

decreased side lobes compared to the point spread function after 1.5 min scan. The incoherence values for the 7 mice were 0.35 ± 0.014 and 0.35 ± 0.007 for the 1.5 and 2.5 min scans, respectively.

For each mouse, 10 min acquisition was used to obtain the standard dataset, to which the newly proposed accelerated acquisitions were subsequently compared.

Figure 2. Incoherence Measurements. The k_y-t sampled trajectory for a representative case after A) 1.5 and B) 2.5 min scans and the corresponding C, D) PSFs.
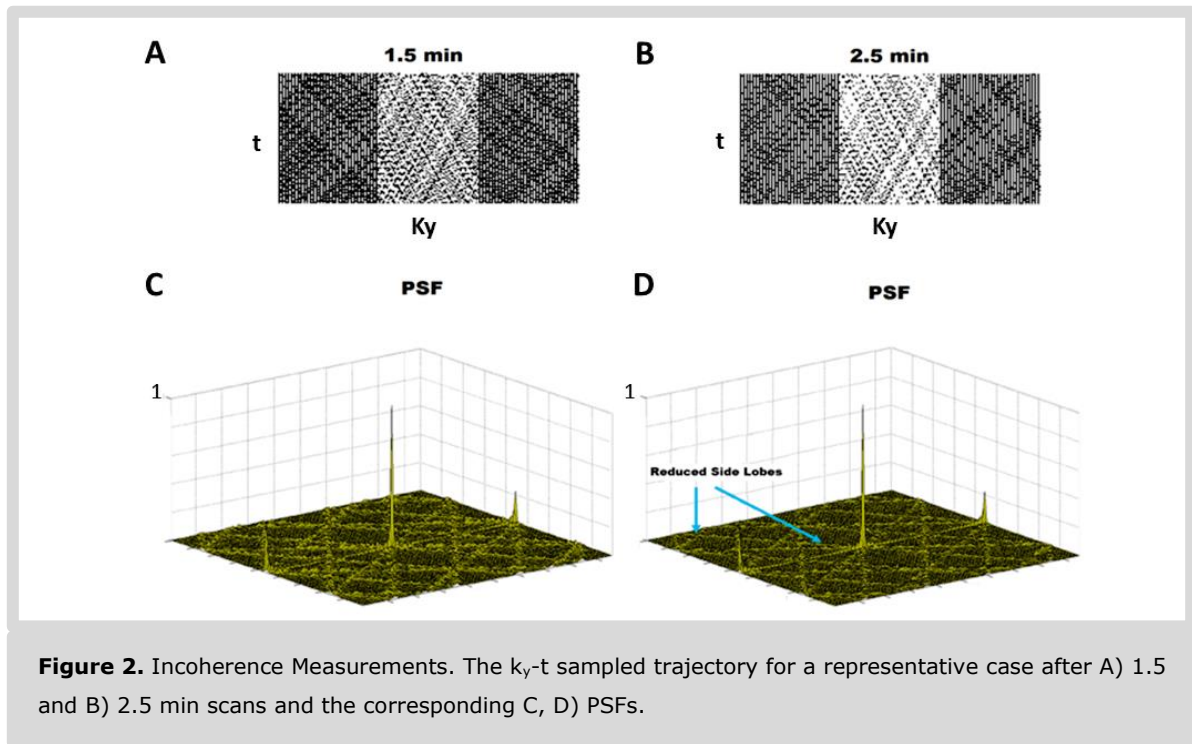
Fig. 3 shows still frames at end-diastole, mid-systole and end-systole for the standard reconstruction, compared with the corresponding 2X-, 3X- and 4X-accelerated CS reconstructions and the corresponding difference maps. The image quality of the standard acquisition was nearly recovered for the 2X and 3X CS accelerations. Image quality of the 4X-accelerated movies was visually judged insufficient for evaluation. We therefore limited further analyses to the 2X and 3X accelerated movies. The CS reconstruction recovered a good quality image of the heart in which the endocardium, epicardium and papillary muscles were well distinguished. To assess the quality of the CS reconstruction more quantitatively for the 7 mice, the RMSe between the CS

reconstructions using the standard reconstructions as a gold standard was measured using Eq.5. The RMSe were 5.0% ± 0.8% and 6.0% ± 0.6% for the 2X and 3X CS reconstructions, respectively.

To evaluate the effect of CS reconstruction on derived heart functional parameters, the LV lumen surface area at end-systole and end-diastole of standard and CS reconstructions were compared in Bland-Altman plots for 2X and 3X under-sampling factors as shown in Fig. 4. For the end-diastole lumen surface area, differences were almost equally distributed around small bias values of 2.1% and 2.8% with 95% observation intervals of [-6.5%, 10.6%] and [-6.7%, 12.3%] for the 2X and 3X under-sampled datasets, respectively. For the end-systole lumen surface area, differences were also almost equally distributed around small bias values of 2.5% and 2.9% with 95% observation intervals of [-10.2%, 15.1%] and [-16.9%, -10.2%] for the 2X and 3X under-sampled datasets, respectively.

Figure 3. Accelerated CS reconstructions of high frame-rate Cine movies. End-diastolic, mid-systolic and end-systolic frames of a standard acquisition, and 2X-, 3X- and 4x-accelerated CS reconstructions. The second, fourth and sixth columns show the difference images with the standard reconstruction. All the images have the same intensity scale.
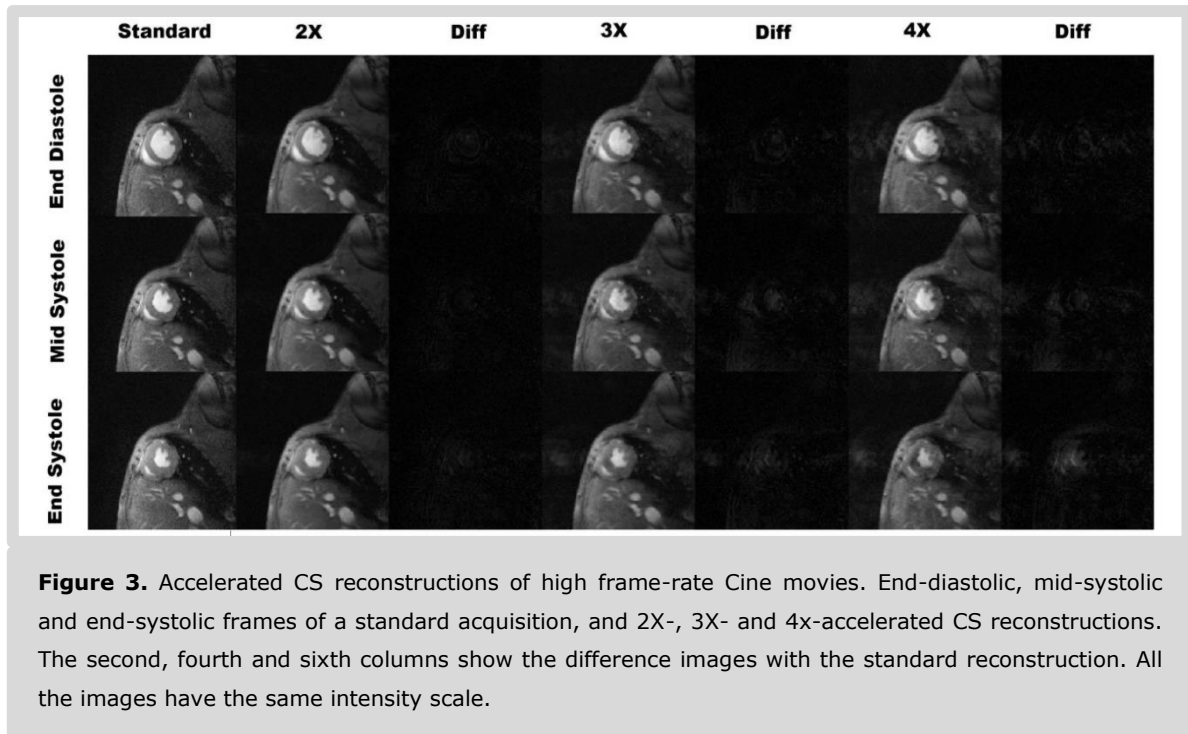
The correlation coefficients for the lumen surface area-time curves of the 2X and 3X under-sampled datasets compared to the standard datasets of are 0.986 ± 0.007 and

0.975 ± 0.015, respectively. Finally, the LV lumen surface area versus time curves and filling-rate versus time curves for standard and 2X and 3X accelerated CS reconstructions were compared. A representative example (Fig. 5) shows that the curves correspond very well throughout the cardiac cycle. The E/A ratio's of the 2X and 3X CS reconstructions were analyzed with respect to the standard acquisition in a Bland-Altman graph (Fig. 6). Differences in E/A values for 2X and 3X were centered on a bias of 5% and 6% with 95% observation intervals of [-3.1%, 13%] and [-3.5%, 15.6%] for the 2X and 3X under-sampled datasets, respectively.
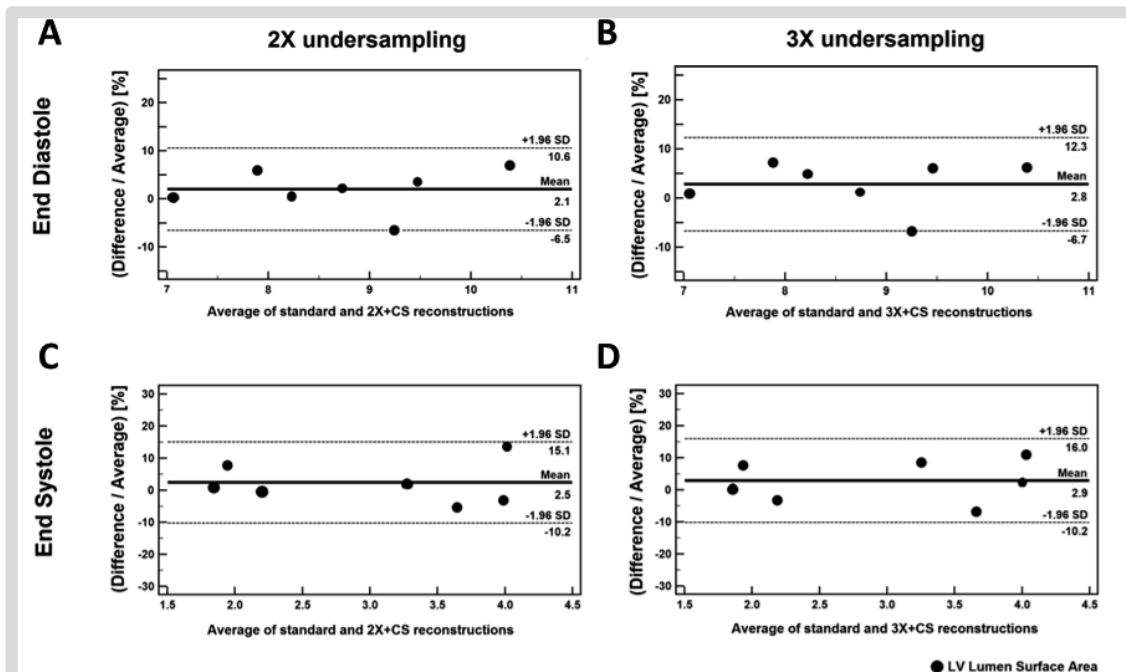
Figure 4. Bland-Altman analysis of LV lumen surface area at end-systole and end-diastole. Comparison between standard and 2X-accelerated CS acquisitions at A) end-diastole and B) end-systole. Comparison between standard and 3X-accelerated CS acquisitions at C) end-diastole and D) end-systole.

2.4   Discussion

Compressed sensing reconstruction facilitates accurate image reconstructions of highly undersampled accelerated acquisitions. It provides an elegant and effective way to speed up the cardiac MRI measurements as an alternative or in addition to parallel imaging by

multi-coil arrays. CS has been successfully demonstrated in many MRI applications [16] and was found particularly useful in cardiac imaging where imaging speed is a prerequisite [25-27]. Recently, CS was also implemented to speed up regular ECG-triggered mouse cardiac Cine MRI and for rapid T_1 mapping of the mouse myocardium [17, 28-29].
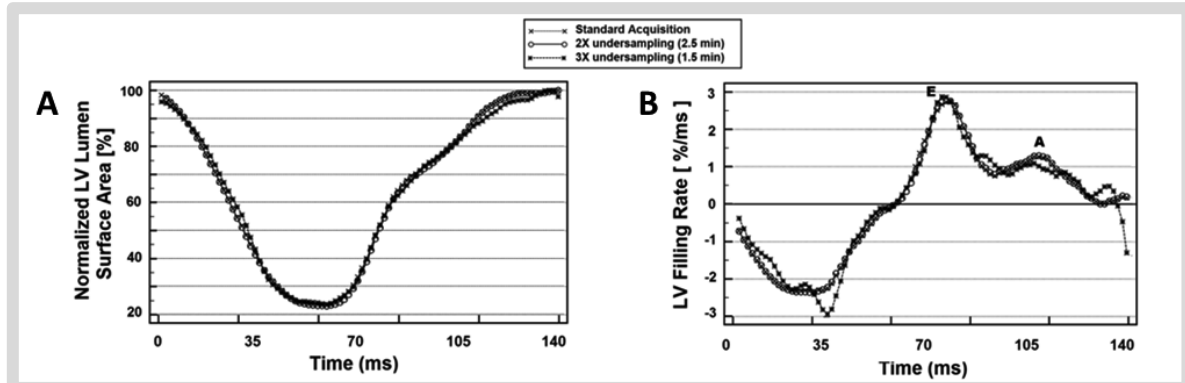
Figure 5. Normalized LV lumen surface area and ejection-rates. A) Normalized LV lumen surface area as function of time through the cardiac cycle for standard, 2X and 3X-accelerated CS reconstructions for a representative mouse. B) Corresponding ejection-rates, showing E and A peak filling rates.
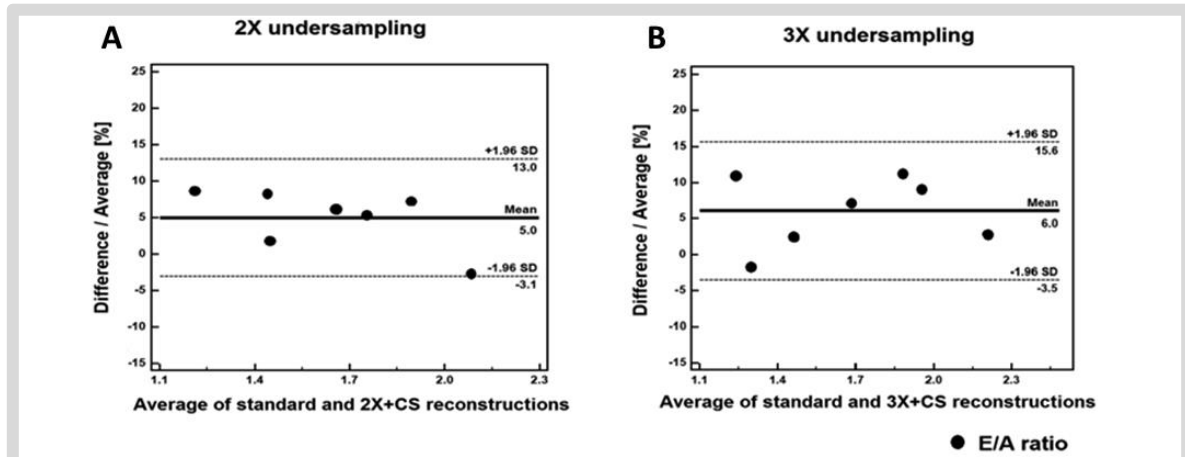
Figure 6. Bland-Altman analysis of E/A ratio. Comparison between standard and A) 2X- and B) 3X-accelerated CS acquisitions.

Cine CMR with high temporal resolution well below the TR can be achieved using a self-gated acquisition. However, the statistical nature of k-space filling and binning of cardiac time frames results in long acquisition times to ensure that all k-lines are measured at

least once and averaging is homogeneous in k-space. Starting from a non-accelerated standard 90-frame Cine acquisition of the left ventricle with a total scan time of 10 min resulting in an effective number of averages of approximately 4.3 to ensure that all k-lines are measured, we demonstrated in this chapter that undersampling by at least a factor 3 is possible using a CS reconstruction. The accuracy of derived LV functional parameters such as end-systolic and end-diastolic lumen surface area as well as diastolic E/A filling ratios were not significantly compromised within acceptable confidence intervals.

Unique to our approach of CS acquisition and reconstruction is that we exploit the stochastic nature of the self-gated acquisition scheme to produce an undersampled and random k-t-space. Randomness results naturally from the asynchrony between the duration of the cardiac cycle and TR and thus there was no need to predefine an undersampled k-space trajectory for the different frames in the cardiac cycle. A potential drawback of this approach is that k-space is filled completely random, which would result in a rather unfavorable PSF. However, in our implementation the acquisition of additional auto-calibration signal (ACS) lines in the middle of k-space resulted in a variable density (random) filling of k-space. In other words, higher probability that most of the signal information is acquired since most of this information is located at the center of the k-space. Therefore, the incoherence was adequate to achieve 2X and 3X kt-space undersampled reconstructions.

We demonstrated that for a single slice with FOV = 3 x 3 cm^2 and in-plane pixel dimensions = 156 x 156 μm^2, reconstruction of 90 frames/cardiac cycle from 2.5 min (2X undersampling) or even 1.5 min (3X undersampling) datasets was possible. Thus multi-slice imaging of high frame rate Cine within acceptable measurement times is now feasible.

Further improvements and higher acceleration factors might be achieved by increasing the incoherence of the undersampling artifacts, which can be done by undersampling in

two dimensions rather than in one as is the case for the Cartesian sampling trajectory used here. This can be realized by radial and spiral k-space filling trajectories. In such schemes, the incoherence is maximized compared to the traditional Cartesian sampling trajectory.

By using the proposed method, the acquired k-t space cannot be fully predicted or predetermined as this depends on the heart and respiration rates of the mouse. However, because of the GRAPPA-like acquisition, there is a higher probability to acquire k-lines in the center of k-space, where most of the signal information presents. On the other side, the used acquisition strategy does not provide the optimum incoherence, as the GRAPPA like acquisition, specifically at the outer regions of the frames' k-spaces, gives elevated side peaks in the transform point spread function (TPSF). However, since a large region of the center of the k-space is acquired, under-sampling outer regions does not result in severe, coherent, artifacts.

For better incoherence, another possible solution would be to spend more time in the center of k-space to achieve a variable density filling with, for example, a Gaussian profile in k-space without GRAPPA skipping strategy. Simulation studies could be carried out to determine the optimum sampling profile compared to different heart rates. This would improve the TPSF, thus yield better CS reconstructions.

Besides these multi-slice sampling strategies, 3D volume imaging with radial readout would be more favorable for several reasons. First, the incoherence of the under-sampling artifacts in case of using random 3D radial sampling is much higher than using the random multi-slice sampling. Thus, the under-sampling artifacts are more incoherent which allows better CS reconstruction. Second, the radial readout contains motion information in itself, so compared to the pulse sequence used here, there is no need to acquire navigator echo data in every TR, which will lead to shorter imaging time.

In summary, in this chapter we presented a new self-gated Cine MRI protocol for making high frame rate movies of the mouse heart within a much shorter acquisition time. The technique exploits the retrospective triggering acquisition scheme to produce an undersampled, random k-t-space filling and CS reconstruction. 2X and 3X accelerated acquisitions were possible with high image quality and without significantly compromising the determination of the derived cardiac functional parameters.

References

1. McVeigh, E., Regional myocardial function. Cardiol Clin, 1998. 16(2): p. 189-206.
2. Ibrahim el, S.H., et al., Combined functional and viability cardiac MR imaging in a single breathhold. Magn Reson Med, 2007. 58(4): p. 843-9.
3. Watzinger, N., et al., Myocardial viability: magnetic resonance assessment of functional reserve and tissue characterization. J Cardiovasc Magn Reson, 2001. 3(3): p. 195-208.
4. Kim, R.J., et al., The use of contrast-enhanced magnetic resonance imaging to identify reversible myocardial dysfunction. New England Journal of Medicine, 2000. 343(20): p. 1445-1453.
5. Ham, C.L.G., et al., Peripheral nerve stimulation during MRI: Effects of high gradient amplitudes and switching rates. Jmri-Journal of Magnetic Resonance Imaging, 1997. 7(5): p. 933-937.
6. Oh, J.K., S.J. Park, and S.F. Nagueh, Established and Novel Clinical Applications of Diastolic Function Assessment by Echocardiography. Circulation-Cardiovascular Imaging, 2011. 4(4): p. 444-455.
7. Rettmann, D.W., et al., High temporal resolution breathheld 3D FIESTA CINE imaging: Validation of ventricular function in patients with chronic myocardial infarction. Journal of Magnetic Resonance Imaging, 2007. 25(6): p. 1141-1146.
8. Krishnamurthy, R., et al., High-temporal resolution (< 6 ms) Cine Steady-State Free Precession (SSFP) imaging for assessing LV diastolic function. Journal of Cardiovascular Magnetic Resonance, 2009. 11(Suppl 1): p. P74.
9. Diamant, M., et al., Diastolic dysfunction is associated with altered myocardial metabolism in asymptomatic normotensive patients with well-controlled type 2 diabetes mellitus. Journal of the American College of Cardiology, 2003. 42(2): p. 328-335.
10. Coolen, B.F., et al., High frame rate retrospectively triggered Cine MRI for assessment of murine diastolic function. Magnetic Resonance in Medicine, 2013. 69(3): p. 648-656.
11. Stuckey, D.J., et al., Novel MRI method to detect altered left ventricular ejection and filling patterns in rodent models of disease. Magnetic Resonance in Medicine, 2008. 60(3): p. 582-587.
12. Bishop, J., et al., Retrospective gating for mouse cardiac MRI. Magnetic Resonance in Medicine, 2006. 55(3): p. 472-477.
13. Nauerth, A., E. Heijman, and C. Diekmann. Slice refocusing signal for retrospective reconstruction of CINE cardiac MR images. in Proc. Intl Soc. Magn. Reson. Med. 2006.
14. Heijman, E., et al., Comparison between prospective and retrospective triggering for mouse cardiac MRI. Nmr in Biomedicine, 2007. 20(4): p. 439-447.
15. Donoho, D.L., Compressed sensing. Ieee Transactions on Information Theory, 2006. 52(4): p. 1289-1306.
16. Lustig, M., D. Donoho, and J.M. Pauly, Sparse MRI: The application of compressed sensing for rapid MR imaging. Magn Reson Med, 2007. 58(6): p. 1182-95.
17. Wech, T., et al., Accelerating Cine-MR Imaging in Mouse Hearts Using Compressed Sensing. Journal of Magnetic Resonance Imaging, 2011. 34(5): p. 1072-1079.
18. Frahm, J., A. Haase, and D. Matthaei, Rapid Nmr Imaging of Dynamic Processes Using the Flash Technique. Magnetic Resonance in Medicine, 1986. 3(2): p. 321-327.
19. Griswold, M.A., et al., Generalized Autocalibrating Partially Parallel Acquisitions (GRAPPA). Magnetic Resonance in Medicine, 2002. 47(6): p. 1202-1210.
20. Tsai, C.M. and D.G. Nishimura, Reduced aliasing artifacts using variable-density k-space sampling trajectories. Magnetic Resonance in Medicine, 2000. 43(3): p. 452-458.
21. Marseille, G.J., et al., Nonuniform phase-encode distributions for MRI scan time reduction. Journal of Magnetic Resonance Series B, 1996. 111(1): p. 70-75.
22. Chen, S.S.B., D.L. Donoho, and M.A. Saunders, Atomic decomposition by basis pursuit. Siam Journal on Scientific Computing, 1998. 20(1): p. 33-61.
23. Candes, E. and J. Romberg. Signal recovery from random projections. in Proc. SPIE. 2005.
24. Daubechies, I., M. Defrise, and C. De Mol, An iterative thresholding algorithm for linear inverse problems with a sparsity constraint. Communications on Pure and Applied Mathematics, 2004. 57(11): p. 1413-1457.
25. Jung, H., et al., k-t FOCUSS: A General Compressed Sensing Framework for High Resolution Dynamic MRI. Magnetic Resonance in Medicine, 2009. 61(1): p. 103-116.
26. Otazo, R., et al., Combination of Compressed Sensing and Parallel Imaging for Highly Accelerated First-Pass Cardiac Perfusion MRI. Magnetic Resonance in Medicine, 2010. 64(3): p. 767-776.
27. Gamper, U., P. Boesiger, and S. Kozerke, Compressed sensing in dynamic MRI. Magnetic Resonance in Medicine, 2008. 59(2): p. 365-373.
28. Li, W., M. Griswold, and X. Yu, Fast cardiac T1 mapping in mice using a model-based compressed sensing method. Magnetic Resonance in Medicine, 2012. 68(4): p. 1127-1134.
29. Wech, T., et al. Highly accelerated cine-MRI in mouse hearts using compressed sensing and parallel imaging at 9.4 T. in Proc. Int. Soc. Magn. Reson. Med. 2012.

Functional Imaging of Murine Hearts Using Accelerated Self-Gated UTE Cine MRI

As you go, you will make mistakes of your own

But son, that's alright ...

Related Articles:

➢ Abdallah G. Motaal ; Nils Noorman ; Wolter L. De Graaf ; Luc J. Florack ; Klaas Nicolay, Gustav J. Strijkers, Functional Imaging of Murine Hearts Using Accelerated Self-Gated UTE Cine MRI. Int J Cardiovasc Imaging. 2014 Sep 10 Doi: s10554-014-0531-8

➢ Abdallah G. Motaal ; Nils Noorman ; Wolter L. De Graaf ; Luc J. Florack ; Klaas Nicolay, Gustav J. Strijkers, Accelerated self-gated UTE MRI of the murine heart, Proc. SPIE 9038, Medical Imaging 2014: Biomedical Applications in Molecular, Structural, and Functional Imaging, 903803 (March 13, 2014); doi:10.1117/12.2043806;

Abstract

A fast protocol for Ultra-Short Echo Time (UTE) Cine MRI of the beating murine heart is presented in this chapter. The sequence involves a self-gated UTE with golden angle radial acquisition and compressed sensing reconstruction. The self-gated acquisition is performed asynchronously with the heartbeat, resulting in a randomly undersampled kt-space that facilitates compressed sensing reconstruction. The sequence was tested in 4 healthy rats and 4 rats with chronic myocardial infarction, approximately 2 months after surgery. As a control, a non-accelerated self-gated multi-slice FLASH sequence with an echo time (TE) of 2.76 ms, 4.5 signal averages, a matrix of 192x192, and an acquisition time of 2min34s per slice was used to obtain Cine MRI with 15 frames per heartbeat. Non-accelerated UTE MRI was performed with TE=0.29ms, a reconstruction matrix of 192X192, and an acquisition time of 3min47s per slice for 3.5 averages. Accelerated imaging with 2X, 4X and 5X undersampled kt-space data was performed with 1min, 30s and 15s acquisitions, respectively. UTE Cine images up to 5X undersampled kt-space data could be successfully reconstructed using a compressed sensing algorithm. In contrast to the FLASH Cine images, flow artifacts in the UTE images were nearly absent due to the short echo time, simplifying segmentation of the left ventricular (LV) lumen. LV functional parameters derived from the control and the accelerated Cine movies were statistically identical.

3.1   Introduction

Cardiovascular magnetic resonance imaging (MRI) is considered the gold standard for accurate assessment of cardiac anatomy and function [1-3]. In murine animal models of myocardial diseases MRI provides a unique technique to get detailed longitudinal information on disease progression [4, 5]. Nevertheless, there are considerable experimental limitations to small animal cardiovascular MRI. The small size of the murine heart requires powerful imaging gradients that may lead to ECG distortions and unreliable cardiac and respiratory triggering. The high heart rate and high blood flow velocities result in residual movement artifacts in the images. Moreover, full heart coverage requires lengthy acquisitions [6-8].

Signal voids and ghosting due to rapid blood flow are the most pronounced artifacts in the standard FLASH Cine MRI acquisition of the murine heart. Additionally, susceptibility artifacts near the lungs and liver may result in signal loss. Both types of artifacts can be mitigated by decreasing the echo time (TE). However, in the FLASH sequence TE cannot be chosen adequately short due to image resolution requirements and bandwidth limitations [9].

A solution to flow and susceptibility related artifacts can be found in the use of an ultra-short echo time (UTE) sequence [10, 11]. The use of a radial readout shortens TE considerably and enables artifacts free Cine of the murine heart, as was shown previously by Hoerr et al. [12]. In the latter study a self-gating technique was used for cardiac triggering and respiratory gating. Heart and respiratory movements were obtained from the center k-space point that is acquired each TR in the radial readout scheme. Movies were reconstructed by retrospectively binning data into the desired cardiac time frames [13-16]. A major drawback of this retrospective gating scheme is the long acquisition time that is needed to ensure full stochastic filling of k-space for each cardiac time frame, as each k-line has to be measured at least once. Assignment of echoes to the different k-

space time points is a random process that depends on the asynchronous timing of TR with respect to heart and respiration rates [15]. Moreover, to fulfill the radial Nyquist criterion more k-spokes need to be measured than for an equal image matrix in regular Cartesian FLASH imaging, leading to an even longer imaging time. To reduce the acquisition time, novel sparse sampling and reconstruction strategies such as compressed sensing (CS) can be employed. The radial readout scheme of the UTE sequence fits very well with the CS requirements and high acceleration factors can be achieved [17].

In this chapter, we introduce a fast protocol for multi-slice Cine MRI of the murine heart, which combines a self-gated radial UTE Cine sequence and CS reconstruction, where a golden-angle undersampling scheme is used to provide homogenous coverage and higher incoherence of the undersampling artifacts. The sequence was tested in 4 rats with chronic myocardial infarction, approximately 2 months after surgery, and 4 age-matched sham control rats. The technique was validated in a comparison to the acquired with the regular non-accelerated self-gated multi-slice FLASH sequence.

3.2   Materials and Methods

3.2.1   In vivo measurements

The local institutional animal care committee (Maastricht University, Maastricht, The Netherlands) reviewed and approved all experimental procedures. In this study, 8 male Lewis rats (Charles River, Paris, France) 12 weeks of age were used. All animals underwent surgery, where in 4 rats ligation of the left anterior descending artery (LAD) was performed to induce chronic myocardial infarction, while for the other 4 rats no knot was placed pulled in the ligation suture. During surgery animals were anesthetized using inhalation anesthesia (2-3% Isoflurane in oxygen (0.8 l/min) after intubation). Animals were placed on a heating pad and their temperature was continuously monitored by a rectal probe and maintained between 36 and 37.5 ^{o}C. To treat pain, sufentanil as an

analgesic was used during the procedure, and after recovery buprenorphine was given subcutaneously at least up till 48 hours. Animals were daily checked for weight, hydration, behavior, pain and wound healing. No animals died during or directly after the ligation procedure. Animals were housed under specific pathogen free (SPF) conditions with two per cage and were provided with food and water ad libitum. The imaging experiments were performed 2 months after the surgery. During imaging, rats were sedated by inhalation of 2 – 3% isoflurane in oxygen (0.8 l/min). Temperature was maintained at 36 – 37.5 ^{o}C with a heating pad and monitored using a rectal probe.

3.2.2 MRI protocol

Scanning was performed with a 7T Bruker animal scanner (Bruker BioSpin MRI GmbH, Ettlingen, Germany). The gradient system allowed a maximal gradient strength of 660 mT/m with a slew rate of 4570 T/m/s. A 86 mm quadrature coil (Bruker BioSpin) was used for RF transmission and a 4x1 cardiac phased array coil (Bruker BioSpin) was used for RF reception. To determine the orientation of the short axis, several scout images were acquired in the transverse plane and the long-axis plane of the left ventricle at the start of each examination.

As a reference, a standard multi-slice short axis self-gated FLASH sequence was used with 5 slices (NS=5) covering the heart from base to apex. Self-gating was performed using an in-slice navigator echo. Sequence parameters were: Gaussian-shaped RF pulse of 300 μs; flip angle = 15°; TR = 8 ms; TE = 2.76 ms; field of view = 5 x 5 cm^{2}; acquisition matrix (NF x NP) = 192 x 192; reconstruction matrix = 256 x 256; slice thickness = 1 mm; number of repetitions (NR) per slice = 100. This number of repetitions resulted in number of averages NA = 4.5 ± 0.3 on average over the 8 animals. The resulting total acquisition time was NR x NP x TR ≈ 2min34s per slice. Cine movies with 15 frames per slice were reconstructed retrospectively.

For the proposed method, a multi-slice self-gated 2D UTE sequence was implemented as schematically shown in Fig. 1A. Imaging was performed in the same geometry (short axis) and with the same number of slices (NS = 5) as for the reference datasets. Sequence parameters were: Gaussian-shaped RF pulse of 300 μs; flip angle = 15°; TR = 5 ms; TE = 0.29 ms; field of view = 5 x 5 cm^2; readout data (Number Radial Spokes (NP) x Spoke Length) = 604 x 96; reconstruction matrix = 256 x 256; slice thickness = 1 mm; number of repetitions (NR) = 75 resulting in NA = 3.4 ± 0.2 on average over the 8 animals. The resulting total acquisition time was NP x TR x NR ≈ 3min47s min per slice. The radial spokes that were sampled with golden angle angular spacing, were assigned to the corresponding time frames and Cine images were reconstructed using a non-uniform fast Fourier transform (NUFFT) [18].

The navigator echo analyses were done retrospectively with homebuilt software in Matlab 8.1 using a local maximum detection algorithm to determine the start of the cardiac cycle. K-spokes acquired during respiration (~30% of the data) were discarded. Unless stated otherwise, Cine movies were reconstructed with 15 cardiac time frames.

Shorter acquisition times were achieved by taking the first 1min, 30s, and 15s of the fully sampled data that correspond to approximately 2X, 4X, and 5X undersampled k-space data, respectively. The % k-space filling and effective number of averages varied over the animals and cardiac time frames because of the stochastic filling method. In Table 1 the different protocols are listed with the acquisition time per slice, as well as the effective k-space filling percentages and NA averaged over the 8 animals.

3.2.3 CS reconstruction

Compressed sensing (CS) has proven a valuable technique for speeding up data acquisition in MRI by exploiting the compressibility of MR images [19-22]. The ability to transform the data to a sparse representation and the radial trajectory, which is used in

Cine UTE imaging, both fit very well with the sparsity and incoherence requirements for CS.

Table 1: Acquisition time, percentage k-space filling, and effective number of averages for the different protocols

	FLASH fully sampled	UTE fully sampled	UTE 2X	UTE 4X	UTE 5X
Acquisition time	2min34s	3min47s	1min	30s	15s
k-space filling†	95.7 ± 3.1%	94.7 ± 4.1%	55.6 ± 8.1%	26.2 ± 5.6%	19.9 ± 3.9%
NA*†	4.5 ± 0.3	3.4 ± 0.2	1.50 ± 0.09	1.16 ± 0.15	1.09 ± 0.11

* NA refers to the effective number of averages for the part of the k-space that was filled.
† Values are mean ± standard deviation.

Due to the stochastic nature of the retrospective gating acquisition, a randomly undersampled kt-space was achieved. The resulting kt-space, sampled at significant sub-Nyquist rates, was reconstructed with a non-linear compressed sensing algorithm. Mathematically, the following constrained optimization problem was solved:

$$min \; ||\partial(m)||_1 \; subject \; to \; ||R^{-1}F_s m - y||_2 < \; \epsilon \qquad (3.1)$$

where ∂ is the sparsifying transformation, m is the reconstructed data, y is the measured undersampled kt-space, and Fs is the sampled Fourier transformation and R is a gridding operator that interpolates the Fourier data to radial spokes to ensure data consistency with acquired data, and ϵ controls the fidelity of the reconstructed to the measured data. For Non-uniform Fourier transformation (NUFFT), the online available Fessler toolbox was used [18]. The objective function is the ℓ1 norm that promotes sparsity. The constrained optimization problem in Eq. 1, could be reformulated as unconstrained optimization form by solving the Lagrangian ℓ1-minimization problem:

$$min_m\{ \; ||R^{-1}F_s m - y||_2^2 + \alpha \; ||\partial(m)||_1 \qquad (3.2)$$

where m is the Cine image to be reconstructed, α is a weighting parameter, ∂ is the total-variation (TV) (sparse-transform) along the temporal direction and defined as

$$\partial(m) = |\beta_t(m)| \tag{3.3}$$

where m is a voxel, and β_t is the finite difference in the temporal direction. The difference operator used for the total variation was a one-sided difference.

For successful compressed sensing application, sampling trajectories that induce incoherent, noise-like, artifacts should be used. This can be satisfied by using radial trajectories where undersampling is achieved in two dimensions. This makes radial sampling very robust with respect to undersampling, as the undersampling artifacts appear as slight streaking and increased pseudo-noise. In radial sampling, radial spokes passing through the k-space origin are acquired with uniform angular spacing. However, homogenous coverage and higher incoherence values were achieved by sampling with non-uniform golden angle angular spacing [23-25]. This reduces the symmetry of the point spread function (PSF) of radial sampling, allowing for better compressed sensing reconstruction. The repetitive acquisition of the center of the k-space is of special interest, leading to dense oversampling of the center of k-space suppressing motion artifacts.

3.2.4 Self-gating

For self-gated cardiac Cine MRI, the cardiac and respiratory cycle information is extracted from the MRI data itself. For the FLASH sequence, self-gating information can be retrieved from the echo that is produced by the slice-refocusing gradient, at the cost of increased TE [14]. In the radial acquisition scheme of the UTE sequence the center point in the k-space that is recorded each TR can be used for self-gating purposes. Cardiac triggering and respiratory gating is therefore derived directly from the radial readout with the shortest possible TE and TR.

3.2.5 Data analysis

To validate the multi-slice self-gated UTE reconstructions, cardiac functional parameters (end-systolic and end-diastolic LV cavity lumen volume, and ejection fraction) derived from the fully sampled and undersampled CS reconstructions were compared to those obtained from the FLASH acquisitions. Global heart parameters were calculated using a semi-automatic segmentation with the QMass MR software (version 7.5) by Medis (Medis Medical Imaging Systems B.V., Leiden, The Netherlands). One person performed all the segmentations. Contours were manually corrected for the papillary muscle area. Statistical analysis was performed using SPSS 20.0 (SPPS, Inc., Chicago, IL, USA). A t-test with post-hoc Bonferroni correction was performed to compare the EF for the different reconstructions between and within the healthy and infarct groups. The level of statistical significance was set at $p = 0.05$. A Bland-Altman analysis was performed for ESV, EDV, EF, and CO to test the level of agreement between cardiac parameters derived from fully sampled and undersampled reconstructions.

Additionally, 4 independent observers, who were blinded to the type of sequence and reconstruction, visually scored the diagnostic quality of the movies from the different protocols. The movies were presented to the observers in a random order. Criteria included signal to noise (SNR), contrast to noise (CNR) between myocardium and blood pool, presence of reconstruction artifacts (e.g. streaking due to radial sampling or ghosting due to undersampling), and presence of flow artifacts. Scoring in these categories was performed on a standard 4 point scale, with 1 = poor to 4 = excellent for SNR and CNR, and 1 = uninterpretable due artifacts to 4 = no artifacts for scoring artifacts. A Wilcoxon's signed ranked test was used for comparing the scores. The level of statistical significance was set at $p = 0.05$.

3.3 Results

The navigator information was obtained from the first sampled point at the start of the radial readout. Cardiac and respiratory cycles could be clearly distinguished in a trace of the navigator signal intensity, as shown in Fig. 1B for a representative example from one of the in-vivo measurements. Consequently, the acquired radial k-lines could be accurately assigned to the corresponding cardiac time frames and approximately 30% of the k-lines acquired during respiration were rejected. The average heart rate for all the rats included in the experiment was 348 ± 51 beats per min.
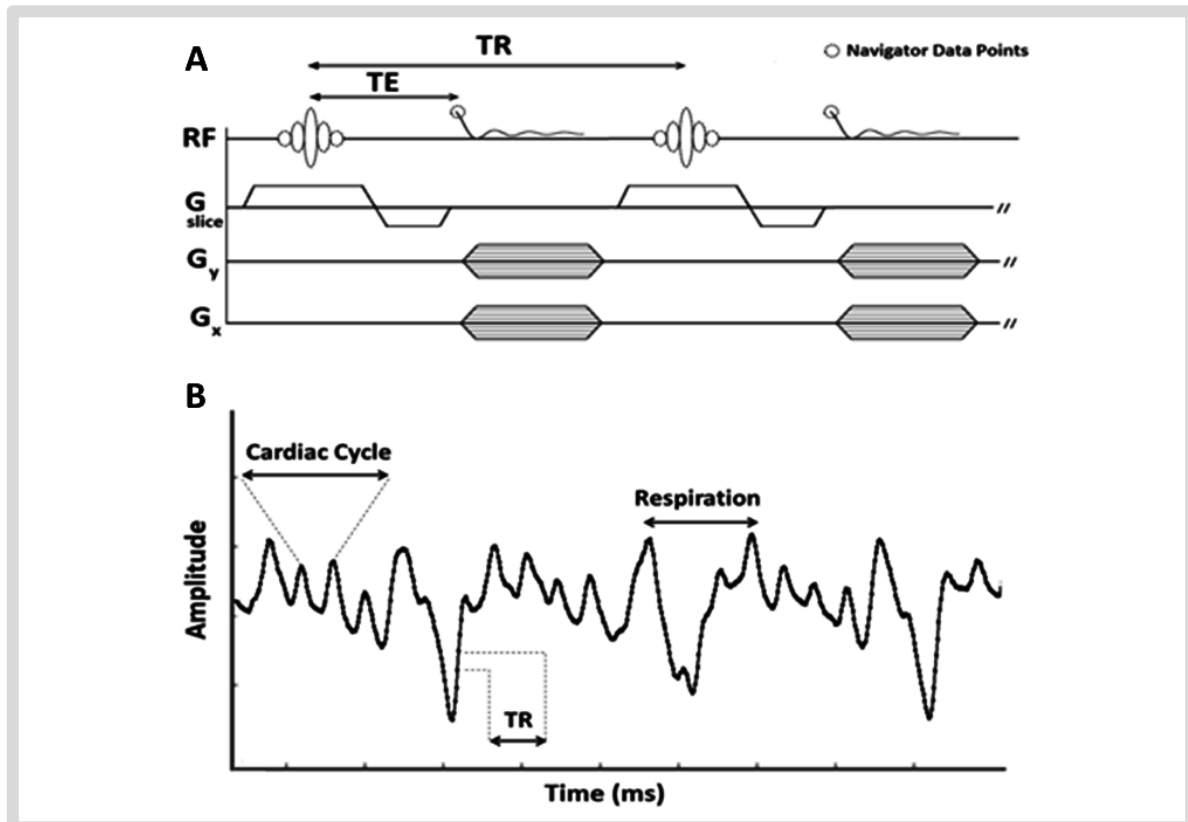
Figure 1. Schematic of the 2D self-gated UTE sequence. A) Readout is performed with short TE and directly after the slice refocusing gradient. A navigator signal for the recording of cardiac and respiratory motion is extracted from the first point (circle) of the readout. B) Representative example of the navigator signal amplitude as function of time. The rapid oscillation in the amplitude is due to cardiac motion, whereas the larger changes, lower frequency in amplitude are due to respiration. The solid line is a spline fit through the individual navigator samples (solid circles).

The top left panel in Fig. 2 shows a long-axis image of a rat with myocardial infarction at end-diastole with lines indicating the position of the 5 short-axis slices shown in the other panels. Long-axis and short-axis images were acquired with the fully sampled 3min47s self-gated 2D UTE acquisition. The 5 slices covered the heart from base to apex. Good contrast between blood and myocardium was achieved, facilitating accurate segmentation of the left ventricular (LV) wall and lumen. Movies were visually free from flow or other artifacts.

Figure 2. Long-axis and 5 short-axis slices at end-diastole of an infarcted rat heart obtained with the fully sampled 3min47s self-gated 2D UTE acquisition. The position of the 5 short-axis slices is indicated in the long-axis image.
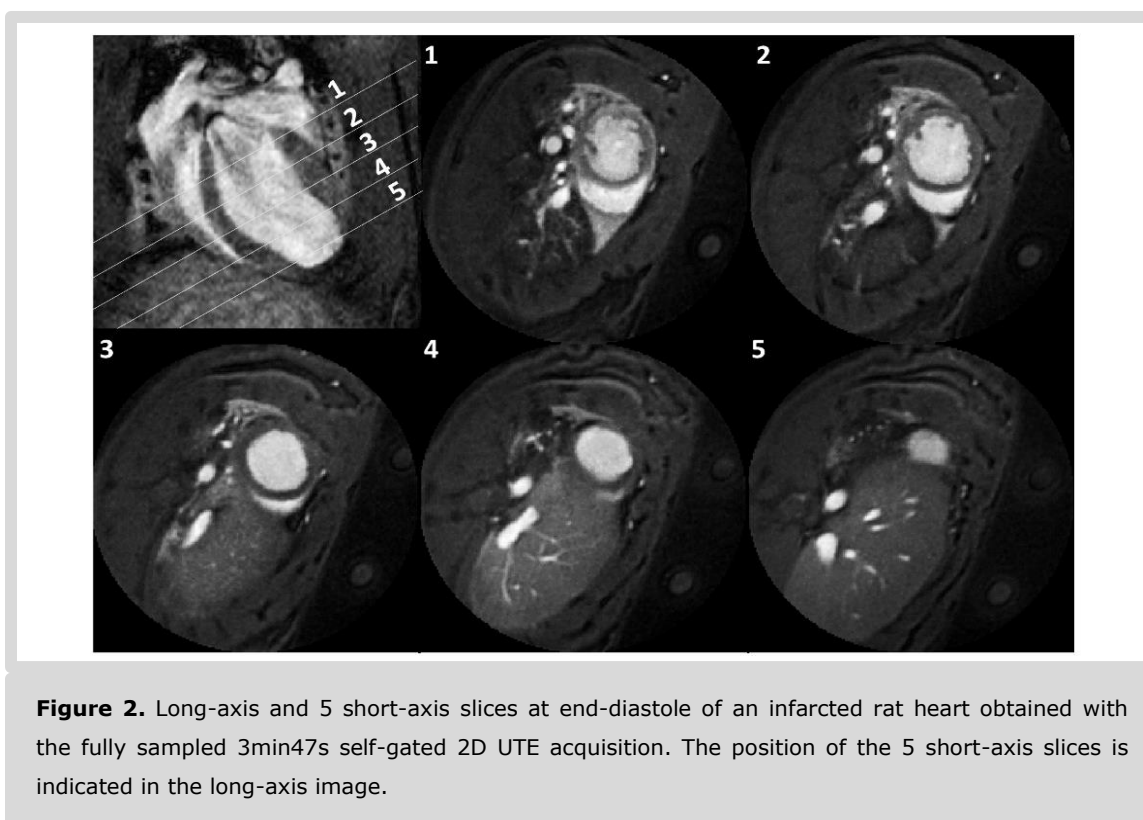
A comparison between the fully sampled UTE Cine acquisition and the standard self-gated FLASH is presented in Fig. 3 for several time frames in the cardiac cycle at a mid-ventricular slice of a healthy rat. FLASH acquisitions suffered from flow artifacts particularly during the filling phases in diastole. In contrast, uniform blood signal intensity was observed in UTE acquisitions with no visible flow artifacts in the left and right ventricle. Undersampling of the radial acquisition with golden-angle k-space filling leads to

relatively mild artifacts using a standard linear Fourier transform reconstruction, as shown in the top row of Fig. 4 for the 1min (2X undersampling), 30s (4X undersampling) and 15s (5X undersampling) at a mid-ventricular slice of a healthy rat at end-diastole. Undersamplng artifacts were incoherent and noise-like, which is a requirement facilitating CS reconstruction, clearly leading to improved image quality. Even for 5X undersampling in Fig. 4F the CS reconstruction nearly recovered the image quality of the 1min linear reconstruction shown in Fig. 4A. Movies with higher undersampling factor were judged visually unfit for quantitative analysis.

Figure 3. Comparison of fully sampled FLASH and UTE. Short-axis mid-ventricular end-systolic, mid-diastolic, and end-diastolic time frames from a Cine of a healthy rat heart using the fully sampled self-gated FLASH and UTE scans. In contrast to the FLASH, the UTE scans are free from blood flow artifacts in the left and right ventricle.
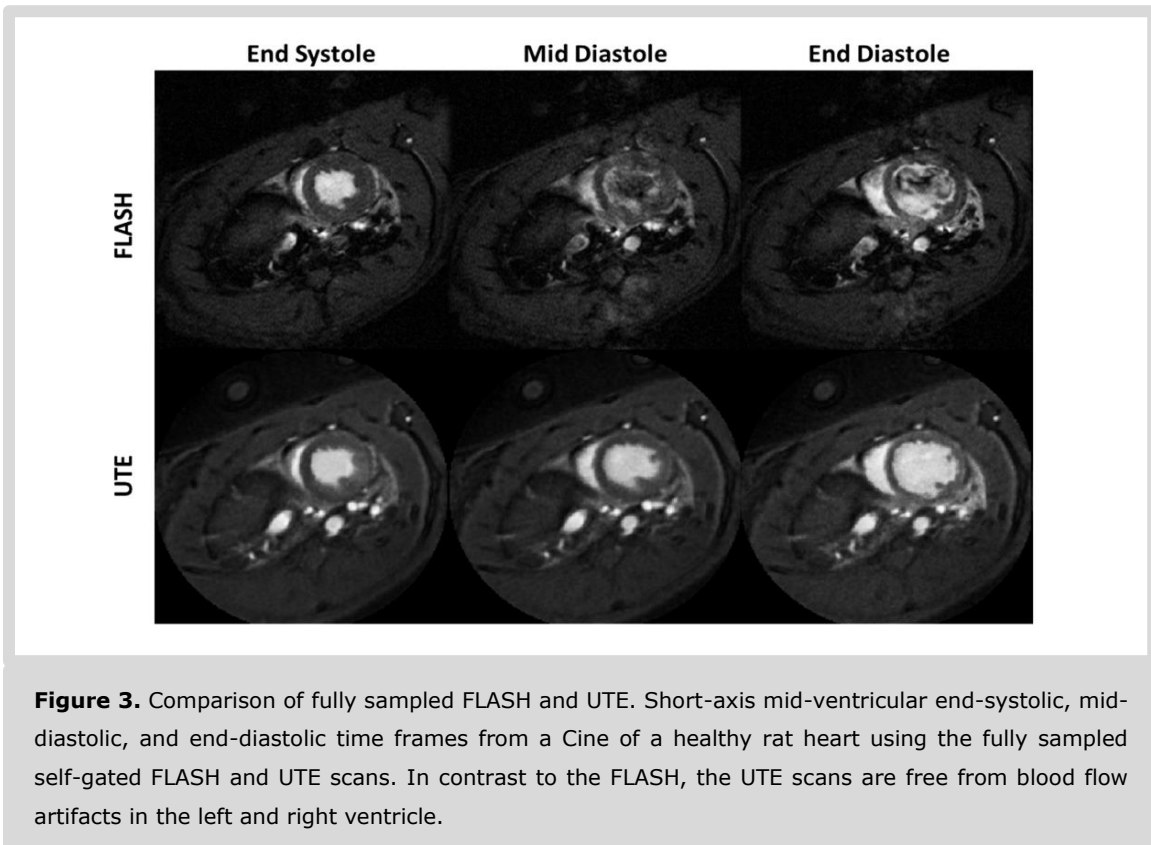
Frames at end-diastole and end-systole, as well as magnifications of the heart region for fully sampled and undersampled UTE acquisitions are shown in Fig. 5 A and B for a healthy rat and a rat with myocardial infarction, respectively. For all 4 healthy rats and the 4 rats with myocardial infarction, cardiac movies in all 5 slices were successfully reconstructed by CS up to 5X kt-space undersampling.

Four observers blinded to the type of scan and reconstruction method visually scored the quality of the cardiac movies using a standard 4-point scoring scale. The average scores in 4 categories, i.e. SNR, CNR between blood and myocardium, presence of reconstruction artifacts and presence of flow artifacts, are summarized in Table 2. As shown in the table, the quality of the fully sampled UTE movies was superior to the fully sampled FLASH movies. For the UTE protocols, there was a significant decrease in the average scoring of the SNR, CNR and reconstruction artifacts with increasing degree of undersampling. In contrast to the FLASH protocol, the UTE protocols were free of flow-artifact free images. For a quantitative analysis, in Fig. 6 a bar chart of the EF for the healthy and infarct rats comparing FLASH and UTE acquisitions is shown.

Figure 4. Difference between Linear and CS reconstructions of undersampled UTE scans. Shown is a mid-ventricular slice of a healthy rat heart at end-diastole. Image quality of linear reconstructions of the 2x (1min), 4X (30s), and 5X (15s) undersampled data was poor with noise-like and streaking artifacts. The CS reconstruction mitigated the undersampling artifacts resulting in greatly improved image quality.

As expected, the animals with myocardial infarction showed significantly lower ejection fractions than healthy ones in both FLASH and UTE images. However, within the standard

deviation of the admittedly limited (N=4) number of animals there were no statistical differences between FLASH, fully sampled, and accelerated UTE acquisitions within the infarct and healthy groups.

Table 2: Average scoring of the different protocols by 4 observers. Scoring in the categories SNR, CNR, presence of reconstruction artifacts, and presence of flow artifacts was performed on a standard 4-point scale, with 1 = poor to 4 = excellent for SNR and CNR, and 1 = uninterpretable due artifacts to 4 = no artifacts for scoring the presence of artifacts.

	FLASH fully sampled	**UTE fully sampled**	**UTE 2X**	**UTE 4X**	**UTE 5X**
SNR	3.13 ± 0.64	3.75 ± 0.44*	3.45 ± 0.52	2.87 ± 0.55#	2.66 ± 0.63#
CNR	3.52 ± 0.52	3.66 ± 058	3.56 ± 0.44	3.31 ± 0.54#	3.12 ± 0.66#
Reconstruction artifacts	3.33 ± 0.80	4.0*	3.64 ± 0.45*#	2.54 ± 0.50*#	2.12 ± 0.42*#
Flow artifacts	2.54 ± 0.46	4.0*	4.0*	4.0*	4.0*

All values are mean ± standard deviation. * Indicates significantly different from FLASH fully sampled. # Indicates significantly different from UTE fully sampled.
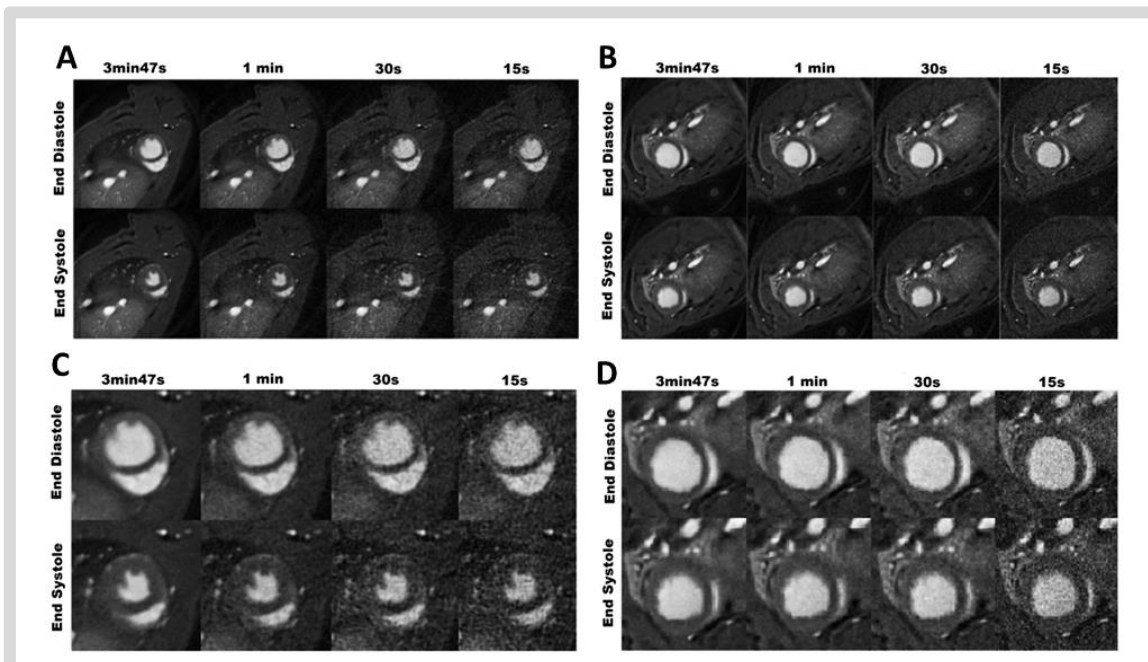
Figure 5. Short-axis frames at end-diastole and end-systole comparing the fully sampled UTE scan and the undersampled UTE scans with CS reconstruction for a A) healthy and B) Infarcted rat. C,D) Magnification of the region containing the heart.

Additionally, to evaluate the effect of CS reconstruction and degree of undersampling on derived heart functional parameters of standard and CS reconstructions in more detail, the end-systolic volume (ESV), end-diastolic volume (EDV), ejection fraction (EF) and cardiac output (CO) from the FLASH and UTE scans were compared. As an example, Fig. 7 shows the Bland-Altman plot for the functional parameters of a 4X undersampled UTE acquisition with CS reconstruction compared to the FLASH acquisition for the 8 rats included in the experiment. Differences in ESV, EDV, EF and CO only had a small bias. Table 3 summarizes the Bland-Altman analysis of the heart functional parameters for all the UTE acquisitions compared to the FLASH scans.

Figure 6. Comparisons of EF between the experimental groups and for the FLASH and UTE acquisitions.
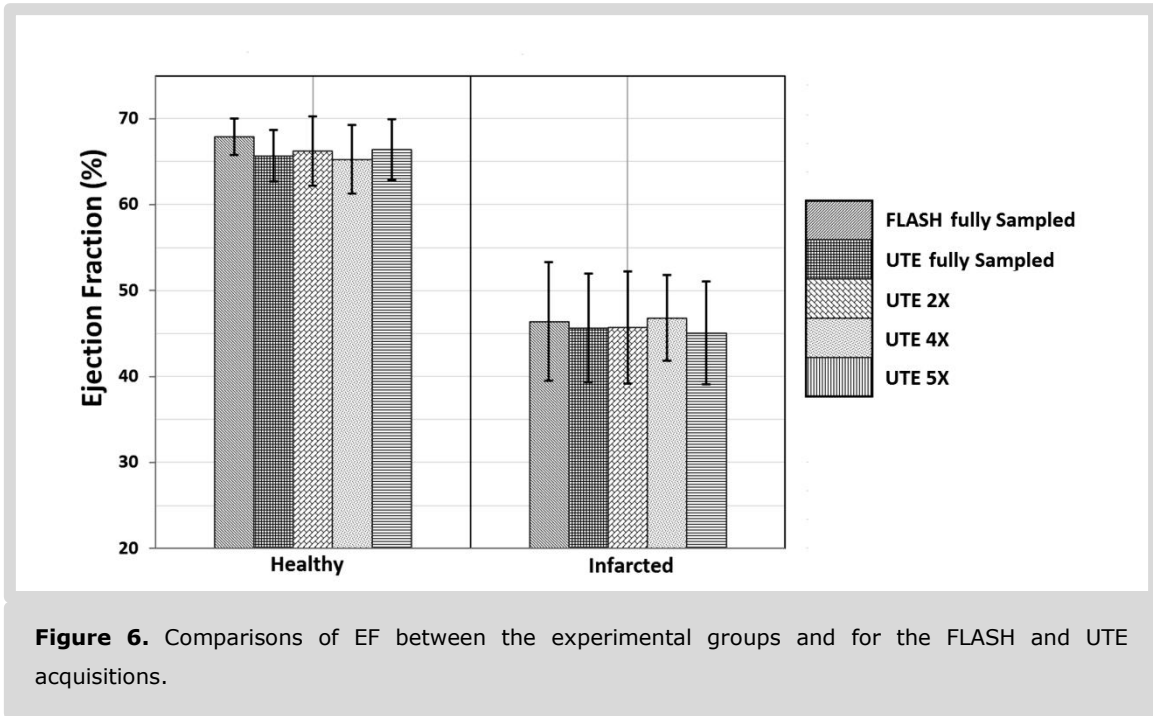
3.4   Discussion

Radial k-space encoding schemes are becoming popular and find successful applications in clinical and preclinical studies [26-28]. The repetitive and dense acquisition of the center of the k-space makes the sequence relatively robust to motion [29]. This allows for better performance in capturing dynamic information. Besides, radial undersampling results in relatively mild streaking artifacts, which can be effectively removed by novel compressed

sensing reconstruction methods making the technique suitable for high acceleration factors [23, 24]. The short TE that can be achieved in UTE sequences traditionally finds applications in bone, fibro-cartilage and lung imaging [30, 31]. Radial and spiral k-space filling schemes are employed for cardiovascular imaging in humans [27, 32-36] and animals [28, 37-40].
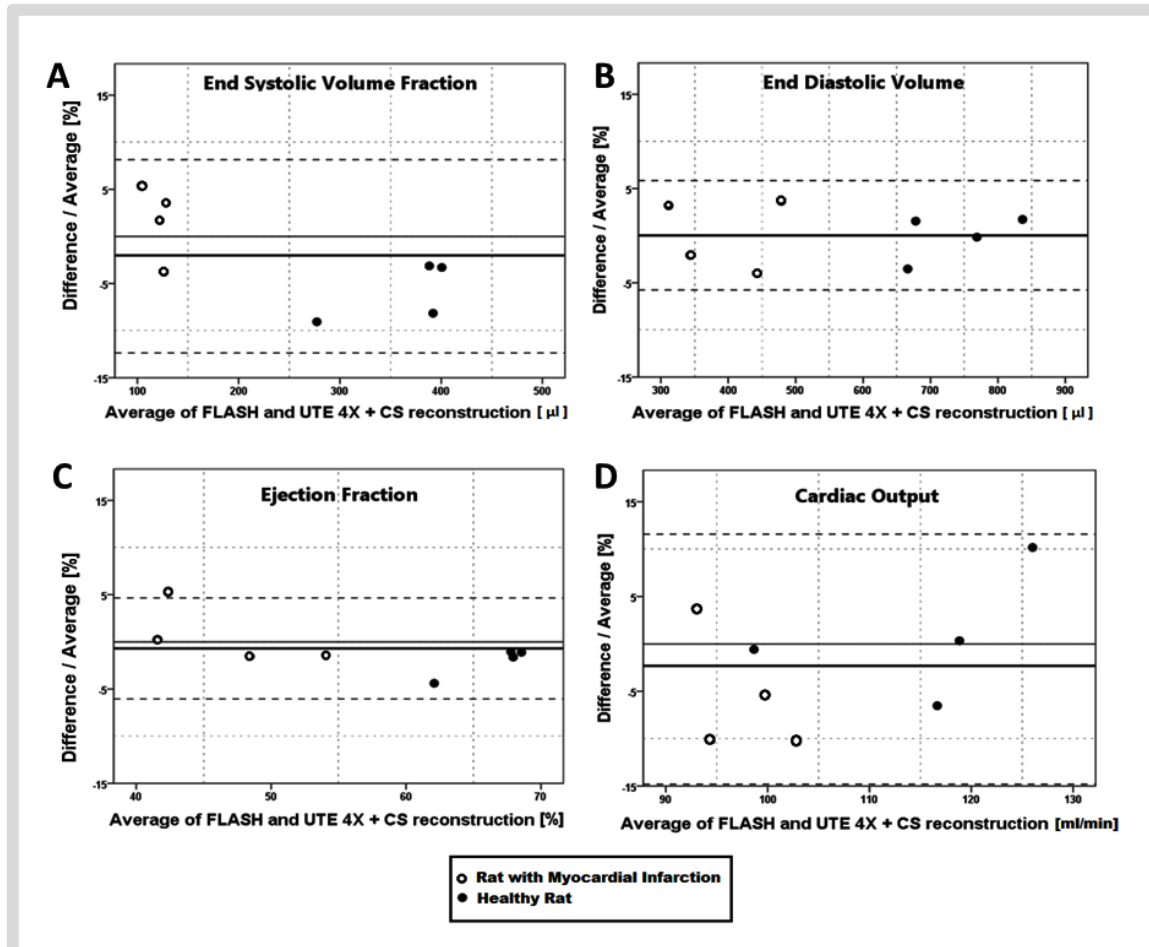
Figure 7. Bland-Altman analysis of the heart functional parameters, A) ESV, B) EDV, C) EF and D) CO, for 4X undersampled UTE in comparison to fully sampled FLASH. Solid and open points indicate data for healthy and infarcted rat hearts, respectively.

Recently, UTE MRI was employed to detect developing myocardial fibrosis after myocardium infarction, exploiting the short T2* of fibrous tissue [37, 38]. Moreover, a radial readout proved beneficial in phase-contrast velocity encoded imaging for high

velocity blood flow quantification in stenotic jets, present in arterial occlusions due to atherosclerosis, which cannot be recorded using the conventional phase contrast sequences with longer TE [41].

Table 3: Bland-Altman analysis of cardiac functional parameters. Comparisons of FLASH with UTE protocols.

	UTE fully sampled	UTE 2X	UTE 4X	UTE 5X
ESV	-0.2 ± 11.0	-2.1 ± 10.5	-2.1 ± 10.3	-4.1 ± 9.5
EDV	-0.5 ± 4.3	-0.1 ± 5.2	0.04 ± 5.80	-0.0 ± 5.6
EF	-1.6 ± 2.8	-1.0 ± 2.6	-0.7 ± 5.4	-1.2 ± 2.4
CO	-3.7 ± 7.1	-3.1 ± 6.0	-2.3 ± 13.9	-4.2 ± 8.3

All values are mean ± 1.96 standard deviation in percentages. ESV = end-systolic volume; EDV = end-diastolic volume; EF = ejection fraction; CO = cardiac output.

In this study, an accelerated 2D multislice self-gated UTE sequence was implemented. Ultimately, volumetric imaging with 3D radial readout would be even more favorable. In 3D, the undersampling artifacts display more incoherence, which allows for a higher degree of acquisition undersampling [17, 23]. Moreover, in our sequence TE could be further reduced from 290 μs for 2D to about 20-50 μs for 3D due to the absence of a slice selection refocusing gradient.

Presently, for the 15-frame Cine reconstructions 5X undersampling was the upper limit. With this technology the measurement of a single slice takes only 15s and full heart coverage was obtained within 1min30s, which is much faster than traditional murine Cine imaging [14, 15]. For higher undersampling factors a number of frames within the cardiac cycle displayed artifacts that made them unsuitable for accurate segmentation and further analysis. The number of frames with artifacts increased with acceleration factor.

Qualitative visual scoring of movie quality by four blinded observers revealed that quality of the fully sampled UTE movies was superior to the fully sampled FLASH movies, primarily due to the absence of flow artifacts in the UTE protocols. For the UTE protocol, SNR and CNR decreased with increasing degree of undersampling and the number of

reconstruction artifacts increased. Nevertheless, a quantitative comparison revealed no statistical difference between the mean EF derived from movies obtained by the different protocols (Fig. 6) and Bland-Altman analysis (Fig. 7) showed only minor differences for the cardiac functional parameters ESV, EDV, EF, and CO of FLASH and UTE protocols. Taken together, this shows that LV functional parameters could be derived accurately with the UTE protocol and CS reconstruction up to 5X undersampling.

Since we are using a self-gated sequence with no ECG triggering, filling of kt-space cannot be fully predetermined as it relies on the asynchronous timing between heartbeat, respiration and TR. The effective number of averages for the acquired k-lines and the percentage of k-space filling therefore vary over the acquisitions (Table 1) as well as over the cardiac time frames. The acquisition of a fully sampled dataset therefore takes relatively long as we have to ensure that at least approximately 95% of all k-lines are filled [15, 42]. The use of self-gating has the distinct advantage that the number of time frames in the cardiac cycle is not predetermined but can be chosen after scan completion. In this work, the standard Cine reconstructions were performed with 15 cardiac time frames. However, we can also achieve a higher number of cardiac frames with the same effective undersampling factor at the expensive of a longer acquisition time. High frame rate Cine is useful to assess diastolic function, which requires a high temporal resolution particularly in the filling phase of the heart [15, 42]. As an example, in Fig. 8 several frames from a 60-frames Cine are shown, reconstructed from a 1 min acquisition with 5X undersampling.

In this paper, we implemented a self-gated UTE sequence with golden-angle radial acquisition and CS reconstruction for studying murine heart. We believe that self-gating and accelerated UTE scanning could also prove beneficial for human application to decrease scanning time and reduce image artifacts, particularly at high magnetic field strengths.
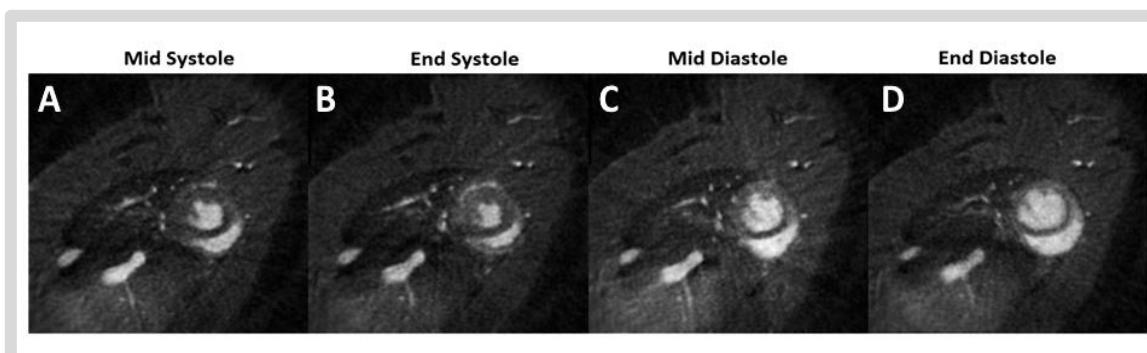
Figure 8. High frame rate CINE UTE reconstruction. Short-axis slices of a healthy rat heart at various time points in the cardiac cycle, A) Mid Systole, B) End Systole, C) Mid Diastole and D) End Diastole, taken from a 60-frames CINE. The data was recorded using the self-gated UTE with a total acquisition time of 1min and 5X undersampling.

In summary, in this work we presented a multi-slice UTE MRI protocol for whole heart Cine imaging of the rat heart. The technique exploits the self-gated acquisition scheme to produce an undersampled, random kt-space. Compressed sensing reconstructions were successful in mitigating undersampling artifacts up to 5X undersampling. Whole heart coverage 15-frame Cine was achieved in 1min30s. Cardiac functional parameters of healthy and infarcted rat hearts derived from fully and undersampled acquisitions were statistically the same as those derived from standard Cine FLASH.

References

1. McVeigh, E., *Regional myocardial function.* Cardiol Clin, 1998. **16**(2): p. 189-206.
2. Watzinger, N., et al., *Myocardial viability: magnetic resonance assessment of functional reserve and tissue characterization.* J Cardiovasc Magn Reson, 2001. **3**(3): p. 195-208.
3. Kim, R.J., et al., *The use of contrast-enhanced magnetic resonance imaging to identify reversible myocardial dysfunction.* New England Journal of Medicine, 2000. **343**(20): p. 1445-1453.
4. Geelen, T., et al., *Contrast-enhanced MRI of murine myocardial infarction - part I.* NMR Biomed, 2012. **25**(8): p. 953-68.
5. Kober, F., et al., *Cardiovascular magnetic resonance of myocardial structure, function, and perfusion in mouse and rat models.* Current Cardiovascular Imaging Reports, 2012. **5**(2): p. 109-115.
6. Shin, T., et al., *Three dimensional first-pass myocardial perfusion imaging at 3T: feasibility study.* J Cardiovasc Magn Reson, 2008. **10**: p. 57.
7. Peters, D.C., et al., *Undersampled projection reconstruction applied to MR angiography.* Magn Reson Med, 2000. **43**(1): p. 91-101.
8. Thedens, D.R., et al., *Fast magnetic resonance coronary angiography with a three-dimensional stack of spirals trajectory.* Magn Reson Med, 1999. **41**(6): p. 1170-9.
9. Frahm, J., A. Haase, and D. Matthaei, *Rapid Nmr Imaging of Dynamic Processes Using the Flash Technique.* Magnetic Resonance in Medicine, 1986. **3**(2): p. 321-327.
10. Robson, M.D., et al., *Magnetic resonance: An introduction to ultrashort TE (UTE) imaging.* Journal of Computer Assisted Tomography, 2003. **27**(6): p. 825-846.
11. O'Brien, K.R., et al., *Aortic valve stenotic area calculation from phase contrast cardiovascular magnetic resonance: the importance of short echo time.* Journal of Cardiovascular Magnetic Resonance, 2009. **11**.
12. Hoerr, V., et al., *Cardiac-respiratory self-gated cine ultra-short echo time (UTE) cardiovascular magnetic resonance for assessment of functional cardiac parameters at high magnetic fields.* Journal of Cardiovascular Magnetic Resonance, 2013. **15**.
13. Heijman, E., et al., *Comparison between prospective and retrospective triggering for mouse cardiac MRI.* Nmr in Biomedicine, 2007. **20**(4): p. 439-447.
14. Nauerth, A., E. Heijman, and C. Diekmann. *Slice refocusing signal for retrospective reconstruction of CINE cardiac MR images.* in *Proc. Intl Soc. Magn. Reson. Med*. 2006.
15. Coolen, B.F., et al., *High frame rate retrospectively triggered Cine MRI for assessment of murine diastolic function.* Magnetic Resonance in Medicine, 2013. **69**(3): p. 648-656.
16. Larson, A.C., et al., *Self-gated cardiac cine MRI.* Magnetic Resonance in Medicine, 2004. **51**(1): p. 93-102.
17. Lustig, M., D. Donoho, and J.M. Pauly, *Sparse MRI: The application of compressed sensing for rapid MR imaging.* Magnetic Resonance in Medicine, 2007. **58**(6): p. 1182-1195.
18. Fessler, J.A. and B.P. Sutton, *Nonuniform fast Fourier transforms using min-max interpolation.* Ieee Transactions on Signal Processing, 2003. **51**(2): p. 560-574.
19. Wech, T., et al., *Accelerating Cine-MR Imaging in Mouse Hearts Using Compressed Sensing.* Journal of Magnetic Resonance Imaging, 2011. **34**(5): p. 1072-1079.
20. Otazo, R., et al., *Combination of Compressed Sensing and Parallel Imaging for Highly Accelerated First-Pass Cardiac Perfusion MRI.* Magnetic Resonance in Medicine, 2010. **64**(3): p. 767-776.
21. Gamper, U., P. Boesiger, and S. Kozerke, *Compressed sensing in dynamic MRI.* Magnetic Resonance in Medicine, 2008. **59**(2): p. 365-373.
22. Buonincontri, G., et al., *Functional assessment of the mouse heart by MRI with a 1-min acquisition.* Nmr in Biomedicine, 2014. **27**(6): p. 733-737.
23. Doneva, M., et al. *Highly undersampled 3D golden ratio radial imaging with iterative reconstruction*. in *Intl Soc Mag Reson Med*. 2008.
24. Feng, L., et al., *Golden-Angle Radial Sparse Parallel MRI: Combination of Compressed Sensing, Parallel Imaging, and Golden-Angle Radial Sampling for Fast and Flexible Dynamic Volumetric MRI.* Magnetic Resonance in Medicine, 2014. **72**(3): p. 707-717.
25. Winkelmann, S., et al., *An optimal radial profile order based on the golden ratio for time-resolved MRI.* Ieee Transactions on Medical Imaging, 2007. **26**(1): p. 68-76.
26. Thompson, R.B. and E.R. McVeigh, *Flow-gated phase-contrast MRI using radial acquisitions.* Magnetic Resonance in Medicine, 2004. **52**(3): p. 598-604.

27. Bauer, R.W., et al., *True real-time cardiac MRI in free breathing without ECG synchronization using a novel sequence with radial k-space sampling and balanced SSFP contrast mode.* International Journal of Cardiovascular Imaging, 2013. **29**(5): p. 1059-1067.

28. Hiba, B., et al., *Cardiac and respiratory self-gated cine MRI in the mouse: Comparison between radial and rectilinear techniques at 7T.* Magnetic Resonance in Medicine, 2007. **58**(4): p. 745-753.

29. Glover, G.H. and J.M. Pauly, *Projection Reconstruction Techniques for Reduction of Motion Effects in Mri.* Magnetic Resonance in Medicine, 1992. **28**(2): p. 275-289.

30. Bergin, C.J., G.H. Glover, and J.M. Pauly, *Lung Parenchyma - Magnetic-Susceptibility in Mr Imaging.* Radiology, 1991. **180**(3): p. 845-848.

31. Du, J.A., et al., *Qualitative and quantitative ultrashort echo time (UTE) imaging of cortical bone.* Journal of Magnetic Resonance, 2010. **207**(2): p. 304-311.

32. Kramer, M., et al., *Retrospective Reconstruction of Cardiac Cine Images From Golden-Ratio Radial MRI Using One-Dimensional Navigators.* Journal of Magnetic Resonance Imaging, 2014. **40**(2): p. 413-422.

33. Jung, H., et al., *Radial k-t FOCUSS for High-Resolution Cardiac Cine MRI.* Magnetic Resonance in Medicine, 2010. **63**(1): p. 68-78.

34. Bauer R., et al., *True Real-Time Cardiac MRI with Radial K-Space Sampling in Free Breathing without ECG-synchronization—Improved Image Quality with Iterative Image Reconstruction*. Radiological Society of North America 2012 Scientific Assembly and Annual Meeting; 2012 Chicago IL

35. Seiberlich, N., et al., *Improved Temporal Resolution in Cardiac Imaging Using Through-Time Spiral GRAPPA.* Magnetic Resonance in Medicine, 2011. **66**(6): p. 1682-1688.

36. Usman, M., et al., *Motion corrected compressed sensing for free-breathing dynamic cardiac MRI.* Magn Reson Med, 2013. **70**(2): p. 504-16.

37. de Jong, S., et al., *Direct detection of myocardial fibrosis by MRI.* J Mol Cell Cardiol, 2011. **51**(6): p. 974-9.

38. van Nierop, B.J., et al., *In vivo ultra short TE (UTE) MRI of mouse myocardial infarction.*

39. Hiba, B., et al., *Cardiac and respiratory double self-gated cine MRI in the mouse at 7 T.* Magnetic Resonance in Medicine, 2006. **55**(3): p. 506-513.

40. Voiron, J. and L. Lamalle. *Spiral MRI on rat brain and rat heart at 7 Tesla*. in *Proc. Intl. Soc. Mag. Reson. Med*. 2006.

41. O'Brien, K.R., et al., *Phase contrast ultrashort TE: A more reliable technique for measurement of high-velocity turbulent stenotic jets.* Magn Reson Med, 2009. **62**(3): p. 626-36.

42. Motaal, A.G., et al., *Accelerated high-frame-rate mouse heart cine-MRI using compressed sensing reconstruction.* Nmr in Biomedicine, 2013. **26**(4): p. 451-457.

Towards 4D UTE Flow MRI

As you go, you will make mistakes of your own

But son, that's alright, you live and you learn ...

Related Articles:

➢ Abdallah G. Motaal, Verena Hoerr, Huiming Dong, Luc Florack, Klaas Nicolay, Gustav J. Strijkers. Accelerated 4D Phase Contrast UTE MRI. Proceedings of the International Society for Magnetic Resonance in Medicine (ISMRM), 2015, Canada.

Abstract

MRI of the mouse heart is usually performed with a gradient echo based sequence. Blood flow related artifacts are common since the echo time (TE) of a traditional gradient echo sequence in the order of milliseconds is not short enough to prevent dephasing of signal during the rapid filling and ejection phases of the heart. A shorter TE for mouse heart functional Cine and 4D flow imaging is therefore desired and this can be achieved by the use of an ultra-short echo time (UTE) MRI sequence with TEs in the range of 0.01 to 0.5 ms. Here, we introduce a preliminary study towards the development of a quantitative 4D UTE flow imaging sequence. We aimed for a 3D time resolved UTE Flow protocol for the whole mouse heart with self-gating and CS accelerated reconstruction. Phantom results showed good results in terms of flow velocity estimation with echo time (TE) of 0.68 ms in comparison to the standard FLASH based 3D Flow MR sequence. Preliminary in vivo experiments have been carried, where the objective was not fully reached yet and is still work in progress. When successful in vivo, full anatomical and functional maps for the whole heart could be acquired in a single scan session, which will assist in better and comprehensive assessment of the cardiovascular system.

4.1   Introduction

Cardiovascular diseases are major causes of death in the world. Magnetic resonance imaging (MRI) is an established technique to assess cardiac morphology and function in a clinical as well as preclinical setting. The mouse is a commonly used animal model to study cardiovascular diseases. Cardiac MRI of the mouse is a well-established technique, although MRI of the mouse heart is challenging due to its small size and high heart rate. MRI of the murine heart is commonly performed using gradient echo type sequences. Despite the fact that these sequences perform well to measure cardiac function and anatomy, blood flow related artifacts are common since the echo time (TE) of a traditional gradient echo sequence in the order of milliseconds is not short enough to prevent dephasing of signal during the rapid filling and ejection phases of the heart. Such artifacts can be avoided by the use of an Ultra Short Echo Time (UTE) sequence, with a TE in the range of 0.01 to 0.5 ms [1-6].

Apart from improved image quality by prevention of blood flow artifacts, UTE heart imaging might be advantageous for other reasons. First of all, the use of a UTE sequence allows the measurement of tissue components with short T2 relaxation time, which go undetected by the gradient echo sequence. For example, UTE sequences are extensively used for imaging the musculoskeletal system, particularly bone, ligaments and cartilage [4]. UTE sequences have found application in the cardiovascular system to image calcified plaque [5] and for the detection of fibrosis [6].

Phase contrast (PC) MRI is widely applied for blood flow mapping in clinical studies as well as in preclinical applications [7-10]. The bipolar gradients used in the PC sequences increase the echo time. However, by combining short TE sequences with PC method, the suppression of flow artifacts by the relatively short TE facilitates improved assessment of cardiovascular blood flow. In 4D MRI flow measurements, a time-resolved PC technique is combined with 3D volume acquisition, which enables a comprehensive assessment of the

cardiovascular system [11-13]. Most of the 4D PC MRI sequences are based on multi-slice acquisitions rather than volume excitation [14-15], which is still very challenging and suffers from long scan times [12].

In this chapter, we introduce a protocol for 4D PC UTE imaging in the mouse. It combines a self-gated 3D radial sequence with accelerated imaging using compressed sensing (CS) reconstruction. The aim of this work is to achieve time resolved 3D Flow Cine imaging of the mouse heart with a very short TE (0.68 ms). As a starting point, 3D PC blood flow measurements were conducted in phantoms, where the flow sequence was validated and compared to a standard 3D PC FLASH sequence. The here presented work is still in progress and image quality needs to be improved and more validations need to be performed prior to robust implementation for in vivo applications.

4.2   Materials and Methods

4.2.1   Measurement Setup

For sequence validation, a customized flow phantom was used. The phantom consisted of a cylindrical acrylic glass body filled with water with four small tubes placed inside and connected to a peristaltic water pump (Medorex e.K., Horten-Hardenberg, Germany) as shown in Fig. 1. The pumping rate was ranging between v=0-400 ml/min. The water pump was calibrated and it was confirmed that the pump provided the desired water flow rates.

The local animal care committee of the local government in Germany (North Rhine-Westphalia State Agency for Nature, Environment and consumer protection) reviewed and approved all experimental procedures.

For the in vivo experiments on mice, the animals were anesthetized using inhalation anesthesia (2-3% Isoflurane in oxygen (0.8 l/min) after intubation). Animals were placed on a heating pad and their temperature was continuously monitored by a rectal probe

and maintained between 36 and 37.5 ^{o}C. Mice were sedated by inhalation of 1.5 – 2.5% isoflurane in 0.7/0.3 air/O_2. After induction of anesthesia, the respiration of the mice was monitored continuously (SA instruments, Stony Brook, USA).

Figure 1. A) The customized flow phantom with B) an axial mid-slice proton density image from the reconstructed 3D volume, where the red arrow points toward the acrylic class container, white and black arrows point towards tubes where water flows in the through plane direction and in the opposite direction, respectively.
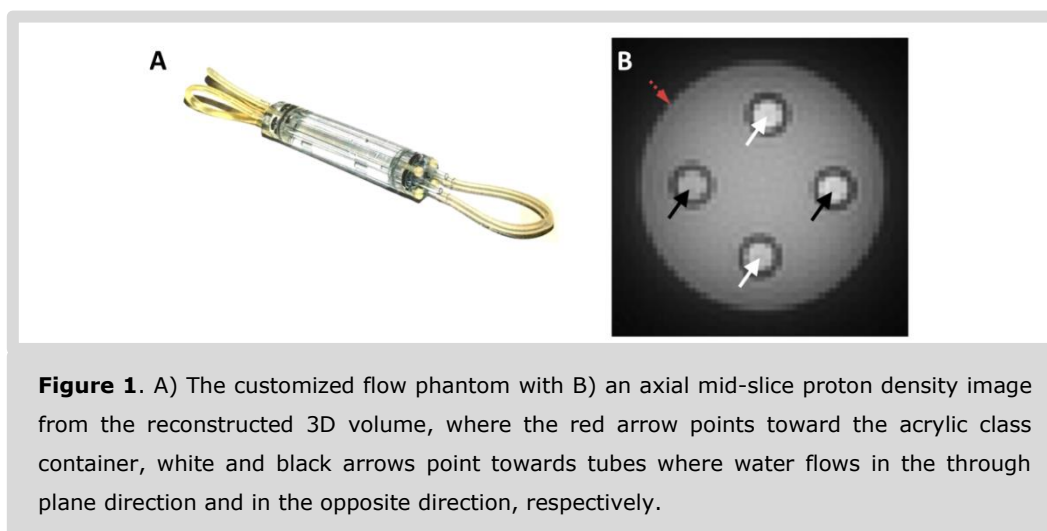
MRI measurements were performed with a 9.4 T small animal MRI system with a horizontal bore with a diameter of 20 cm (Bruker BioSpin GmbH, Ettlingen, Germany). A 35-mm-diameter mouse body quadrature volume coil (Rapid Biomedical, Germany) was used for signal transmission and reception. The scanner was equipped with a 1 T/m gradient insert (BGA-6S, Bruker BioSpin GmbH, Ettlingen, Germany). The MRI scanner was operated using the Bruker Paravision 6.0 acquisition software.

4.2.2 MRI protocol

The pulse sequence is schematically shown in Fig. 2. For validating the phase contrast measurements, the customized flow phantom was scanned with the lowest achievable TE of 0.68 ms as the length of bipolar gradients was 0.6 ms. Sequence parameters were: Block shaped RF pulse of 2 μs; flip angle = 5°; TR = 4 ms; number of spokes (NS) = 36424; field of view = 3 x 3 x 3 cm^3; isotropic acquisition matrix = 108; number of repetitions (NR) = 1; velocity encoding experiments to obtain 3D flow information (NV) = 4. The resulting total acquisition time was NR x NS x NV x TR = 9min42s.

Under-sampled data was generated by subsampling the fully sampled dataset retrospectively with different undersampling factors (2, 4, 6, 8, 9 and 10). Subsequently, the data has been reconstructed using compressed sensing algorithm as explained in section 4.2.4.

As a reference, a 3D FLASH based PC MR sequence with a four-point Hadamard encoding was used [16, 17]. Sequence parameters of the 3D FLASH were: TE/TR = 2.2/6.9 ms; FA = 15°; FOV = 3 × 3 × 3 cm^3; NA = 2; acquisition matrix (NF x NP x NS) = 108 × 108 × 108. The resulting total acquisition time was 10min42s. The 3D UTE flow sequence was calibrated and compared with the FLASH-based phase contrast measurement reference sequence.

In vivo MRI measurements were performed and sequence parameters were: Block shaped RF pulse of 2 μs; flip angle = 5°; TR = 5 ms; TE = 0.68 ms; number of spokes (NS) = 28733; field of view = 2.5 x 2.5 x 2.5 cm^3; isotropic acquisition matrix = 96; number of repetitions (NR) = 8. The resulting total acquisition time was NR x NS x TR x NV = 1h16min37s. Cine movies with 8 frames were reconstructed retrospectively by compressed sensing reconstruction.
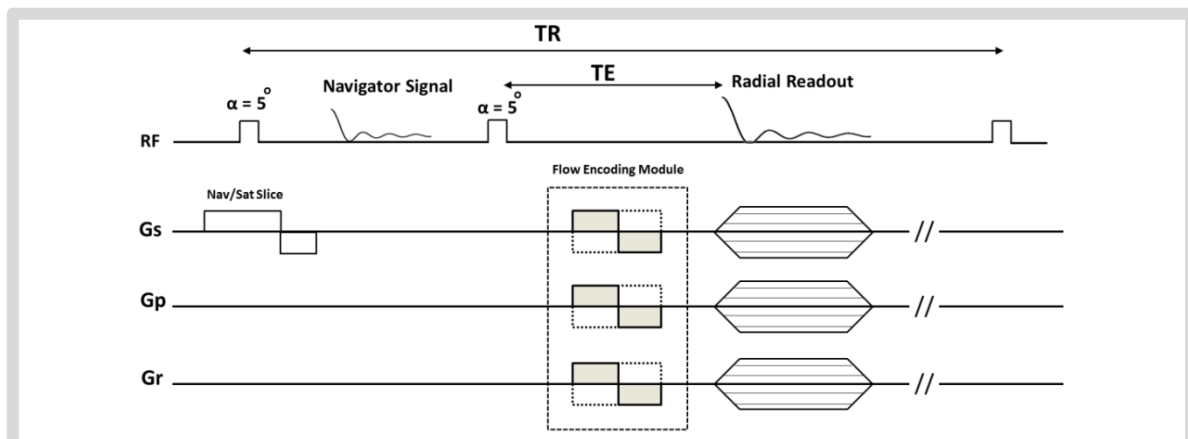
Figure 2. Schematic of the 3D Cine UTE sequence. For 4D PC UTE the flow-encoding module can be switched on. A navigator signal readout in a single slice is acquired every TR, preceding volume excitation. Cardiac and respiratory motion is extracted from the signal modulation of the navigator. Bi-polar gradients are added for PC measurements, where the dotted lines indicate the switching of the bipolar gradients to the opposite polarity with every flow encoding experiment.

4.2.3   Cardiac and Respiratory Gating

For retrospective reconstruction, a navigator slice was placed at the base of the heart, where the navigator signal could be extracted. The navigator signal intensity is modulated by the cardiac and respiratory movement and therefore can be used to assign the acquired k-spokes to the corresponding cardiac time points and reject data during respiratory motion. In a 2D radial acquisition scheme, the center point in the k-space that is recorded each TR can be used for self-gating purposes as was shown in chapter 3. However, in the 3D sequence this was not sensitive enough to extract the cardiac and respiratory movements. This is probably due to the fact that the total signal in the 3D imaging volume does not vary much with cardiac and respiratory motion. Another advantage of using a separate navigator slice is that a higher flip angle might be used to saturate inflowing blood leading to improved contrast between blood and myocardium. The navigator echo analyses were done off-line with homebuilt software in Matlab 8.1 using a local maximum detection algorithm to determine the start of the cardiac cycle. K-spokes acquired during respiration (~30% of the data) were discarded.

4.2.4   CS reconstruction

As demonstrated in the previous chapters, CS reconstruction can be used for accurate reconstruction of highly undersampled data under the conditions that data is sparse and undersampling is performed in an incoherent way. Because acquisitions were performed asynchronously with cardiac motion, the resulting 4D kt-space is filled at significant sub-Nyquist rates incoherently in space and time, which facilitates CS reconstruction.

A non-linear CS algorithm was used for reconstruction. Mathematically, the following unconstrained optimization ℓ_1-minimization problem was solved:

$$min_m\{ \, ||R^{-1}F_s m - y||_2^{\,2} + \alpha \, ||\partial(m)||_1 \qquad\qquad (4.1)$$

where m is the 4D kt-space data to be reconstructed, ∂ is the sparsifying transformation, where spatio-temporal finite difference domain was selected as a sparsifying domain, m is the reconstructed data, y is the measured undersampled kt-space, and Fs is the Fourier transformation, R is a gridding operator that interpolates the Fourier data to radial spokes to ensure data consistency with acquired data. For Non-uniform Fourier transformation (NUFFT), the online available Fessler toolbox was used [18].

4.3   Results

A linear phase shift through the slices in the phase maps was noticed. The cause for such linear phase is the eddy current induced by the pulsed or the bipolar gradients that lead to miscalculation of flow velocity [19]. A simple correction algorithm was used, where the background linear phase shift that is estimated from a no-flow (static region) through all the slices is subtracted from the estimated phase maps, as shown in Fig. 3.

Fig. 4A shows an axial slice of the flow phantom used for phase contrast experiments. The corresponding flow map, providing calculated flow velocities, is shown in Fig. 4B. The map shows hyper- and hypo-intense regions representing the in-/out water flow in the tubes. In Fig. 4C, the average flow velocities in two regions of interest (flow-in and flow-out tubes) are calculated in all the slices. It shows that the estimated flow in all the slices is nearly identical. For sequence calibration, the experiments were carried out with different flow rates (Q ranges from 30 to 300 ml/min with step of 30 ml/min) using the proposed and the standard FLASH based 3D PC sequence that gives accurate velocity estimation. The estimated velocity using the 3D PC UTE sequence increased linearly with the increase in the input flow as shown in Fig. 5A. The relation between the velocity estimated from the 3D UTE Flow and 3D PC FLASH experiment is shown in Fig. 5B. Although there is a linear relationship, there is an underestimation compared to the gold standard 3D PC FLASH sequence. Therefore, the flow velocity estimated from the 3D UTE Flow

experiments were corrected using the calibration coefficient estimated from the linear fitted line in Fig. 5B.
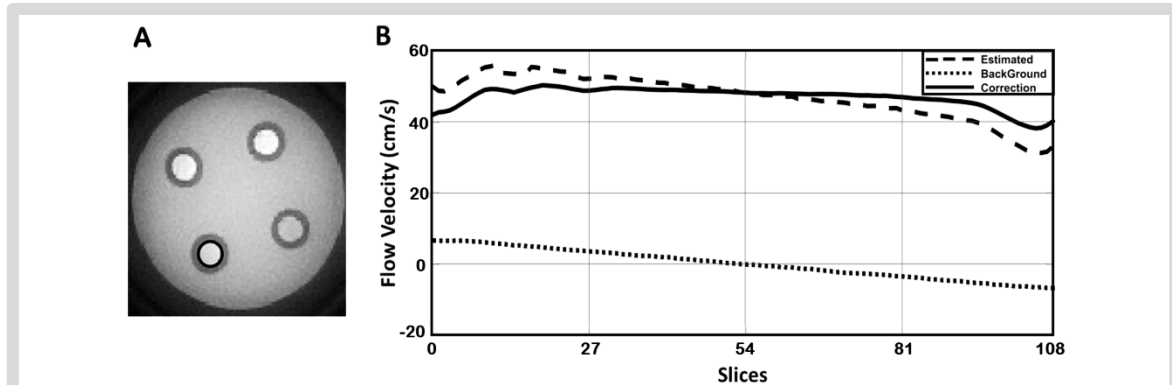
Figure 3. A) Axial mid-slice proton density image from a reconstructed 3D volume, and the B) estimated flow velocity as a function of the slice location drawn in a dashed line and is estimated from a region of interest shown in A with a black circle. The corrected flow estimation curve is shown in solid line that has been calculated from the difference of the estimated flow curve and the background linear phase that is shown in dotted lines.
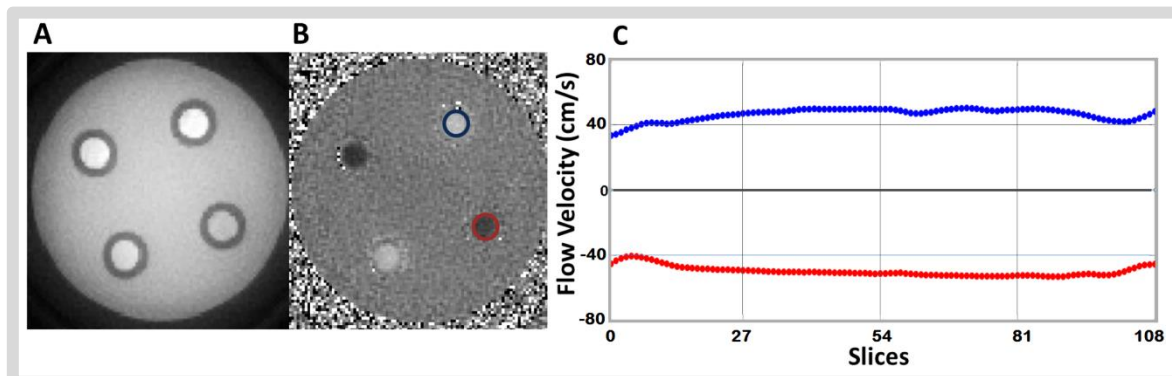
Figure 4. A) Axial mid-slice proton density image from a reconstructed 3D volume, and the corresponding B) phase map of the slice showing the two opposite through plane flow of water shown in hypo-/hyper intensities respectively. C) The estimated velocities as a function of the slice location estimated from different region of interest as shown in A with blue and red circles.

Fig. 6 shows an axial slice reconstructed from the fully sampled and the undersampled datasets using CS reconstruction with different acceleration factors. The image quality of the standard acquisition was nearly recovered for up to 6X acceleration. Image quality of the >=8X-accelerated reconstructions were visually judged insufficient for evaluation.
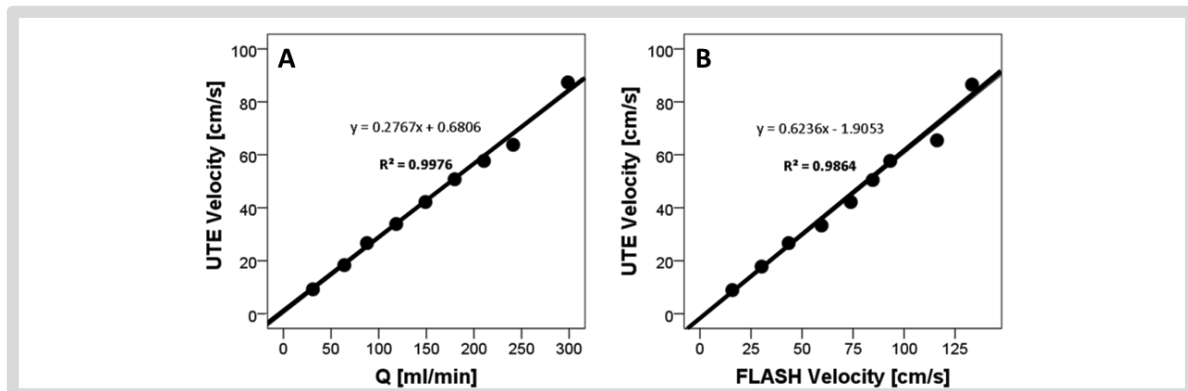
Figure 5. A) The relation between the input flow rate and estimated velocity using the proposed sequence, where it shows they are linearly correlated. B) The relation between the flow velocity estimated using the proposed sequence and the 3D PC FLASH sequence, which shows that the estimated velocity using the proposed sequence is underestimated compared to 3D PC FLASH sequence.
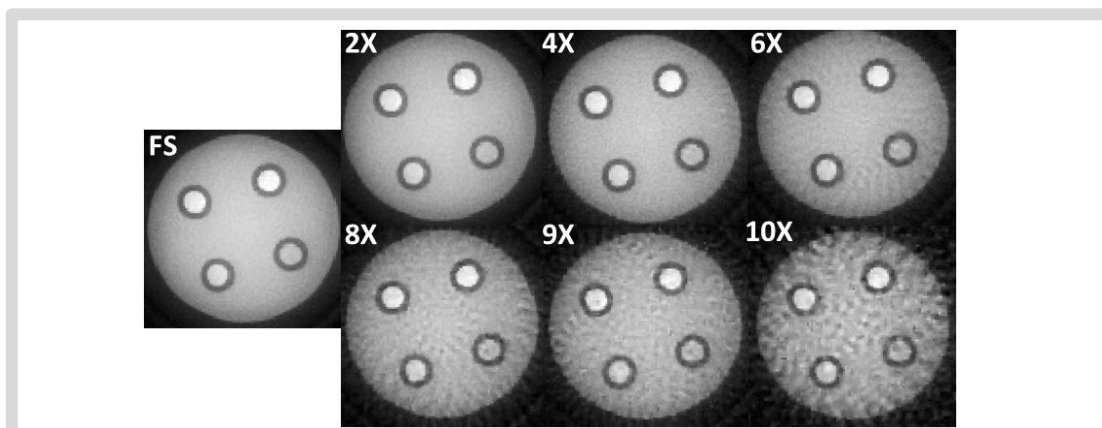
Figure 6. A) Axial mid-slice from a reconstructed 3D volume of a fully sampled (FS) standard acquisition, and different under sampled accelerated CS reconstructions. Accelerations up-to 6X could recover the image quality of the standard acquisition. Higher accelerations (>=8X) were visually judged poor in quality.

Fig. 7A shows the placement of the navigator slice and the 3D imaging volume on a long-axis survey scan of the mouse heart. In Fig. 7B, a representative signal trace from the navigator slice placed at the base of the heart is plotted as function of time. The navigator slice was examined at different locations (apex, base and middle of the heart). In all cases the navigator signal was sensitive to the cardiac and respiratory motion. The cardiac cycle and respiratory phases could be easily distinguished as rapid oscillations (cardiac motion)

interrupted by periodic larger signal changes (respiratory motion), respectively. Based on this navigator signal, the data could be reconstructed retrospectively with 8 frames per cardiac cycle. Because of the retrospective triggering and relatively short scan time for the 4D acquisition, the k-space is not fully acquired. The acquired k-space was ~60%. However, better and more accurate reconstruction could be achieved using compressed sensing method applied on the acquired undersampled kt-space.

Figure 7. A) The navigator slice is planned at the base of the heart. B) Representative example of the navigator signal amplitude as function of time. The rapid oscillation in the amplitude is due to cardiac motion, whereas the larger changes, lower frequency in amplitude are due to respiration.
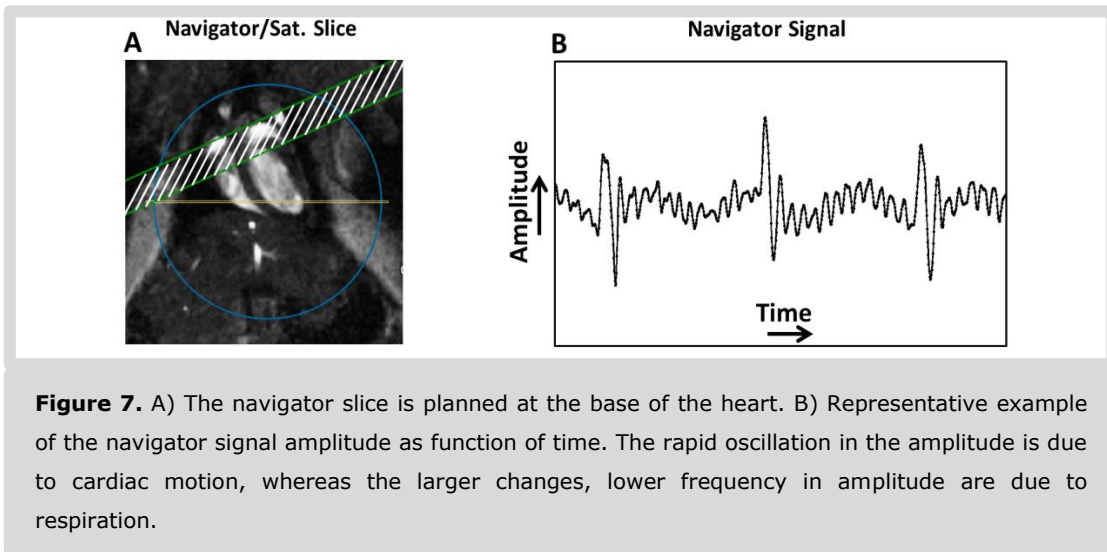
In Figs. 8A and 8B, the comparison between linear and CS reconstructions of the murine abdomen at one of the time points in both the axial and coronal views is shown. CS reconstruction improved the image quality markedly. Basic anatomical features, including heart, lungs, aorta and stomach could be distinguished. However, overall the images had a blurred appearance and the contrast in the images is particularly poor. Focusing on the heart, because of poor contrast it was extremely difficult to distinguish the myocardial wall from the blood pool in the LV lumen, making accurate segmentations impossible.

4.4   Discussion

Reduction of the TE is beneficial for PC flow measurements as it reduces intravoxel dephasing particularly at high magnetic field strength [20-24]. O'Brein et al. reported a TE of 0.65 ms for more accurate flow measurement of high-velocity turbulent stenotic jets

when utilizing UTE-based PC technique [25]. Therefore, developing and implementing UTE-based phase-contrast sequences is necessary in order to improve fast flow imaging. Moreover, radial sampling is beneficial for accelerated imaging with CS reconstruction as it achieves undersampling aliasing artifacts with high incoherence [26-27]. It has been reported that in high-field pre-clinical scanners, the accuracy of spin phase could be severely affected by strong eddy currents which are inevitably induced during the switch of magnetic gradients [28-30]. The radial acquisitions like the UTE sequence used in this study, are more susceptible to eddy current problems.

Figure 8. A) Coronal and B) axial views of the abdomen (LR: liver, H: Heart, L: Lung, S: Stomach and AA: Abdominal Aorta) for a representative case using the proposed sequence with (left) linear and (right) CS accelerated reconstructions. Improved reconstructions could be achieved using compressed sensing method applied on the acquired undersampled kt-space

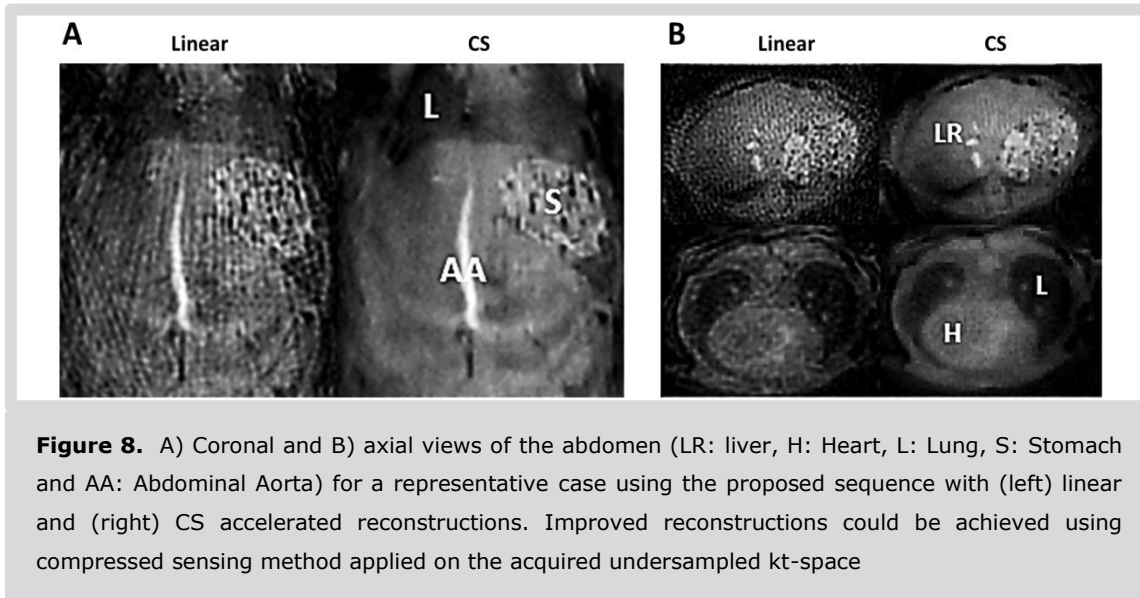As shown in the results section, the induced eddy current leads to phase accumulation and miscalculation of flow velocity. In addition, the bipolar gradients produce eddy currents that induce a linear phase shift in the phase maps. For minimizing this effect, a delay between bipolar gradients and the start of the readout could be added. However this will affect the TR leading to longer acquisition time as well as to longer TE. In this chapter, we showed a simple correction algorithm in which the background linear phase shift that is estimated from a no-flow (static region) through all the slices is subtracted from the estimated phase maps. In future work, a more robust correction algorithm as reported in [19, 29-31] could be implemented.

Apparently, in the preliminary in vivo results, there was a poor contrast to noise ratio (CNR) between the blood and myocardium. This makes it very difficult to distinguish the myocardial wall. Maximizing the contrast between the blood and myocardium could be achieved by the application of a saturation slices at the base of the heart. This will saturate the magnetization of inflowing blood as shown in [32, 33]. Another way could be to make the blood brighter by the injection of Gd-based blood-pool agent that reduces the T_1 of blood. For phase contrast experiments, the signal from the blood is the signal of interest. This means that application of signal saturation cannot be employed. However, contrast between blood and myocardium is not critical for 4D flow as long as a proper anatomical reference scan with sufficient contrast is available.

In this chapter, the reconstruction quality with different degrees of undersampling was judged visually. In future work, in vivo experiments to calculate the highest achievable degree of undersampling, quantitatively, are still to be conducted. We also believe that other sparsifying transforms that exploit the redundancy of the phase contrast experiments might be useful rather than the spatio-temporal variation used in this work. Phantom measurements showed promising results for phase contrast experiments. However, sequence optimization and in vivo phase contrast experiments still have to be performed.

4.5 Conclusion

In conclusion, the aim of this chapter was to explore the utility of a 4D UTE sequence to acquire full anatomical and flow maps with high isotropic resolution and short echo times. 4D imaging suffers from long scan times, which could be mitigated by using undersampling and a CS reconstruction pipeline. Phantom experiments showed promising results. However in vivo sequence optimization and further validation have to be conducted in future experiments.

References

1. Gatehouse, P.D. and G.M. Bydder, *Magnetic resonance imaging of short T2 components in tissue.* Clin Radiol, 2003. **58**(1): p. 1-19.
2. Robson, M.D., et al., *Magnetic resonance: an introduction to ultrashort TE (UTE) imaging.* J Comput Assist Tomogr, 2003. **27**(6): p. 825-46.
3. Bergin, C.J., G.H. Glover, and J.M. Pauly, *Lung parenchyma: magnetic susceptibility in MR imaging.* Radiology, 1991. **180**(3): p. 845-8.
4. Du, J., et al., *Qualitative and quantitative ultrashort echo time (UTE) imaging of cortical bone.* J Magn Reson, 2010. **207**(2): p. 304-11.
5. Chan, C.F., et al., *Ultra-short echo time cardiovascular magnetic resonance of atherosclerotic carotid plaque.* J Cardiovasc Magn Reson, 2010. **12**: p. 17.
6. de Jong, S., et al., *Direct detection of myocardial fibrosis by MRI.* J Mol Cell Cardiol, 2011. **51**(6): p. 974-9.
7. Gatehouse, P.D., et al., *Applications of phase-contrast flow and velocity imaging in cardiovascular MRI.* Eur Radiol, 2005. **15**(10): p. 2172-84.
8. Nayler, G.L., D.N. Firmin, and D.B. Longmore, *Blood flow imaging by cine magnetic resonance.* J Comput Assist Tomogr, 1986. **10**(5): p. 715-22.
9. Pelc, N.J., et al., *Phase contrast cine magnetic resonance imaging.* Magn Reson Q, 1991. **7**(4): p. 229-54.
10. Rebergen, S.A., et al., *Magnetic resonance measurement of velocity and flow: technique, validation, and cardiovascular applications.* Am Heart J, 1993. **126**(6): p. 1439-56.
11. Markl, M., et al., *Time-resolved 3D MR velocity mapping at 3T: improved navigator-gated assessment of vascular anatomy and blood flow.* J Magn Reson Imaging, 2007. **25**(4): p. 824-31.
12. Markl, M., et al., *Time-resolved 3-dimensional velocity mapping in the thoracic aorta: visualization of 3-directional blood flow patterns in healthy volunteers and patients.* J Comput Assist Tomogr, 2004. **28**(4): p. 459-68.
13. Markl, M., P.J. Kilner, and T. Ebbers, *Comprehensive 4D velocity mapping of the heart and great vessels by cardiovascular magnetic resonance.* J Cardiovasc Magn Reson, 2011. **13**: p. 7.
14. Janiczek, R.L., et al., *Three-dimensional phase contrast angiography of the mouse aortic arch using spiral MRI.* Magn Reson Med, 2011. **66**(5): p. 1382-90.
15. Kadbi, M., et al., *4D UTE flow: A phase-contrast MRI technique for assessment and visualization of stenotic flows.* Magn Reson Med, 2014.
16. Pelc, N.J., et al., *Encoding strategies for three-direction phase-contrast MR imaging of flow.* J Magn Reson Imaging, 1991. **1**(4): p. 405-13.
17. Bovenkamp, P.R., et al., *Velocity mapping of the aortic flow at 9.4 T in healthy mice and mice with induced heart failure using time-resolved three-dimensional phase-contrast MRI (4D PC MRI).* Magnetic Resonance Materials in Physics, Biology and Medicine, 2014: p. 1-13.
18. Fessler, J.A. and B.P. Sutton, *Nonuniform fast Fourier transforms using min-max interpolation.* Ieee Transactions on Signal Processing, 2003. **51**(2): p. 560-574.
19. Jehenson, P. and A. Syrota, *Correction of Distortions Due to the Pulsed Magnetic-Field Gradient-Induced Shift in B0 Field by Postprocessing.* Magnetic Resonance in Medicine, 1989. **12**(2): p. 253-256.
20. Spielmann, R.P., et al., *Appearance of Poststenotic Jets in Mri - Dependence on Flow Velocity and on Imaging Parameters.* Magnetic Resonance Imaging, 1991. **9**(1): p. 67-72.
21. Schmalbrock, P., et al., *Volume Mr Angiography - Methods to Achieve Very Short Echo Times.* Radiology, 1990. **175**(3): p. 861-865.
22. Stahlberg, F., et al., *Quantification of Complex Flow Using Mr Phase Imaging - a Study of Parameters Influencing the Phase-Velocity Relation.* Magnetic Resonance Imaging, 1992. **10**(1): p. 13-23.
23. Nayak, K.S., B.S. Hu, and D.G. Nishimura, *Rapid quantitation of high-speed flow jets.* Magn Reson Med, 2003. **50**(2): p. 366-72.
24. O'Brien, K.R., et al., *MRI phase contrast velocity and flow errors in turbulent stenotic jets.* J Magn Reson Imaging, 2008. **28**(1): p. 210-8.
25. O'Brien, K.R., et al., *Phase contrast ultrashort TE: A more reliable technique for measurement of high-velocity turbulent stenotic jets.* Magn Reson Med, 2009. **62**(3): p. 626-36.
26. Doneva, M., et al. *Highly undersampled 3D golden ratio radial imaging with iterative reconstruction*. in *Intl Soc Mag Reson Med*. 2008.

27.   Feng, L., et al., *Golden-angle radial sparse parallel MRI: combination of compressed sensing, parallel imaging, and golden-angle radial sampling for fast and flexible dynamic volumetric MRI.* Magn Reson Med, 2014. **72**(3): p. 707-17.

28.   Moussavi, A., et al., *Correction of gradient-induced phase errors in radial MRI.* Magn Reson Med, 2014. **71**(1): p. 308-12.

29.   Espe, E.K.S., L.L. Zhang, and I. Sjaastad, *Unwrapping Eddy Current Compensation: Improved Compensation of Eddy Current Induced Baseline Shifts in High-Resolution Phase-Contrast MRI at 9.4 Tesla.* Magnetic Resonance in Medicine, 2014. **72**(4): p. 1096-1102.

30.   Atkinson, I.C., A.M. Lu, and K.R. Thulborn, *Characterization and Correction of System Delays and Eddy Currents for MR Imaging with Ultrashort Echo-Time and Time-Varying Gradients.* Magnetic Resonance in Medicine, 2009. **62**(2): p. 532-537.

31.   Block, K. and M. Uecker. *Simple method for adaptive gradient-delay compensation in radial MRI*. in *Proceedings of the International Society for Magnetic Resonance in Medicine*. 2011.

32.   Nieman, B.J., K.U. Szulc, and D.H. Turnbull, *Three-Dimensional, In Vivo MRI With Self-Gating and Image Coregistration in the Mouse.* Magnetic Resonance in Medicine, 2009. **61**(5): p. 1148-1157.

33.   Coolen, B.F., et al., *Regional contrast agent quantification in a mouse model of myocardial infarction using 3D cardiac T1 mapping.* J Cardiovasc Magn Reson, 2011. **13**: p. 56.

Human Carotid Pulse Wave Velocity Measurements Using Accelerated High Temporal Resolution MRI

As you go, you will make mistakes of your own

But son, that's alright, you live and you learn

I'm here and I'll be if I can …

Related Articles :

- ➢ Abdallah G. Motaal, Wouter V Potters, Huiming Dong, Luc Florack, Klaas Nicolay, Aart Nederveen, Gustav J. Strijkers, Bram F. Coolen. Carotid Pulse Wave Velocity Measurements Using Accelerated High Temporal Resolution MRI. Proceedings of the International Society for Magnetic Resonance in Medicine (ISMRM), 2015, Canada.

Abstract

Arterial stiffness is one of the major biomarkers of early atherosclerotic disease. A common method to assess vessel wall stiffness is measuring the pulse wave velocity (PWV) of the pulse wave created by cardiac contraction. Global PWV measurements are possible by using carotid/femoral Doppler Ultrasound. However, these give little information on local changes in vessel wall stiffness at relevant atherosclerotic-prone sites. In this chapter, we present a novel method for local PWV measurements in the carotid artery based on highly accelerated phase-contrast MRI flow measurements with high temporal resolution of 200 frames/cardiac cycle. PWV was determined based on two methods: 1) cross correlation (CC-method) of two time-resolved flow curves from the common and internal carotid artery, 2) a slice-specific measurement of the flow vs. lumen area time curve (QA-method). The reconstructed images have high in-plane spatial resolution of 0.54 mm and 0.86 mm for the QA and CC method, respectively. Estimated PWV values in healthy volunteers were in the range of 2.5-6.5 m/sec. The two methods were highly correlated (r=0.82), with a mean difference of 0.42 m/s. Reproducibility measurements showed a coefficient of variation of 15.6% and 12.1% for the CC- and QA-method, respectively. In conclusion, we showed that MRI based measurements of local carotid PWV are feasible. We expect that our novel method will facilitate measurements in elderly volunteers and patients with above-normal PWV values.

5.1   Introduction

Atherosclerosis is the main underlying cause of cardiovascular disease and considered one of the leading causes of death worldwide. To improve treatment and risk prevention, a great need exists for diagnostic tools that identify patients at high risk and assess the vulnerability of the vessel wall for atherosclerosis at an early stage. The pulse wave velocity (PWV) of the pulse wave created by cardiac contraction is a measure of arterial stiffness and has been proven to deliver an independent predictor for cardiovascular events [1]. Nesbitt et al. reported elevation of PWV in patients with atherosclerosis [2]. Furthermore, age-related regional aortic PWV changes have recently been demonstrated [3].

Currently, Doppler Ultrasound measurements of carotid-femoral pulse wave velocity (cf-PWV) are considered the non-invasive gold standard index for global arterial stiffness assessment. PWV is calculated by determining the time taken for the arterial pulse to propagate from the carotid to the femoral artery relative to the distance between these points. There is, however, considerable importance of obtaining local PWV values in specific regions of interest. First, it is well known that the stiffness of the arteries is not uniform along the vasculature tree and it increases from proximal to the distal regions [4]. Secondly, the arteries are non-uniform along the vasculature especially in elderly and patients with vascular diseases, which as a consequence affects the distance measurements. Finally, in the carotid and femoral arteries, the two measurement points do not lie on the same path of the pulse wave propagation [5], since the pulse wave travels in two opposite directions. Therefore, measurements of regional PWV, instead of global PWV, can be of great interest.

Phase-contrast MRI is a promising technique for assessment of local PWV, in which time-resolved flow measurements are acquired throughout the cardiac cycle [6-10]. This has been applied in the aorta by measuring a slice that intersects both the descending and

ascending aorta. Using the so called foot-to-foot method (FF), PWV is calculated as the ratio of the distance between descending and ascending aortas and the time difference between the arrival of the foot of the pulse wave at these levels [11-14]. A more robust approach is the cross-correlation method (CC) [15], in which the correlation between the two pulse waves is calculated for several time shifts. The maximum value will correspond to the actual time shift between the two flow curves, after which the PWV can then be estimated from the traveled distance. An even more local PWV quantification method is based on the relationship between the flow (Q) and the area (A) of the vessel in early systole [3, 16-18]. So far, this so-called QA-method has only rarely been used in the MRI field, mainly because of the high demands on the quality of the MRI scans and the subsequent post processing for accurate lumen area detection.

Of all the larger arteries, PWV measurements in the carotids are of particular interest, since they are major atherosclerosis-prone site associated with stroke [19]. Compared to the aorta, PWV measurements in the carotid artery using MRI require a significant increase in spatial and temporal resolution in order to cope with the smaller lumen diameter (4-6 mm) and the shorter time lag between the flow profiles observed in two slices. Currently, the spatiotemporal resolution is limited by available scan time and the lowest achievable repetition time of the velocity-encoded phase-contrast acquisition.

In this chapter, we demonstrate a new protocol for high spatiotemporal resolution flow-encoded imaging and PWV quantification in the carotid arteries, based on a combination of a Compressed Sensing (CS) acceleration technique [20] and retrospective triggering reconstruction [21-23]. We will show that this approach allows for flow measurements with a high temporal resolution up to 5 ms with spatial resolution of 0.54 mm and 0.86 mm for the QA and CC methods, respectively, and with a total scan time of 6 min for both methods. The methods were validated using a flow phantom. Subsequently, the PWVs in the carotids of 5 volunteers were measured and compared.

5.2 Material and Methods

5.2.1 MR Measurements

MRI measurements were performed with a whole-body 3T MR scanner (Philips Ingenia) and eight-channel RF receiver neck coil. A fast field echo (FFE) phase contrast MR sequence with unidirectional velocity encoding, i.e. velocity encoding experiments (VE) = 2, was used with the following parameters: VENC = 120 cm/s; TE/TR/FA = 3.28 ms/10.58 ms/20°; slice thickness = 3 mm; FOV = 136x136 mm^2, and acquisition matrix = 160x160 and 250x250, resulting in a spatial resolution of 0.85 and 0.54 mm and for the CC and QA methods, respectively. The higher spatial resolution for the QA method is needed for accurate lumen area detection. Fig. 1 shows the proposed MR sequence, with which a very high temporal resolution data with sufficient number of averages could be achieved using a retrospective triggering method. The data is acquired continuously and asynchronously with the heartbeat, while the phase encoding gradient is changed every R-R interval.

5.2.2 Under sampled Variable-Density Sampling

As the center of k-space contains most of the signal information, a Gaussian-shaped variable-density sampling pattern was designed to sample the center k-lines more frequently compared to the rest of k-space regions. The use of retrospective triggering with constant TR leads to random sampling because of the R-R variability as shown in Fig. 2. The weighted pseudo-random sampling is favorable because of the high incoherence of the undersampling artifacts produced in the corresponding spatial domain [24, 25]. The unit with which the acquisition duration of one specific k-line is described is the heartbeat (e.g., n heartbeats of k-line p). The number of repetitions N_i for a specific k-line i is given:

$$N_i = \beta \cdot e^{\frac{(i-\mu)^2}{2 \cdot \sigma^2}}$$

(5.1)

Here N_i is given in units of heartbeat, μ is the number of k-lines/2, β determines the number of repetitions of the central k-line, and σ is the width of the Gaussian function. In addition, for efficient k-space sampling, a partial Fourier factor of 30% was used.
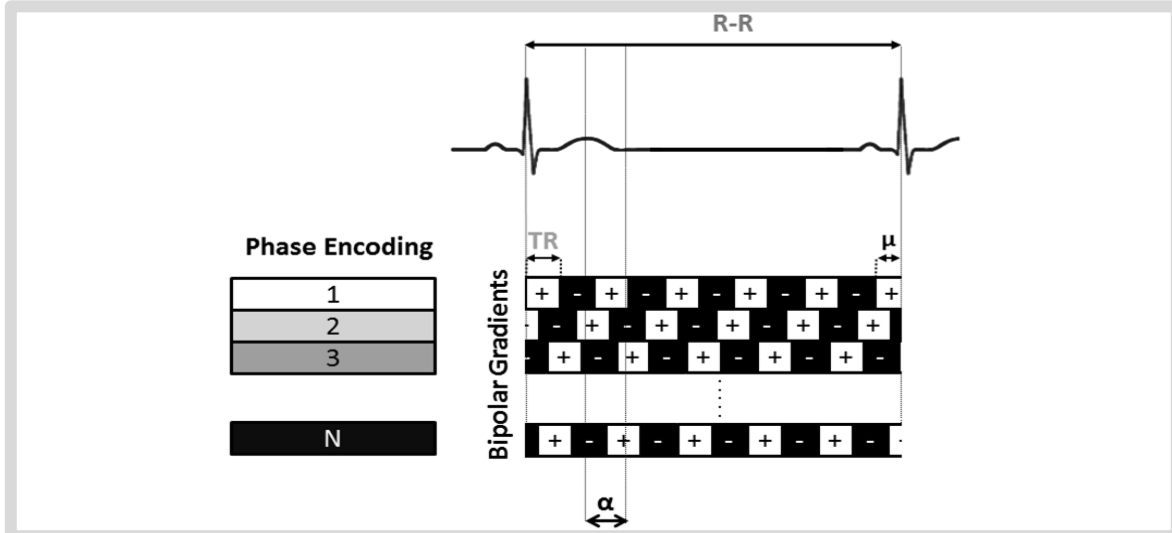
Figure 1. Schematic diagram of the pulse sequence. The phase encoding step was switched every R-R interval, and the data was acquired continuously and asynchronously with the cardiac motion. Small variations in cardiac cycle length ensure that TR is not a multiple of the R-R interval as indicated with μ, leading to time-shifted acquisition of k-lines and a random filling of k-space. Retrospectively, k-lines are collected in bins of the desired temporal resolution, **α** ,using the cardiac triggering and respiratory gating information from the recorded ECG.

5.2.3 Compressed Sensing Reconstruction

Retrospectively undersampled data were reconstructed using a three-dimensional compressed sensing algorithm. Sparsity of the desired image in spatial domain and along the time-axis, as well as its total variation along time-axis were used as constraints. The image reconstruction can be formulated as the following optimization problem:

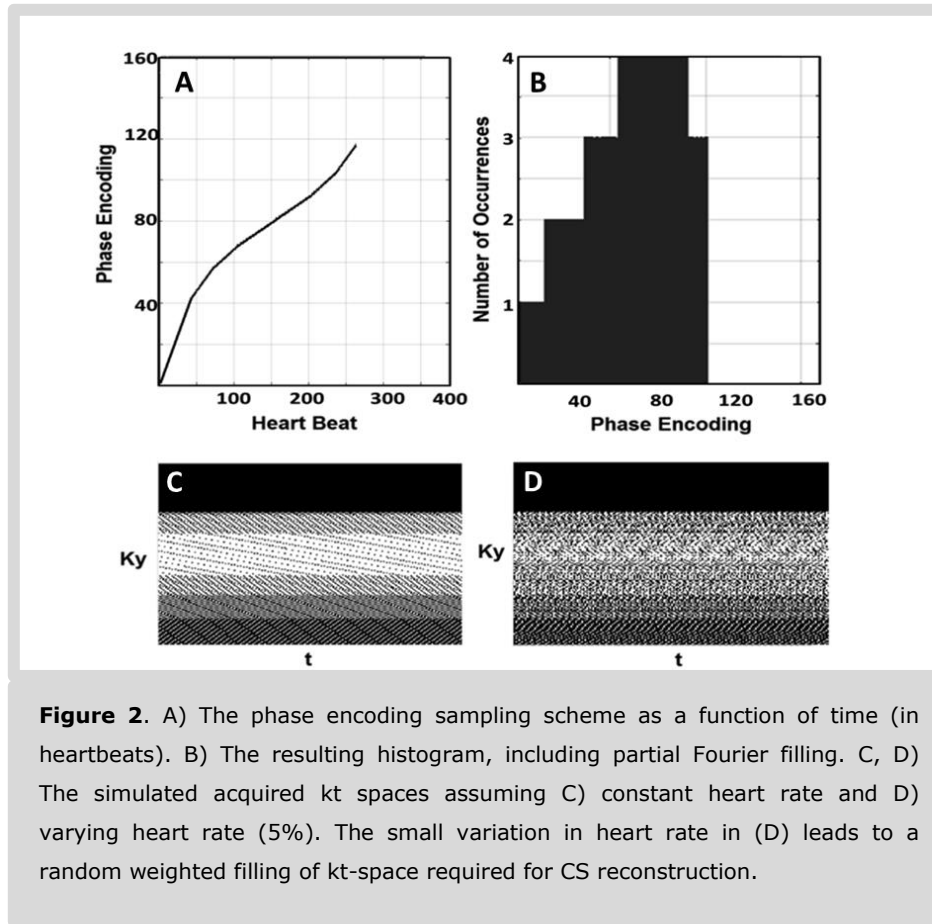$$min_m\{\,||F_s m - y||_2^{\,2} + \vartheta_1\,||\partial(m)||_1 + \vartheta_2 TV(m) \tag{5.2}$$

where m is a (3D) volume of the reconstructed images, ∂ is the sparsifying transformation, y is the acquired data from the scanner, *TV* stands for total variation along the time-axis,

and F_s is the undersampled Fourier operator according to the designed sampling pattern. The optimization involves 3 dimensions (2 spatial and 1 time dimension). The regularization parameters ϑ_1 and ϑ_2 control the trade-off between reconstructed image sparsity in the transform domain and TV penalty. They were heuristically defined by comparing CS-reconstructed magnitude and phase images to the fully-sampled dataset. ϑ_1 and ϑ_2 were set to 0.03 and 0.12, respectively. Once optimized and calibrated using the phantom data, all parameters were fixed to reconstruct the in vivo images. A non-linear conjugated gradient descending algorithm was used to solve the minimization problem.

5.2.4   Flow phantom and simulations

A customized in vitro flow phantom (Fig. 3) was used to validate whether the weighted retrospectively gated acquisition was suitable for reconstructing high temporal resolution flow values. The phantom was a model created by segmenting a healthy volunteer carotid artery and smoothing the surface. Three flow-extensions (straight pipes) were connected to a computer-controlled water pump that applied a flow waveform mimicking the carotid arterial blood flow pattern.

The MR sequence parameters were equal to those of the CC-method (see section 5.2.1). A fully-sampled Cartesian k-space was then acquired with 25 dynamics (ND = 25), where one dynamic is capable to reconstruct ~ 50 fully sampled time frames (NF = 50). The total scan time for the phantom measurement was (NP x ND x NF x TR x VE) = 62 min. This highly oversampled dataset allowed reconstruction of 200 fully sampled time frames, resulting in high temporal resolution gold standard flow profiles. Undersampled kt-space sampling patterns were generated using computer simulations with different β and σ values, as explained in the previous section. The trajectory that gave the highest incoherent artifacts was selected, and subsequently, undersampled acquisition schemes were generated by subsampling the fully-sampled data. We aimed to achieve 3 and 6 minute scan times per slice for the CC and the QA method, respectively.

Figure 2. A) The phase encoding sampling scheme as a function of time (in heartbeats). B) The resulting histogram, including partial Fourier filling. C, D) The simulated acquired kt spaces assuming C) constant heart rate and D) varying heart rate (5%). The small variation in heart rate in (D) leads to a random weighted filling of kt-space required for CS reconstruction.

5.2.5   In-Vivo Experiments

Carotid artery PWV scans were performed in 5 healthy male volunteers (age: 25-30). Axial slices were positioned to intersect the common and internal carotid arteries as shown in Fig. 4. The resulting data was subsequently reconstructed with a three-dimensional (2D + time) CS algorithm as described in section 5.2.3. Using the phase images, flow-time curves were calculated for each vessel. Finally, PWV analysis was performed using 1)-CC method by calculating the time-shift in the flow curves of the vessels in two axial slices separated with a distance d. The time-shift 't' was determined by the maximum cross-correlation between the (time-shifted) flow curves. The PWV is then given by PWV=d/t. 2)- QA method in single slice, where the PWV could be calculated

from the relation of the change of the blood flow and surface area during systole. In this case, the PWV is given by PWV=ΔQ/ΔA.
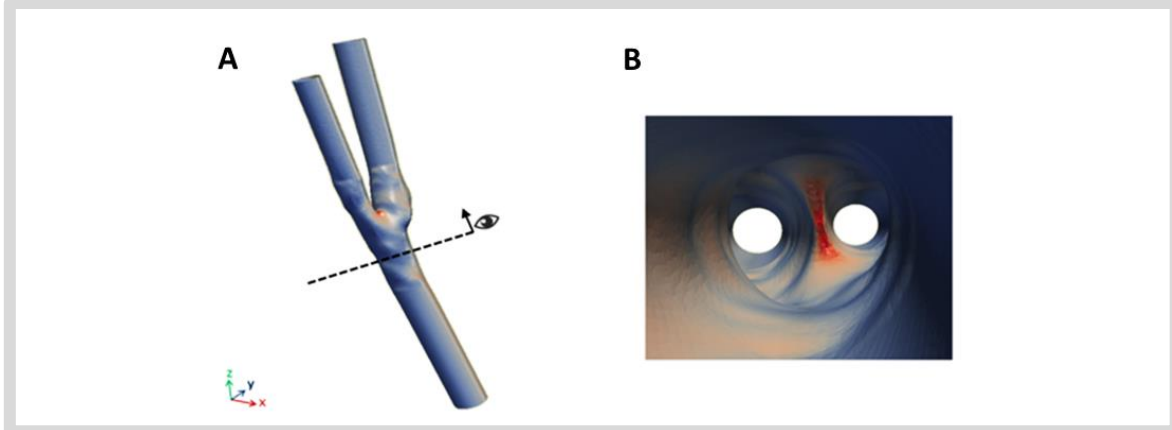
Figure 3. The phantom model. A) Surface rendering for the segmentation of healthy volunteer carotid artery. The model is connected to a computer-controlled water pump. B) Cross section in the common carotid artery at the location of the dashed line in A, where the arrow points to eye sight direction.
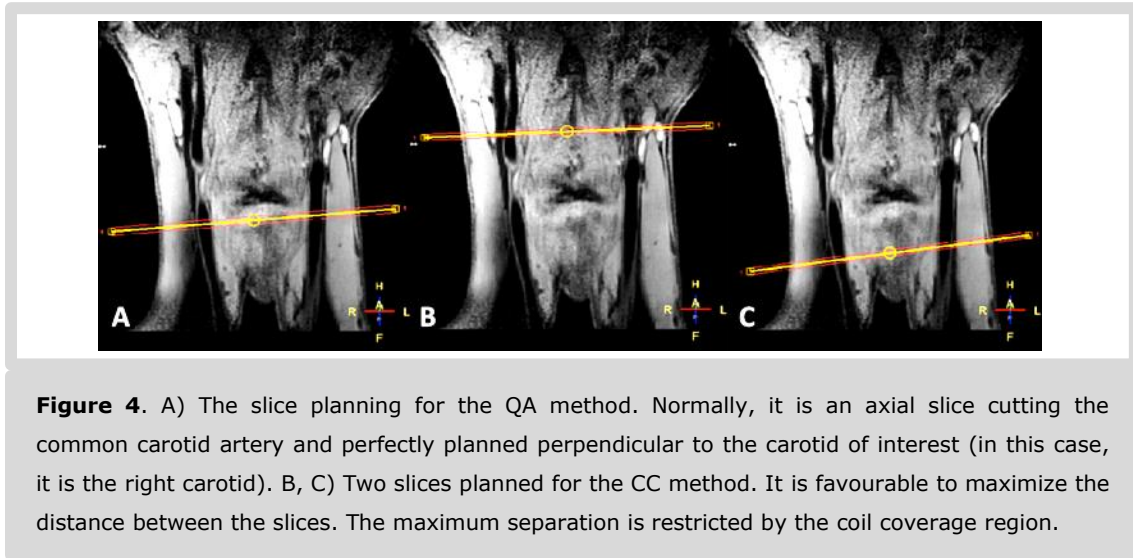
5.2.6   Automatic Segmentation and PVW Calculation

Accurate segmentation of the carotid lumen area is essential for an accurate PWV estimation using the QA method. The high temporal resolution of our method makes manual delineation unpractical and time consuming. Therefore an automatic 2D-t segmentation approach was implemented [26]. The segmentation was based on a deformable contour v(s, t) optimized to equilibrate internal and external energy terms. The internal energy is given by:

$$E(v)_{int} = \alpha_s \left| \frac{\delta v}{\delta s} \right|^2 + \alpha_t \left| \frac{\delta v}{\delta t} \right|^2 + \beta_s \left| \frac{\delta^2 v}{\delta s^2} \right|^2 + \beta_t \left| \frac{\delta^2 v}{\delta t^2} \right|^2 \qquad (5.3)$$

where α_s and α_t are elasticity parameters that aim to shorten the contour length and β_s and β_t are curvature smoothness parameters. These regularization parameters act both in the spatial domain as well as in the time domain. The time domain regularization ensures the frame-to-frame contour stability. The parameters α_s, α_t, β_s and β_t were set to 0.3, 1.5,

0.01 and 0.75 respectively. Values were heuristically defined using a visual assessment of the quality of the segmentation. The external energy, E_{ext}, is based on the gradient field of the original image, which was estimated from the first-order finite difference calculated in the x and y directions.
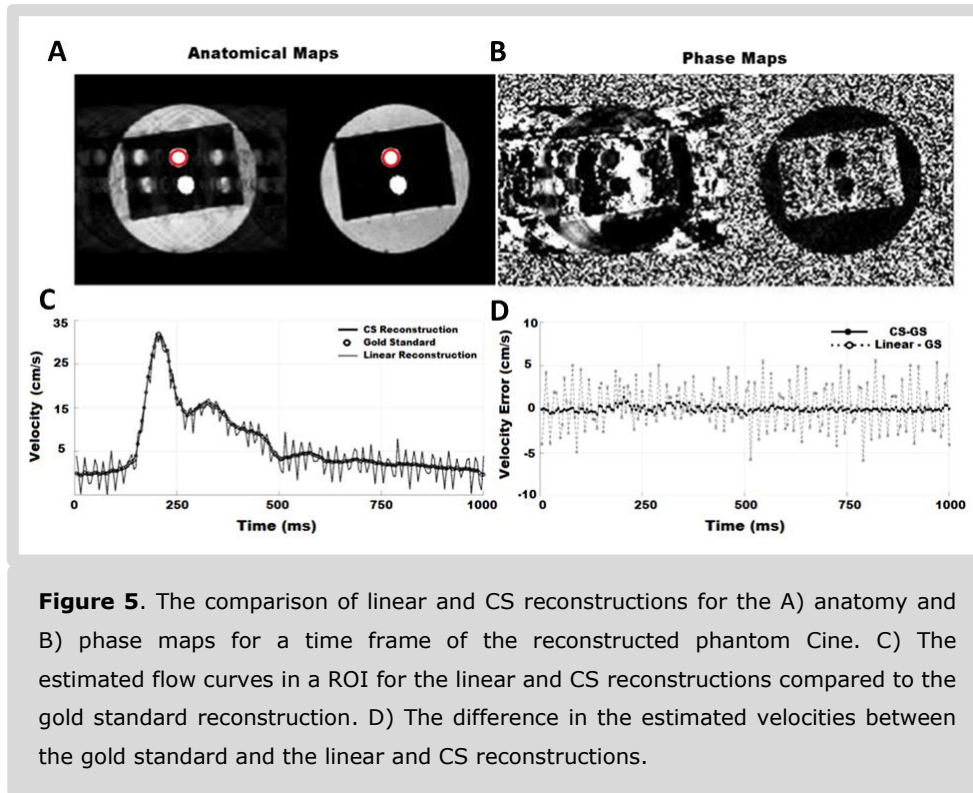

Figure 4. A) The slice planning for the QA method. Normally, it is an axial slice cutting the common carotid artery and perfectly planned perpendicular to the carotid of interest (in this case, it is the right carotid). B, C) Two slices planned for the CC method. It is favourable to maximize the distance between the slices. The maximum separation is restricted by the coil coverage region.

5.3   Results

Fig. 5A and 5B show representative magnitude and phase images from the flow phantom measurements after reconstruction of 200 frames/sec. Because of the retrospective triggering acquisition and the relatively short scan time, the acquired k-space was significantly undersampled, with an average coverage of kt-space of only 25%. When applying a regular inverse Fourier directly to the undersampled data, aliasing occurs in the magnitude and flow image data (Figs. 5A and 5B, left images). However, the CS reconstruction algorithm effectively removed these undersampling artifacts (Figs. 5A and B, right images).

Fig.5C shows flow curves as function of time from the red ROI in Fig.5A. The open circles form the gold standard flow curve, reconstructed from fully sampled data. For the regular linear inverse Fourier data (dashed line), the flow curve followed the general trend of the
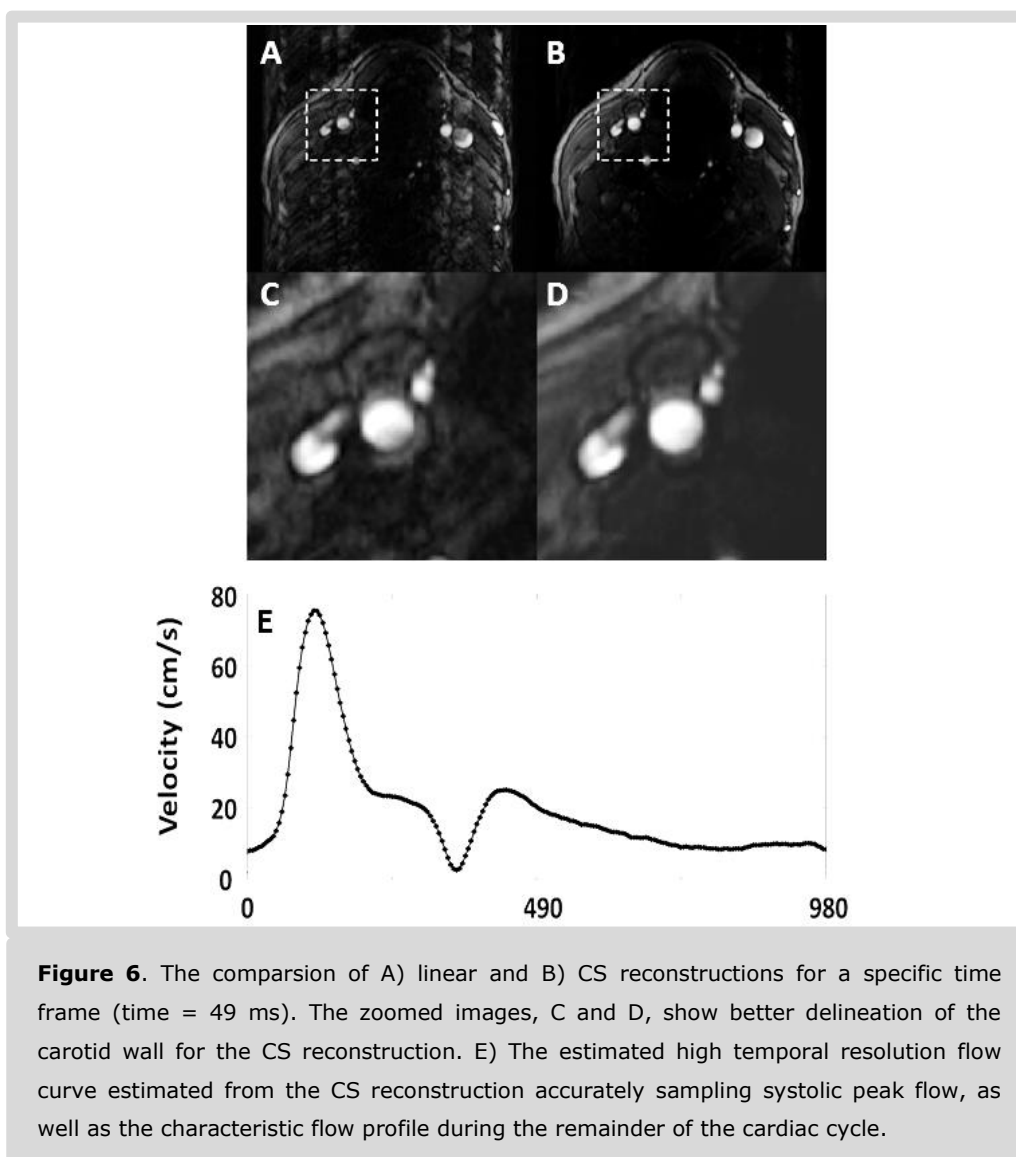
gold standard curve. However, the flow curve was severely distorted by aliasing artifacts. The CS reconstruction (solid line) was able to recover the gold standard flow curve accurately and both flow curves were visually nearly identical. The differences between the gold standard and CS and linear reconstructed flow curves are shown in Fig.5D.

Figure 5. The comparison of linear and CS reconstructions for the A) anatomy and B) phase maps for a time frame of the reconstructed phantom Cine. C) The estimated flow curves in a ROI for the linear and CS reconstructions compared to the gold standard reconstruction. D) The difference in the estimated velocities between the gold standard and the linear and CS reconstructions.

For the in vivo experiments, the top row in Fig. 6 shows the comparison of linear and CS reconstructions of one of the time frames. Clearly, CS reconstruction cleans up the aliasing artifacts and better image quality with good delineation of the carotids was achieved as shown in Fig. 6D. By using a retrospective triggering scheme, detailed flow curves, in which clearly the peak flow point and uniform flow pattern, could be estimated from the reconstructed Cine as shown in Fig. 6E.
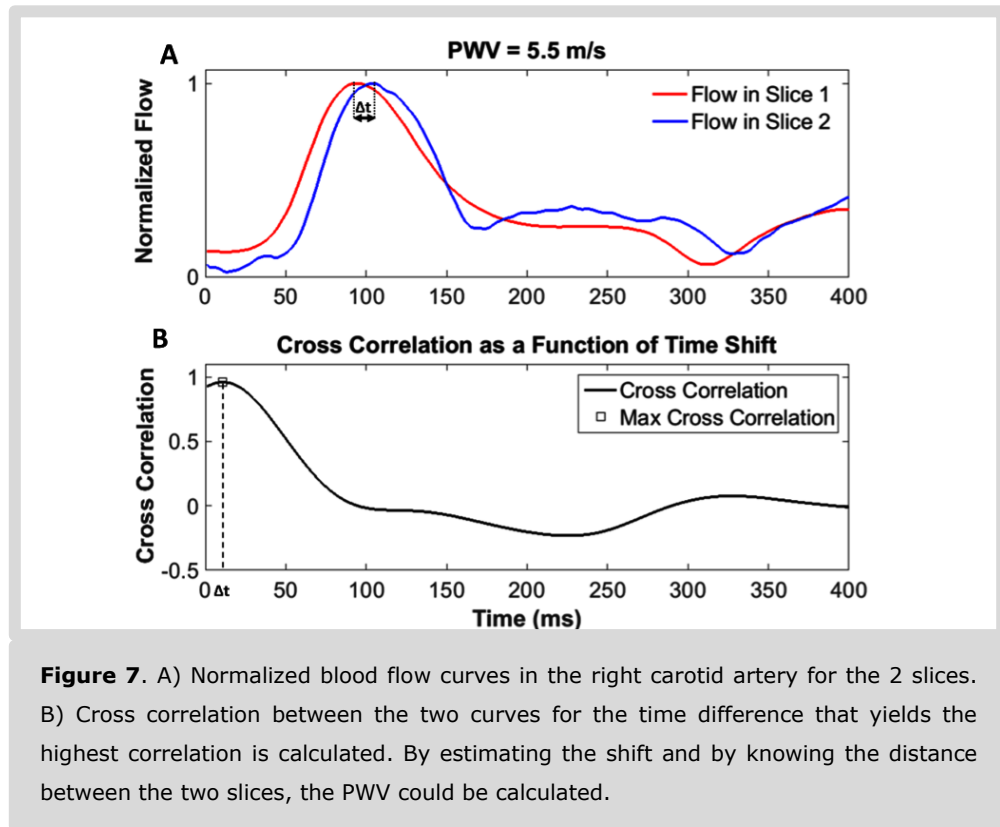
Results obtained by CC and QA methods are depicted in Fig. 7 and 8. For the CC method, in the top row of Fig. 7, the normalized blood flow curves of the carotid artery of a representative case for the two slices are shown (the time axis is cropped and only the

early time points of the flow curves are displayed). High resolution curve of the cross correlation between the two flow curves was obtained allowing accurate determination of the time shift of the peak flow arrival at the two slices.

Figure 6. The comparsion of A) linear and B) CS reconstructions for a specific time frame (time = 49 ms). The zoomed images, C and D, show better delineation of the carotid wall for the CS reconstruction. E) The estimated high temporal resolution flow curve estimated from the CS reconstruction accurately sampling systolic peak flow, as well as the characteristic flow profile during the remainder of the cardiac cycle.

For the QA method, in the left column of Fig. 8, the normalized blood flow and surface area of the right carotid artery of a representative case is shown. Clearly it shows the change of the carotid artery lumen area with the blood flow rate, illustrating the response of vessel dilation to the increase in blood flow. In the right column, the change in the

blood flow and carotid surface area with time is plotted. During systole, a clear linear relation was observed, allowing linear fitting from which the PWV could be estimated. Reproducibility results are shown in Figs. 9A and 9B, together with corresponding Bland Altman plots in Fig. 10A and 10B. The estimated PWV differences were almost equal and distributed around small bias values of 0.416 m/s and -1.13 m/s with confidence intervals of [-0.93 1.77] and of [2.57 -4.84] m/s for the right and left carotid arteries, respectively.

Figure 7. A) Normalized blood flow curves in the right carotid artery for the 2 slices. B) Cross correlation between the two curves for the time difference that yields the highest correlation is calculated. By estimating the shift and by knowing the distance between the two slices, the PWV could be calculated.

The coefficient of variation (CV) was 15.29% and 27.7% for CC and QA methods respectively. In case of taking into consideration only the right carotid artery, to which the imaging slice was perpendicularly planned in the QA method, the CV of the CC and QA method was 15.62 and 12.1%. The relation and agreement between the CC and QA methods for estimating the PWV in the right carotid for the two scan sessions is plotted in Fig. 10C. It is shown that the two methods were well correlated with R=0.83. The

correlation coefficient between the two methods for estimating the PWV in the left carotid artery was R=0.014.
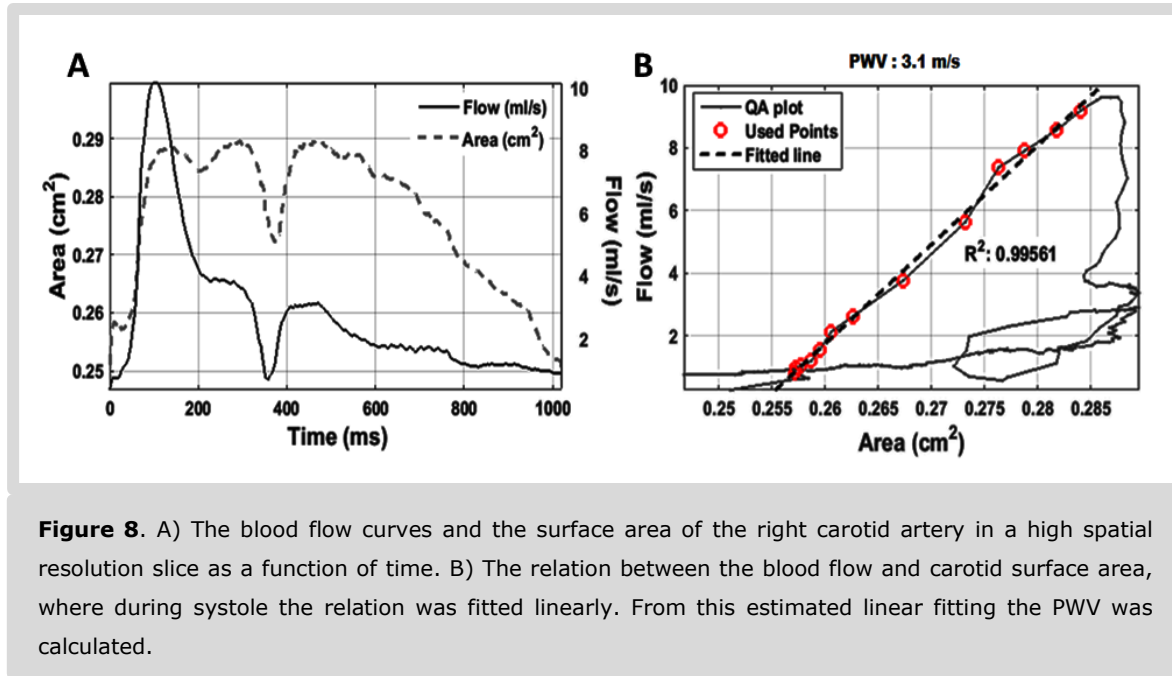

Figure 8. A) The blood flow curves and the surface area of the right carotid artery in a high spatial resolution slice as a function of time. B) The relation between the blood flow and carotid surface area, where during systole the relation was fitted linearly. From this estimated linear fitting the PWV was calculated.

5.4   Discussion

Carotid–femoral PWV estimation using Doppler ultrasound is the most established index of the arterial stiffness. This method provides global information about the arterial tree status. However, the different measurement methods to estimate the arterial path length produces substantial variations in the estimated values [27]. Moreover, the global PWV estimation may fail to detect focal regions of altered stiffness at sites prone to plaque formation. Thus, regional PWV is of clinical importance. Carotid PWV is of great interest, since the carotids are a major site of atherosclerosis development.

Recent progress in MRI technology allows for measuring regional PWV [15, 17, 18, 28-29], avoiding some of the drawbacks related to the standard Doppler ultrasound measurements. Several analytical methods have been used to analyze the acquired data. A frequently used method in both ultrasound and MR based measurements is calculating

the time difference between flow curves at different sites. Therefore, accurate measurement of the distance between the two imaging planes is important.
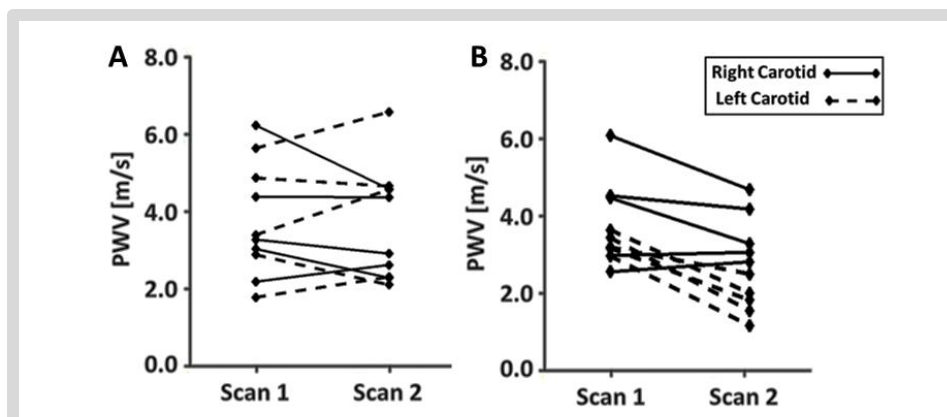

Figure 9. Repeated measurement for the 5 volunteers and the estimated PWV using A) CC and B) QA method in the right and left carotid arteries.
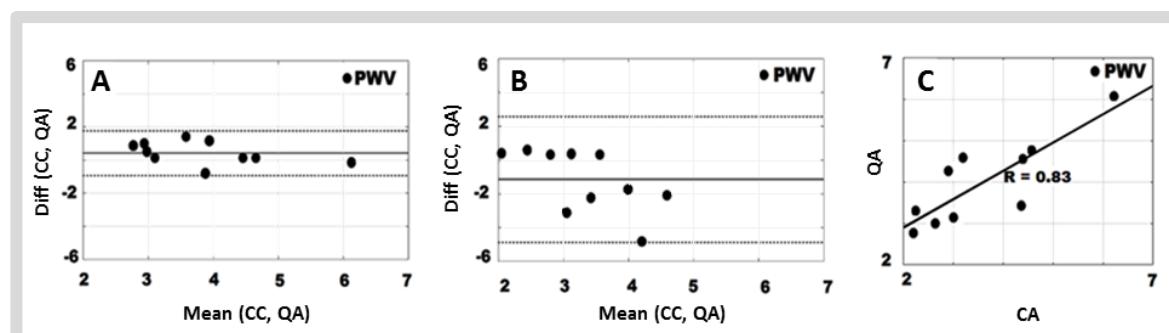
Figure 10. The Bland Altman plot between the QA and CC methods of estimating the PWV in the A) right and B) left carotid arteries for the 5 volunteers in. C) The relation between the two methods for estimating the PWV for the right carotid artery in the two scans session for the five volunteers.

In this chapter, we described a new method to allow for high temporal resolution MRI carotid flow measurements for calculation of local carotid PWV. In the CC-method, based on a sequential acquisition of 2 different slices, average PWV values were obtained representing the most vulnerable part of the carotid around the bifurcation. In a recent study by Westenberg et al. [30] the PWV in the carotid artery was measured using a neck coil with a large coverage (180x172 mm) and temporal resolution of 12.4 ms. The mean

PWV in young volunteers (<30) was 5.7 m/s. Using the slice-specific QA-method, we were able to measure an even more local carotid PWV. In this approach, we found that accurate lumen contour area calculation is crucial to obtain reproducible values. Fig. 11 shows the segmentation results at three different time points, where the segmentation contour is displayed over both the anatomical and phase maps. As shown, the contour tracks the borders of the carotid artery, from which the change in the lumen area with the cardiac cycle was calculated. For optimum choice of parameters involved in the segmentation, a high spatial resolution low temporal resolution T1 weighted scan to measure the actual lumen diameter at several points in the cardiac cycle could be acquired. For our QA analysis, we therefore acquired higher spatial resolution data (0.54 mm) compared to the data acquired for the CC method (0.85 mm), which naturally improved the segmentation procedure. In addition, it is important that the slice is planned perpendicular to the carotid vessel, which restricts accurate measuring of the PWV for both carotid vessels at the same time, since these are not perfectly parallel to each other. This could be the reason of the low correlation between the QA and CC method that we obtained in the left carotid artery.
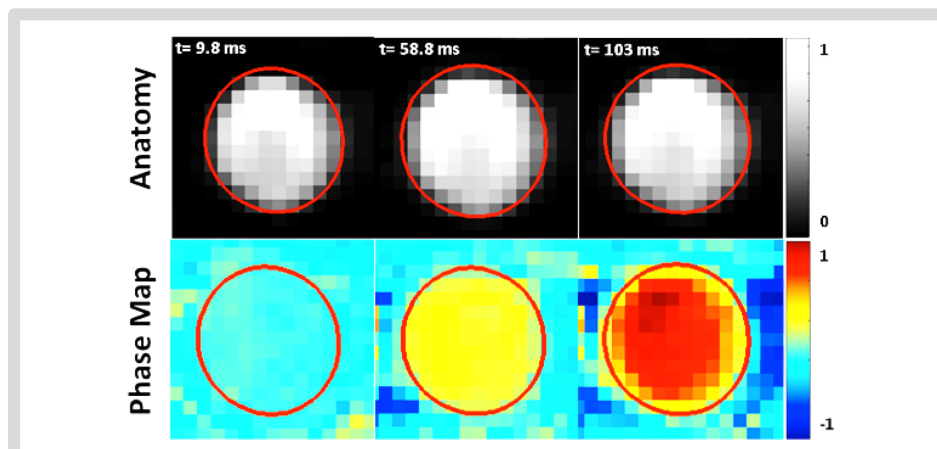
Figure 11. The segmentation results at three different time points (9.8, 58.8 and 103 ms) after the R-peak of the ECG signal. The contour tracks the borders of the carotid artery, from which the change in the lumen area with the cardiac cycle is calculated. The images in the figure are normalized and shown in the corresponding colour scale.

For early atherosclerosis detection we believe that the CC method might be more appropriate since this allows for a PWV estimation within a larger part of the carotid artery and for left and right arteries, simultaneously. In addition, the CC approach is more stable and simple method compared to the QA method, since there is no need for subsequent advanced post processing steps, like automatic segmentation in the QA method. The QA method might be more suitable for characterization of the PWV in a specific location of interest.

Several scan acceleration techniques have been applied for accelerated flow-imaging, including parallel imaging and spatiotemporal acceleration techniques [31-34]. In general, these acceleration techniques allow for a shortening of the scan time by a factor of 2-5 and were applied on low temporal resolution data (<35 frames/s). Recently, an acceleration factor of eight was achieved on higher temporal resolution data (100 frames/s) [35], which is still only half of the temporal resolution of 200 frames/s we achieved in this chapter.

The PWV data we showed in this chapter are in line with the values reported in the literature. A range of reference values for the global PWV measurements using ultrasound have been reported. In one of the studies the average PWV is < 7 m/s for healthy young volunteers [36]. Recently, a feasibility study have been conducted to measure regional PWV in the carotids using ultrasound and the reported PWV range was (4.0 - 5.2 m/s) [27]. In elderly subjects and atherosclerotic patients, several studies showed elevated PWV values >10 m/s [2, 3, 27, 36, 37]. Although this may require a further increase in temporal resolution, due to the retrospective nature of the sequence, this can be achieved solely by prolongation of the imaging time.

Conclusion

In conclusion, a combination of retrospectively triggered phase-contrast MRI and compressed sensing reconstruction allows for regional carotid pulse wave velocity

measurements. Good reproducibility was observed across different imaging sessions. We believe this method serves as an important addition to the vessel wall MRI toolkit for the non-invasive characterization of atherosclerotic disease.

References

1. Laurent, S., et al., *Expert consensus document on arterial stiffness: methodological issues and clinical applications.* Eur Heart J, 2006. **27**(21): p. 2588-605.
2. Nesbitt, E., et al., *Assessment of arterial blood flow characteristics in normal and atherosclerotic vessels with the fast Fourier flow method.* MAGMA, 2000. **10**(1): p. 27-34.
3. Mohiaddin, R.H., D.N. Firmin, and D.B. Longmore, *Age-related changes of human aortic flow wave velocity measured noninvasively by magnetic resonance imaging.* J Appl Physiol (1985), 1993. **74**(1): p. 492-7.
4. Nichols, W.W., M.F. O'Rourke, and D.A. McDonald, *McDonald's blood flow in arteries : theoretic, experimental, and clinical principles*. 5th ed. 2005, London. New York: Hodder Arnold ;Distributed in the U.S.A. by Oxford University Press. xii, 607 p.
5. Hirata, K., M. Kawakami, and M.F. O'Rourke, *Pulse wave analysis and pulse wave velocity - A review of blood pressure interpretation 100 years after Korotkov.* Circulation Journal, 2006. **70**(10): p. 1231-1239.
6. Constantinesco, A., et al., *Spatial or flow velocity phase encoding gradients in NMR imaging.* Magn Reson Imaging, 1984. **2**(4): p. 335-40.
7. Nayler, G.L., D.N. Firmin, and D.B. Longmore, *Blood-Flow Imaging by Cine Magnetic-Resonance.* Journal of Computer Assisted Tomography, 1986. **10**(5): p. 715-722.
8. Axel, L. and D. Morton, *Mr Flow Imaging by Velocity-Compensated Uncompensated Difference Images.* Journal of Computer Assisted Tomography, 1987. **11**(1): p. 31-34.
9. Firmin, D.N., et al., *The Application of Phase-Shifts in Nmr for Flow Measurement.* Magnetic Resonance in Medicine, 1990. **14**(2): p. 230-241.
10. Bernstein, M.A., A. Shimakawa, and N.J. Pelc, *Minimizing Te in Moment-Nulled or Flow-Encoded 2-Dimensional and 3-Dimensional Gradient-Echo Imaging.* Jmri-Journal of Magnetic Resonance Imaging, 1992. **2**(5): p. 583-588.
11. Lalande, A., et al., *Compliance and Pulse Wave Velocity Assessed by MRI Detect Early Aortic Impairment in Young Patients With Mutation of the Smooth Muscle Myosin Heavy Chain.* Journal of Magnetic Resonance Imaging, 2008. **28**(5): p. 1180-1187.
12. Vulliemoz, S., N. Stergiopulos, and R. Meuli, *Estimation of local aortic elastic properties with MRI.* Magnetic Resonance in Medicine, 2002. **47**(4): p. 649-654.
13. Peng, H.H., et al., *Estimation of pulse wave velocity in main pulmonary artery with phase contrast MRI: Preliminary investigation.* Journal of Magnetic Resonance Imaging, 2006. **24**(6): p. 1303-1310.
14. Herold, V., et al., *In Vivo Measurement of Local Aortic Pulse-Wave Velocity in Mice With MR Microscopy at 17.6 Tesla.* Magnetic Resonance in Medicine, 2009. **61**(6): p. 1293-1299.
15. Fielden, S.W., et al., *A new method for the determination of aortic pulse wave velocity using cross-correlation on 2D PCMR velocity data.* Journal of Magnetic Resonance Imaging, 2008. **27**(6): p. 1382-1387.
16. Yu, H.Y., et al., *Quantification of the pulse wave velocity of the descending aorta using axial velocity profiles from phase-contrast magnetic resonance imaging.* Magnetic Resonance in Medicine, 2006. **56**(4): p. 876-883.
17. Boese, J.M., et al., *Estimation of aortic compliance using magnetic resonance pulse wave velocity measurement.* Physics in Medicine and Biology, 2000. **45**(6): p. 1703-1713.
18. Mohiaddin, R.H., *Magnetic-Resonance-Imaging of Peripheral Vascular-Disease - the State of the Artery.* Echocardiography-a Journal of Cardiovascular Ultrasound and Allied Techniques, 1992. **9**(5): p. 553-577.
19. Lusis, A.J., *Atherosclerosis.* Nature, 2000. **407**(6801): p. 233-241.
20. Lustig, M., D. Donoho, and J.M. Pauly, *Sparse MRI: The application of compressed sensing for rapid MR imaging.* Magnetic Resonance in Medicine, 2007. **58**(6): p. 1182-1195.
21. Heijman, E., et al., *Comparison between prospective and retrospective triggering for mouse cardiac MRI.* Nmr in Biomedicine, 2007. **20**(4): p. 439-447.
22. Nauerth, A., E. Heijman, and C. Diekmann. *Slice refocusing signal for retrospective reconstruction of CINE cardiac MR images*. in *Proc. Intl Soc. Magn. Reson. Med*. 2006.
23. Coolen, B.F., et al., *High frame rate retrospectively triggered Cine MRI for assessment of murine diastolic function.* Magnetic Resonance in Medicine, 2013. **69**(3): p. 648-656.
24. Greiser, A. and M. von Kienlin, *Efficient k-space sampling by density-weighted phase-encoding.* Magnetic Resonance in Medicine, 2003. **50**(6): p. 1266-1275.
25. Tsai, C.M. and D.G. Nishimura, *Reduced aliasing artifacts using variable-density k-space sampling trajectories.* Magnetic Resonance in Medicine, 2000. **43**(3): p. 452-458.

26. Herment, A., et al., *Automated Segmentation of the Aorta from Phase Contrast MR Images: Validation Against Expert Tracing in Healthy Volunteers and in Patients with a Dilated Aorta.* Journal of Magnetic Resonance Imaging, 2010. **31**(4): p. 881-888.

27. Voges, I., et al., *Normal values of aortic dimensions, distensibility, and pulse wave velocity in children and young adults: a cross-sectional study.* Journal of Cardiovascular Magnetic Resonance, 2012. **14**.

28. Dogui, A., et al., *Measurement of Aortic Arch Pulse Wave Velocity in Cardiovascular MR: Comparison of Transit Time Estimators and Description of a New Approach.* Journal of Magnetic Resonance Imaging, 2011. **33**(6): p. 1321-1329.

29. Ibrahim, E.S.H., et al., *Measuring aortic pulse wave velocity using high-field cardiovascular magnetic resonance: comparison of techniques.* Journal of Cardiovascular Magnetic Resonance, 2010. **12**.

30. Kroner, E.S.J., et al., *Pulse Wave Velocity and Flow in the Carotid Artery Versus the Aortic Arch: Effects of Aging.* Journal of Magnetic Resonance Imaging, 2014. **40**(2): p. 287-293.

31. Westenberg, J.J.M., et al., *Bramwell-Hill modeling for local aortic pulse wave velocity estimation: a validation study with velocity-encoded cardiovascular magnetic resonance and invasive pressure assessment.* Journal of Cardiovascular Magnetic Resonance, 2012. **14**.

32. Thunberg, P., M. Karlsson, and L. Wigstrom, *Accuracy and reproducibility in phase contrast imaging using SENSE.* Magnetic Resonance in Medicine, 2003. **50**(5): p. 1061-1068.

33. Beerbaum, P., et al., *Rapid left-to-right shunt quantification in children by phase-contrast magnetic resonance imaging combined with sensitivity encoding (SENSE).* Circulation, 2003. **108**(11): p. 1355-61.

34. Baltes, C., et al., *Accelerating cine phase-contrast flow measurements using k-t BLAST and k-t SENSE.* Magnetic Resonance in Medicine, 2005. **54**(6): p. 1430-1438.

35. Jung, B., et al., *Highly k-t-space-accelerated phase-contrast MRI.* Magn Reson Med, 2008. **60**(5): p. 1169-77.

36. Giese, D., T. Schaeffter, and S. Kozerke, *Highly undersampled phase-contrast flow measurements using compartment-based k-t principal component analysis.* Magnetic Resonance in Medicine, 2013. **69**(2): p. 434-443.

37. Luo, J.W., R.X. Li, and E.E. Konofagou, *Pulse Wave Imaging of the Human Carotid Artery: An In Vivo Feasibility Study.* Ieee Transactions on Ultrasonics Ferroelectrics and Frequency Control, 2012. **59**(1): p. 174-181.

Summary and Future Perspectives

As you go, you will make mistakes of your own

But son, that's alright, you live and you learn

I'm here and I'll be if I can a father and a friend.

Accelerating Cardiovascular MRI

Cardiovascular diseases are the major cause of death worldwide. MRI is the gold standard method to assess cardiac function. MRI plays an important role in the field of cardiovascular research and made a substantial contribution to the understanding of cardiac disease. In this thesis, strategies for better imaging and accelerating the cardiovascular MRI measurements were presented. In this final chapter, a summary and discussion for each of the presented protocols is given, followed by a brief perspective on future developments.

Murine Cardiovascular MRI

Mouse cardiac imaging is challenging because of the small size of the mouse heart and the high heart and breathing rates. The aim of this thesis was to develop in vivo magnetic resonance imaging (MRI) techniques that can help in assessing the cardiovascular status, and more specifically the thesis is focused on developing strategies to accelerate the MRI measurements. **In chapter 1**, a general introduction about the cardiovascular system and cardiac MRI was presented with an outline of common murine cardiac MR imaging strategies. This was followed by an overview of strategies for accelerating MRI in general and cardiovascular MRI in particular.

Retrospective Triggering

The development of retrospective triggering was a common theme in all of the chapters of this thesis. Retrospective triggering (often referred to as self-gating) is one of the most promising developments in the field of cardiovascular imaging. It provides robust reconstructions of Cinematic (Cine) MR images [1-5] without the need for ECG-based synchronization. Additionally, it allows for continuous steady-state imaging without periodic interrupts from cardiac and respiratory motion, which is beneficial for parametric mapping of tissue relaxation parameters. Data is acquired continuously, asynchronously

with the cardiac and respiratory cycle. After the acquisition is completed, a Cine movie or static images are reconstructed by binning the data into a specified number of cardiac frames and data affected by respiratory activity is discarded. Different strategies have been proposed to retrospectively assign each k-line to the corresponding cardiac time point and to determine respiration intervals. Several strategies exist to make these assignments. A separate navigator signal can be extracted from the refocusing gradient of the imaging slice as shown in chapter 2. Navigators can alternatively be obtained using specific acquisition strategies, such as radial imaging, for which the center point in k-space is recorded each TR as shown in Chapter 3. A navigator signal can also be obtained from a specific slice as shown in chapter 4. Moreover, a parallel recording of the physiological signals (ECG and respiratory) can be used for assigning k-lines to cardiac and respiratory intervals, as used in chapter 5.

Accelerating diastolic function cardiac MRI

For accurate assessment of the left ventricular diastolic function, a moderate temporal resolution imaging is required [5, 6]. The time resolution of mouse cardiac MRI is not sufficient to extract the detailed cardiac movement information during diastole. **In chapter 2**, we introduce a new protocol to obtain very high temporal resolution Cine MRI of the beating mouse heart within reasonable measurement time. The method is based on a self-gated accelerated FLASH acquisition [7] and CS reconstruction [8, 9]. The retrospective reconstruction produced undersampled and random k-t-space filling that allowed for CS reconstruction and acceleration. High acceleration factors were achieved which reduced scan times to 1.5 min instead of >10 min for a fully sampled scan. The accelerated high temporal resolution reconstructions preserve high image quality and the undersampling artifacts were effectively removed without compromising the quantification of the left ventricular functional parameters. The early-to-late filling rate (E/A) ratio was extracted from these accelerated reconstructions, which is considered one of the important parameters to assess diastolic function [10].

Fast Ultrashort Echo Time (UTE) Cine Imaging

One of the main artifacts in the standard FLASH approach cine MRI of the murine heart presented in chapter 2 is the signal voids and ghosting in the left ventricle (LV) lumen due to rapid blood flow. A solution to prevent such artifacts can be found in the use of an ultra-short echo time (UTE) sequence [11-12]. The use of a radial readout shortens TE considerably and enables artifact-free Cine of the murine heart. In line with the main theme presented in this thesis, in **chapter 3**, we presented a multi-slice protocol for whole heart Cine imaging, where the sequence was validated and tested in rats with chronic myocardial infarction as well as control rats, and all the cardiac movies were retrospectively reconstructed using navigator signals produced from the acquired radial spokes for each TR. However, a major drawback of the retrospective gating scheme was the long acquisition time. Full heart coverage with high acceleration factors was achieved with golden-angle radial undersampling and CS reconstruction. The sampling with the golden angle spacing presented in this protocol is favorable for CS construction pipeline, since they produce aliasing artifacts with high degree of incoherence [13].

Towards Accelerated 4D Flow Imaging

In **Chapter 4**, a preliminary study towards the development of a quantitative 4D UTE flow imaging sequence was presented. We aimed for a 3D time resolved UTE Flow MR imaging protocol for the whole mouse heart with self-gating and CS accelerated reconstruction. However, this objective was not fully reached yet and is still works in progress. Image quality needs to be improved and more validations need to be performed. Nevertheless, the phantom results showed good results in terms of flow velocity estimation in comparison to the standard FLASH based 3D Flow MR sequence. In-vivo validations still need to be performed. In case of the successful application of the proposed technique, full anatomical and functional maps for the whole heart can be acquired in a single scan

session, which will assist in better and comprehensive assessment of the cardiovascular system.

Regional PWV Estimation in Human Carotids

In **Chapter 5**, we presented a clinical development study. A method was proposed to estimate the regional pulse wave velocity (PWV) in the carotid artery. The sequence is based on phase contrast MRI, where we combine retrospective triggering and CS reconstruction, resulting in accelerated flow measurements with in-plane spatial resolution of 0.54 mm and temporal resolution of ~ 5 ms in 6 min total scan time. The PWV was estimated using two different methods: the cross correlation (CC) and the flow-area (QA) methods. The two methods were highly correlated (r=0.82), with a mean difference of 0.42 m/s [14]. Given the achieved accelerated high temporal resolution imaging, besides the clinically feasible scan times (3-6 min/slice), measuring the PWV in elderly persons and patients seems feasible. In addition, the retrospective triggering protocol would allow for increasing the temporal resolution even further at the expense of a moderate increase in total scan time.

Future perspective

The ultimate goal for cardiovascular MRI is a comprehensive 4D imaging protocol that can be completed in a reasonable scanning time. This goal is the main drive of many research efforts that are carried out in the cardiovascular research field. In vivo 4D MRI measurements would be a very powerful tool to extract anatomical and functional details of the heart. However, acquiring 4D MRI data in rodents as well as humans is very challenging and suffers from very long scan times and demands concerning post-processing [15-17]. One of the most powerful imaging techniques that has emerged recently in the field of cardiovascular MRI is radial imaging. For example, we showed in chapter 3 that it is able to provide flow-artifact free images of LV function. Radial imaging

(UTE) also is a promising technique for the detection of short T2 components and showed successful application in muscoskeletal studies [18]. Recently, ex vivo UTE imaging was applied to image infarcted rat hearts [19]. In addition, in vivo application of multi-slice cardiac Cine UTE has already been successfully implemented as shown in chapter 3 [13].

In chapter 4, we have taken the next step to combine 4D UTE imaging with phase contrast flow quantification. Successful application of this technique would yield full anatomical and quantitative functional maps of the heart in a single scan session, combining information concerning the cardiac anatomy, systolic function, infarcted region and quantitative flow measurements.

MRI is a relatively slow imaging modality compared to other imaging modalities such as ultrasound or CT because the speed of acquisition is constrained by hardware performance, such as gradient amplitudes and slew rates. In addition, signal averaging to achieve an acceptable signal to noise ratio (SNR) adds scan time. In a preclinical research setting, the total scan time is less of an issue as compared to clinical MRI [20], where patient compliance and comfort play an important role. Through acceleration, higher spatial resolution, temporal resolution or increased SNR through signal averaging can be achieved. As we described in chapter 1, the use of parallel imaging (PI) and multiple receiver coils has provided the opportunity to speed up the MRI [21-24]. In addition, novel acceleration techniques, like spatio-temporal and CS acceleration, have been developed in the last decade that add flexibility to the acquisition requirements and permit higher acceleration factors [8, 25-26].

Even higher acceleration factors could be obtained by combining CS and PI [27, 28]. CS follows the basic principle that the true full signal can be recovered from a low number of, incomplete, measurements, under the conditions that the signal is sparse in a specific transform domain and that the acquisition trajectory yields a high degree of incoherence. A recent extension to CS is Blind Compressed Sensing (BCS), which does not require any

prior knowledge about the sparsifying transform [29]. In BCS, a dictionary learning technique is used to find the optimal set of base elements to describe the MR image or movie in the most sparse fashion. In a recent study, the BCS method was applied to accelerate free breathing myocardial perfusion MRI showing significant improvement over compressed sensing reconstruction [30]. Spatio-temporal acceleration techniques, like kt-PCA, has found several successful applications in the field of cardiovascular research as detailed in chapter 1. Improving these techniques by adding additional constraints and penalties, will make them more robust and will help in achieving higher acceleration factors as shown in recent studies [31-32].

Conclusion

Improving noninvasive techniques for cardiovascular disease assessment is a hot topic in the medical imaging field. This fuels the development of novel MR imaging strategies and inspires many researchers to develop advanced techniques for cardiovascular status assessment. Further improvements in imaging hardware, sequences and acceleration techniques are necessary to mitigate the challenging tradeoff between temporal and spatial resolution and to facilitate comprehensive cardiovascular imaging in a short scan time.

References

1. Heijman, E., et al., *Comparison between prospective and retrospective triggering for mouse cardiac MRI.* NMR Biomed, 2007. **20**(4): p. 439-47.

2. Hoerr, V., et al., *Cardiac-respiratory self-gated cine ultra-short echo time (UTE) cardiovascular magnetic resonance for assessment of functional cardiac parameters at high magnetic fields.* J Cardiovasc Magn Reson, 2013. **15**: p. 59.

3. Bishop, J., et al., *Retrospective gating for mouse cardiac MRI.* Magn Reson Med, 2006. **55**(3): p. 472-7.

4. Coolen, B.F., et al., *High frame rate retrospectively triggered Cine MRI for assessment of murine diastolic function.* Magn Reson Med, 2013. **69**(3): p. 648-56.

5. Nauerth, A., E. Heijman, and C. Diekmann. *Slice refocusing signal for retrospective reconstruction of CINE cardiac MR images*. in *Proc. Intl Soc. Magn. Reson. Med*. 2006.

6. Stuckey, D.J., et al., *Novel MRI method to detect altered left ventricular ejection and filling patterns in rodent models of disease.* Magn Reson Med, 2008. **60**(3): p. 582-7.

7. Frahm, J., A. Haase, and D. Matthaei, *Rapid NMR imaging of dynamic processes using the FLASH technique.* Magn Reson Med, 1986. **3**(2): p. 321-7.

8. Donoho, D.L., *Compressed sensing.* Information Theory, IEEE Transactions on, 2006. **52**(4): p. 1289-1306.

9. Lustig, M., D. Donoho, and J.M. Pauly, *Sparse MRI: The application of compressed sensing for rapid MR imaging.* Magn Reson Med, 2007. **58**(6): p. 1182-95.

10. Motaal, A.G., et al., *Accelerated high-frame-rate mouse heart cine-MRI using compressed sensing reconstruction.* NMR Biomed, 2013. **26**(4): p. 451-7.

11. Robson, M.D., et al., *Magnetic resonance: an introduction to ultrashort TE (UTE) imaging.* J Comput Assist Tomogr, 2003. **27**(6): p. 825-46.

12. Bergin, C.J., G.H. Glover, and J.M. Pauly, *Lung parenchyma: magnetic susceptibility in MR imaging.* Radiology, 1991. **180**(3): p. 845-8.

13. Motaal, A.G., et al., *Functional imaging of murine hearts using accelerated self-gated UTE cine MRI.* The international journal of cardiovascular imaging, 2014: p. 1-12.

14. Motaal, A.G., et al. *Human Carotid Pulse Wave Velocity measurments Using Accelerated High Temporal Resolution MRI*. in *Proc. Intl Soc. Magn. Reson. Med*. *Benelux* 2015

15. Shin, T., et al., *Three dimensional first-pass myocardial perfusion imaging at 3T: feasibility study.* J Cardiovasc Magn Reson, 2008. **10**: p. 57.

16. Peters, D.C., et al., *Undersampled projection reconstruction applied to MR angiography.* Magn Reson Med, 2000. **43**(1): p. 91-101.

17. Thedens, D.R., et al., *Fast magnetic resonance coronary angiography with a three-dimensional stack of spirals trajectory.* Magn Reson Med, 1999. **41**(6): p. 1170-9.

18. Du, J., et al., *Qualitative and quantitative ultrashort echo time (UTE) imaging of cortical bone.* J Magn Reson, 2010. **207**(2): p. 304-11.

19. de Jong, S., et al., *Direct detection of myocardial fibrosis by MRI.* J Mol Cell Cardiol, 2011. **51**(6): p. 974-9.

20. Sharples, L., et al., *Cost-effectiveness of functional cardiac testing in the diagnosis and management of coronary artery disease: a randomised controlled trial. The CECaT trial.* Health Technol Assess, 2007. **11**(49): p. iii-iv, ix-115.

21. Pruessmann, K.P., et al., *SENSE: sensitivity encoding for fast MRI.* Magn Reson Med, 1999. **42**(5): p. 952-62.

22. Ratering, D., et al., *Accelerated cardiovascular magnetic resonance of the mouse heart using self-gated parallel imaging strategies does not compromise accuracy of structural and functional measures.* J Cardiovasc Magn Reson, 2010. **12**: p. 43.

23. Griswold, M.A., et al., *Generalized autocalibrating partially parallel acquisitions (GRAPPA).* Magn Reson Med, 2002. **47**(6): p. 1202-10.

24. Schneider, J.E., et al., *Ultra-fast and accurate assessment of cardiac function in rats using accelerated MRI at 9.4 Tesla.* Magn Reson Med, 2008. **59**(3): p. 636-41.

25. Tsao, J., P. Boesiger, and K.P. Pruessmann, *k-t BLAST and k-t SENSE: dynamic MRI with high frame rate exploiting spatiotemporal correlations.* Magn Reson Med, 2003. **50**(5): p. 1031-42.

26. Pedersen, H., et al., *k-t PCA: temporally constrained k-t BLAST reconstruction using principal component analysis.* Magn Reson Med, 2009. **62**(3): p. 706-16.

27. Otazo, R., et al., *Combination of compressed sensing and parallel imaging for highly accelerated first-pass cardiac perfusion MRI.* Magn Reson Med, 2010. **64**(3): p. 767-76.

28.   Lustig, M. and J.M. Pauly, *SPIRiT: Iterative self-consistent parallel imaging reconstruction from arbitrary k-space.* Magn Reson Med, 2010. **64**(2): p. 457-71.
29.   Gleichman, S. and Y.C. Eldar, *Blind Compressed Sensing.* Ieee Transactions on Information Theory, 2011. **57**(10): p. 6958-6975.
30.   Lingala, S.G. and M. Jacob, *Blind compressive sensing dynamic MRI.* IEEE Trans Med Imaging, 2013. **32**(6): p. 1132-45.
31.   Giese, D., T. Schaeffter, and S. Kozerke, *Highly undersampled phase-contrast flow measurements using compartment-based k-t principal component analysis.* Magn Reson Med, 2013. **69**(2): p. 434-43.
32.   Jung, H., et al., *k-t FOCUSS: a general compressed sensing framework for high resolution dynamic MRI.* Magn Reson Med, 2009. **61**(1): p. 103-16.

Acknowledgment

At the end of my PhD journey, I would like to admit that my thesis would not have been completed without the support and guidance of some beloved people who contributed to the work presented herein throughout my PhD study.

Dear Klaas, it was a great pleasure and honor to be part of the research team in the Biomedical NMR group in Eindhoven university of Technology. I enjoyed the stimulating environment and the great support you offered. You set a great example of a group leader who seeks to ensure and maintain the nice atmosphere so everyone around enjoys what they are doing. I will never forget your fruitful scientific discussions, ideas, and advice concerning my personal and scientific development.

Dear Luc, thanks very much for your support and guidance during my PhD. I remember, whenever I asked for attending scientific courses, conferences, or other specific requests like high performance computer, you were always cooperative and ready to sign with the approval. That helped me proceed with my experiments and of course positively influenced my scientific development. It was such an honor to be affiliated to the IST/e.

Dear Gustav, you are the best! I would like to give you special thanks for what you did and still doing for me through your help, support, supervision, and guidance which are the core reasons for executing this thesis. I feel proud to have you as my daily supervisor and co-promoter. You made things possible and were always pushing me forward. I have a lot of bad times, but you did your best by trying to make everything smooth, and you showed very good understanding of these situations. And yes, sharing some music interests with your co-promoter makes a difference.

My paranymphs: Igor, I remember these days you were trying to bring me around to 'bouldering', but man, I am sorry to say that it never worked out. I guess it was proved when you wrapped your arms for some time with this white thing. You were a very friendly colleague. I wish you all the best in your future endeavors and particularly with your PhD defense soon.

Valentina, being an international student, makes it easier for me to enjoy lunch breaks, discussions and outings with you. This is because I can rest assured that the language of discussion is English, even though sometimes it did not work out in some of our group lunch breaks. I remember during these times, we sometimes had this look on our faces which says: "ok, shall we stay or shall we go back to the office, or cigarettes?" I also still recall your delicious tiramisu in the crazy housewarming party. I wish you all the best with your PhD and your personal life. Do not forget that in any paper you will acknowledge me for the best knee image you got so far: My knee MR images.

I would also like to extend my thanks to my PhD committee: prof. Webb, prof. Faber, Dr. Nederveen, Dr. Mischi, and prof. Hilbers for the time they spent reading my thesis, and for their valuable feedback to further improve it.

My first officemates: Leonie, Tessa, Ewelina and Bram. Thanks for the encouraging friendly environment, which I guess was very important especially at the commencement of my PhD. I enjoyed our company, although I know that you suffered a lot from the music coming out of my headphones. I wish you all the best in your career and personal life.

HTC office mates: Desi, Sharon, and Bart, I enjoyed a lot our hot-chili office. "dat is afhankelijk van of Sharon en Desi aanwezig waren of niet !" Thanks Bart for the candy that was always there, I wish you all the best with Medtronic and your upcoming life events, having a baby? Desi, I enjoyed working together a lot. I also like your Indonesian food. I wish you and your family all the best. Sharon, you are nearly there with your defense, I am sure it will be great. I wish you all the best in your career path.

Dear Wolter, thanks very much. I learned a lot from you. You were such a great colleague. Your comments and advice whenever I had any scientific related/non-related question really helped me to a great extent. Thanks for the great help you offered especially in the work presented in chapter 4. I wish you all the best in Toshiba!

To my colleagues and Master students, Nils, Huiming, and Robart-Jan, it was very nice working together. You were diligent students and most of the work presented in this thesis was during your M.Sc study. You contributed a lot to it. I wish you all the best with your PhD and careers.

I would like also to thank Dr. Prompers, my colleagues in the NMR lab, Jules, Tom, Rik, Stephanie, Katriene, Bastian, Ot, Miranda, Marloes and Philips research PhD students and members. It was a really very nice time I spent with you all. Thanks to Larry, David, Jo and Leonie for all the help they offered with MR technical problems and animal handling. Also I would like to thank Floortje for her valuable assistant, support and Dutch conversations. I wish you all the best.

Bram and Wouter, I enjoyed a lot working with both of you especially in the work presented in chapter 5. You are such an honorable example of clever and hardworking researchers. I got a lot of benefits from working with you, and I hope to proceed with our team work and collaboration in our current projects.

Thanks Verena for welcoming me in Munster to conduct some experiments for the work presented in chapter 4. You are a very nice and clever researcher. I wish you the best of luck with your new position and your personal life. Philip Bovenkamp, thanks for your help in some of the results presented in chapter 4. I wish you all the best with the rest of Your PhD.

Dr. Nederveen, thanks very much for your understanding of the transition from my PhD to my postdoc position in your lab. I know that working in your lab will add a lot to me and will increase my scientific and research skills.

Dr. Faber, thank you very much for welcoming me in your lab for 10 days to conduct some experiments. I enjoyed my stay there and I had nice moments in the beautiful Munster city.

And from the bottom of my heart, I would like to express my gratitude to my father, my confidant, my supporter and my biggest fan. I believe that any personal or scientific achievement I had before, or have at this very moment, or will have throughout my whole life, happened thanks to you. You always dreamt about seeing the PhD thesis of your 'dearest friend and the reason of happiness in your life' as you were always calling me, however you passed away during my study and it was unbearably tough and hard. The pain is excruciating and will always remain. I remember the daily emails you were sending to remind me of how many days left to get the PhD. You were counting down, every single day, and you were waiting for this day more than anyone else, even me. But on the other side, I know that your spirit is surrounding me and that it will never die because I always sense your presence before making an important decision or before having any important event in my life. My father, I miss you. You left a hole in my heart that can never be filled.

To my beloved mother, I am grateful for your help and support. I know that you did a lot for our family and you were always pushing and supporting me to move on. You know, I was thinking about canceling my PhD and returning home as I am supposed to be the man of the family after my dad passed away. When you refused and asked me to carry on, you promised that everything will be fine, and you fulfilled your promise. Thanks my mother for everything, I ask God to help me be a good son for you.

My crazy sister and brother: Lolita and Seif. Thanks for your support during my PhD period. Lolita, thank you for always texting and calling me to know the result of conference submission, journal acceptance, and important meetings. I remember the day my young brother Seif, 16-year-old, texted me late at the night of my thesis submission to ask if everything is fine. Brother and sister, you are the best ever. Thanks also to my uncles for traveling a long distance to attend my PhD defense.

To my fiancée, the girl I chose to spend the rest of my life with, thanks for all the support you gave me during the tough periods I was going through the previous year. I accomplished now one of the most important steps of my life, and the next is … our marriage ;). I love you!

Thanks to my 'online' Egyptian friends, specifically 'El-Nas ElRay'aa. Hawtk, Bakry, Abo ElShwady, Kimo, Hateman, Lo2lo2, 3etra and Wello. Our daily chat was nice to change the mood and to give us the needed support. Besides, our outings and trips together from time to time were an

excellent way to give ourselves a break, so that we could focus more in our research work after the return. I wish for you all the best in your personal life and career.

Special thanks go to my friend Walid, my housemate with whom I spent the last year. Thanks for your company and your advice regarding my thesis and personal decisions. Thanks to Mustafa who has been my nearest friend since our B.Sc. studies in Egypt. Thanks for your "amazing" cover designs, your famous high resolution images and your friendship. I wish you and your family all the best. And for both of you guys, you were such great brothers and friends and I wish you all the best with the rest of your PhD.

I received a lot of support from so many people that I haven't necessarily mentioned in the acknowledgement. For those, please accept my apology and thanks very much.

Abdallah Motaal

وكان فضل الله عليك عظيماً

List of Publications

- ➤ **International Journal Articles**

  - **Motaal, A.G.,** Coolen, B. F., Abdurrachim, D., Castro, R. M., Prompers, J. J., Florack, L. M. J., Nicolay, K. and Strijkers, G. J. (2013), Accelerated high-frame-rate mouse heart cine-MRI using compressed sensing reconstruction. NMR Biomed., 26: 451–457.
  - Coolen, B. F., Abdurrachim, D., **Motaal, A.G.,** Nicolay, K., Prompers, J. J. and Strijkers, G. J. (2013), High frame rate retrospectively triggered Cine MRI for assessment of murine diastolic function. Magn Reson Med, 69: 648–656.
  - **Motaal A.G.,** Noorman N, de Graaf WL, Hoerr V, Florack LM, Nicolay K, Strijkers GJ. Functional imaging of murine hearts using accelerated self-gated UTE cine MRI. Int J Cardiovasc Imaging. 2014 Sep 10 Doi: s10554-014-0531-8
  - Bakermans A.J., Abdurrachim D., Moonen R.P.M., **Motaal A.G.**, J.J. Prompers, G.J Strijkers, K. Vandoorne, K. Nicolay. Small animal MR imaging and spectroscopy of cardiovascular disorder. Progress Nucl Magn Reson Spectros. Invited Review.
  - **Motaal, A. G.,** Potters Wouter, Coolen, B. F., Nicolay, K. Nederveen A., and Strijkers, G. J. (2014), Human Carotid Pulse Wave Velocity Measurements Using Accelerated High Temporal Resolution Carotid MRI. In Preparation.

- ➤ **Conference Proceedings**

  - **Motaal, A.G.,** Noorman, N., Graaf, W., Florack, L. M. J., Nicolay, K. and Strijkers, G. J. (2014), Accelerated self-gated UTE MRI of the murine heart – SPIE '14 Medical Imaging, San-Diego, California, USA.
  - **Motaal, A.G.,** N., Osman, N. Improved Strain Measuring in Fast Strain Encoded Cardiac MR (2011). ISBI 2011, IL, USA.
  - **Motaal, A.G.,** Osman, N. Strain Correction in Interleaved strain-encoded (SENC) cardiac MR (2010). SPIE '10 Medical Imaging, San-Diego, California, USA.
  - **Motaal, A.G.,** ElGayar, N., Osman, N. Automated Cardiac-Tissue Identification in Composite Strain Encoded (C-SENC) Images Using Fuzzy K-Means and Bayesian Classifier (2010). iCBBE '10, Chengdu, China.
  - **Motaal, A.G.,** ElGayar, N., Osman, N. Different Regions Identification in Composite Strain Encoded (C-SENC) Images Using Machine Learning Techniques (2010). ANNPR 2010, Springer LNAI 5998.
  - **Motaal, A.G.,** AlAttar, M., Fahmy, A., Osman, N. Cardiac MRI Steam Images Denoising Using Bayesian Classifier - CIBEC'08, Egypt.

- ➤ **Refereed Abstracts (Author and co-author list)**

  - **Motaal A.G.,** Potters W.V., Dong H., Florack L.J., Nicolay K., Nederveen A., Strijkers G.J., Coolen B.F. Carotid Pulse Wave Velocity Measurements Using Accelerated High Temporal Resolution MRI. ISMRM 2015, Canada.
  - Calcagno C., Giannarelli C., **Motaal, A.G.** Nahrendorf M., Mulder W., Fayad Z.A., Strijkers G.J. Self-gated dynamic contrast enhanced (DCE) MRI with compressed sensing acceleration to quantify permeability in the aortic root of atherosclerotic mice. ISMRM 2015, Canada.
  - **Motaal A.G.,** Hoerr V., Dong H., Florack L.J., Nicolay K., Strijkers G.J. Accelerated 4D Phase Contrast UTE MRI. ISMRM 2015, Canada.
  - De Graaf W., **Motaal A.G.**, Noorman N., Florack L.J., Nicolay K., Strijkers G.J. Accelerated self-gated UTE MRI of the murine heart – SCMR 2014, USA.

- Moonen R., A comparison of two sequences for spectral imaging of 19F-containing emulsions. ISMRM 2014, Italy.
- van Nierop B.J, Nelissen J.L., Bax N, **Motaal A.G.**, de Graaf L., Nicolay K., Strijkers G.J. In Vivo Ultra Short TE (UTE) MRI Detects Diffuse Fibrosis in Hypertrophic Mouse Hearts. ISMRM 2013, USA.
- **Motaal A.G.,** Coolen B.F., Abdurrachim D., Nicolay K., Prompers J.J, Strijkers G.J. Accelerated High Frame Rate Mouse CINE CMR Using Retrospective Triggering and Compressed Sensing Reconstruction. ISMRM 2012, Australia.
- Coolen B.F., Abdurrachim D., **Motaal A.G.**, Nicolay K., Strijkers G.J., Prompers J.J. High spatio-temporal resolution retrospectively gated CINE imaging for measuring diastolic function in mice – ISMRM 2012, Australia.